SYNTHESIS, CHARACTERIZATION AND SENSOR STUDIES OF THIOPHENE CONJUGATED COPOLYMERS

A Thesis Submitted to
the Graduate School of
İzmir Institute of Technology
in Partial Fulfillment of the Requirements for the Degree of

MASTER OF SCIENCE

in Chemistry

by
Tolunay KURT

December 2024
İZMİR

We approve the thesis of **Tolunay KURT**

Examining committee members:

Prof. Dr. Ümit Hakan YILDIZ
Department of Chemistry, İzmir Institute of Technology

Prof. Dr. Talat YALÇIN
Department of Chemistry, İzmir Institute of Technology

Assoc. Prof. Dr. Ümit TAYFUN
Department of Basic Science, Bartın University

06 December 2024

Prof. Dr. Ümit Hakan YILDIZ
Supervisor,
Department of Chemistry,
İzmir Institute of Technology

Prof. Dr. Gülşah ŞANLI MOHAMED
Head of the Department of Chemistry

Prof. Dr. Mehtap EANES
Dean of the Graduate School

ACKNOWLEDGEMENTS

I would like to thank my advisor, Prof. Dr. Ümit Hakan YILDIZ, for his valuable knowledge, continuous support, guidance and patience. His guidance and encouraging words have contributed greatly to me, not only academically but also personally, during this process. He will always be with me, inspiring me throughout this journey and in every aspect of my life.

I am also grateful to my thesis committee members, Prof. Dr. Talat Yalçın and Assoc. Prof. Dr. Ümit Tayfun, for their participation and valuable feedback.

My heartfelt thanks go to my mother, Tülay KURT, my father, Hüseyin KURT and my sister, İlke KURT who have always been there for me, supported every decision I made. My greatest wish is to be able to reciprocate the efforts you have given me.

I am deeply thankful to the entire Biomacros family, with whom I am very happy to be together and work with. Special thanks to my colleagues Fatih SEMA and Mert EREM for their help and support.

I would also like to thank Soner KARABACAK, who has never withheld his assistance since the day I joined the Biomacros Polymer Research Group and and who has shared all of his knowledge with me. I am truly grateful for everything he has contributed to my development.

I would like to sincerely thank Assoc. Prof. Dr. Ahu Arslan YILDIZ and PhD student Başak Çoban for their contributions and assistance with the cell studies, which played an important role in my thesis.

My last and biggest thank you goes to my Super Best Friend, Sanem DİNÇKAL. I feel very lucky and happy to have her in my life. She is so valuable to me, always supporting and encouraging me at every moment. She is the special person in my life who makes me feel special simply because she is in it. I love you.

Scientific and Technological Research Council of Turkey (TÜBİTAK-122Z519) supports this thesis.

ABSTRACT

SYNTHESIS, CHARACTERIZATION AND SENSOR STUDIES OF THIOPHENE CONJUGATED COPOLYMERS

This thesis includes the synthesis and characterization cationic and non-ionic monomers and their corresponding polymers for the application bioimaging and biosensing applications. The cationic polymers were synthesized via oxidative polymerization, and their structural and optical properties were thoroughly characterized using NMR, Mass Spectroscopy, Absorbance Spectroscopy, Fluorescence Spectroscopy, Raman Spectroscopy, Dynamic Light Scattering, Zeta Potential Charge Analysis, and Quantum Yield Analysis. The homopolymers and copolymers, produced with varying ratios of 3-butoxy-4-methylthiophene (M1) and N-allyl-N-methyl-N-(3-((4-methylthiophen-3-yl)oxy)propyl)prop-2-en-1-aminium (M2) monomers, were analyzed for their performance in various applications.

A significant focus of the thesis was placed on enhancing the permeability of these nanomaterials across the blood-brain barrier (BBB) for potential therapeutic uses, particularly by optimizing the structures of polymer dots (Pdots) in the nanometer range (5-30 nm). Among the synthesized polymers, P4 (1:1 ratio M1/M2) demonstrated superior performance in crossing the BBB.

In addition, it investigated the application of cationic polymers as optical probes for the detection of Candida species, especially in the context of oral health. The polymers demonstrated enhanced fluorescence and high specificity for Candida binding, showing great potential for noninvasive detection of Oral Candidiasis. The findings suggest that these cationic polymers could serve as effective diagnostic tools for the early detection of Oral Candida, offering significant promise for clinical management.

The thesis presents cationic polymers and Pdots as highly effective materials for both detecting oral fungal infections and for potential biomedical applications, particularly in improving drug delivery across the blood-brain barrier.

ÖZET

TİYOFEN YAPILI KONJUGE KOPOLİMERLERİN SENTEZİ, KARAKTERİZASYONU VE SENSÖR ÇALIŞMALARI

Bu tez, biyosensör ve biyogörüntüleme uygulamaları için katyonik ve iyonik olmayan monomerlerin ve bunlara karşılık gelen polimerlerin sentezini, karakterizasyonunu içerir. Katyonik polimerler oksidatif polimerizasyon yoluyla sentezlendi ve yapısal ve optik özellikleri NMR, Kütle Spektroskopisi, Absorbans Spektroskopisi, Floresan Spektroskopisi, Raman Spektroskopisi, Dinamik Işık Saçılması, Zeta Potansiyel Yük Analizi ve Kuantum Verim Analizi kullanılarak kapsamlı bir şekilde karakterize edildi. 3-bütoksi-4-metiltiyofen (M1) ve N-alil-N-metil-N-(3-((4-metiltiyofen-3-il)oksi)propil)prop-2-en-1-aminyum (M2) monomerlerinin değişen oranlarıyla üretilen homopolimerler ve kopolimerler, çeşitli uygulamalardaki performansları açısından analiz edildi.

Tezin önemli bir odağı, özellikle nanometre aralığında (5-30 nm) polimer noktalarının (Pdots) yapılarını optimize ederek, bu nanomalzemelerin kan-beyin bariyeri (BBB) boyunca geçirgenliğini potansiyel terapötik kullanımlar için artırmaya yerleştirildi. Sentezlenen polimerler arasında P4 (1:1 oranında M1/M2), BBB'yi geçmede üstün performans gösterdi.

Ek olarak, tez, özellikle ağız sağlığı bağlamında, Candida türlerinin tespiti için optik problar olarak katyonik polimerlerin uygulanmasını araştırmaktadır. Polimerler, Candida bağlanması için gelişmiş floresans ve yüksek özgüllük göstererek, Oral Kandidiyazis'in invaziv olmayan tespiti için büyük bir potansiyel göstermektedir. Bulgular, bu katyonik polimerlerin Oral Candida'nın erken tespiti için etkili tanı araçları olarak hizmet edebileceğini ve klinik yönetim için önemli bir vaat sunabileceğini göstermektedir.

Bu tez, katyonik polimerleri ve Pdot'ları hem oral mantar enfeksiyonlarını tespit etmek hem de özellikle kan-beyin bariyeri boyunca ilaç iletimini iyileştirmek için potansiyel biyomedikal uygulamalar için oldukça etkili malzemeler olarak sunmaktadır.

TABLE OF CONTENTS

LIST OF FIGURES

Figure **Page**

Figure **Page**

Figure **Page**

Figure **Page**

Figure **Page**

Figure **Page**

Figure **Page**

Figure **Page**

Figure **Page**

LIST OF TABLES

Table **Page**

CHAPTER 1

INTRODUCTION

1.1.Motivation

Conjugated polymers, particularly those based on thiophene, have emerged as versatile materials with exceptional electronic, optical, and structural properties.(Lu, Li, and Lei 2021) Their ability to bridge the gap between organic and inorganic materials has opened a myriad of applications, ranging from organic electronics to renewable energy technologies and biomedical innovations. Thiophene-based polymers stand out due to their high charge carrier mobility, thermal stability, and ease of structural modification, making them key candidates for advanced device fabrication. (İncel et al. 2017)

Despite significant progress, challenges such as stability, scalability, and functional diversity remain, particularly in addressing specific needs in biomedicine and multifunctional sensing platforms. (Arslan-Yildiz et al. 2016) Designing thiophene-based hydrophilic and hydrophobic polymers and copolymers offers a promising pathway to overcome these limitations. Hydrophilic derivatives can facilitate interactions with aqueous environments, enabling applications in biosensing, drug delivery, and even crossing the blood-brain barrier.(Knop et al. 2010) In contrast, hydrophobic structures are essential for optoelectronic and energy-related applications, where moisture sensitivity is a critical concern.(Perepichka et al. 2005)

This thesis is driven by the need to synthesize and explore the potential of thiophene-based conjugated polymers with tunable hydrophilic and hydrophobic properties. By addressing both fundamental and applied aspects, the research aims to contribute to the development of advanced materials capable of meeting the demands of next-generation technologies in electronics and healthcare. This motivation stems from the interdisciplinary importance of these materials and their potential to revolutionize various fields through innovative design and application.

1.2. Conjugated Polymers

Conjugated polymers (CPs) are advanced organic materials with a backbone structure composed of alternating single and double bonds, leading to a delocalized π-electron system. (Pankow and Thompson 2020) This unique configuration imparts CPs with exceptional electronic and optical properties, enabling them to function as semiconductors and even metallic conductors when appropriately doped. Their lightweight nature, flexibility, and ease of processing make them ideal for applications in cutting-edge technologies such as organic electronics, renewable energy, and sensors. (Yucel et al. 2021)

The versatility of CPs arises from their tunable properties, which can be tailored through chemical modifications and copolymerization techniques. This allows the creation of materials optimized for specific functions, including organic light-emitting diodes (OLEDs), organic photovoltaics (OPVs), and field-effect transistors (OFETs) .(Al-Azzawi et al. 2022; Zaumseil and Sirringhaus 2007; Sirringhaus 2014) Additionally, their sensitivity to environmental stimuli, such as light, temperature, and chemical analytes, positions CPs as indispensable materials for advanced sensing technologies. (Özenler et al. 2019; Higgins et al. 2020)

Despite their numerous advantages, CPs face challenges such as environmental stability and limited charge mobility, which can restrict their performance in certain applications. Ongoing research aims to overcome these limitations by developing new synthesis methods, enhancing material stability, and exploring hybrid structures. These efforts underscore the potential of conjugated polymers to revolutionize fields like flexible electronics, sustainable energy, and smart materials, making them a focus of modern materials science and engineering. (Yadav, Kumar, and Maiti 2022)

1.3. Thiophene Based Conjugated Polymers

Thiophene-based conjugated polymers represent a significant subclass of conjugated polymers, distinguished by the incorporation of thiophene rings into their backbone structure. Thiophene, a sulfur-containing heterocyclic compound, imparts unique electronic and structural properties to the resulting polymers. These properties

include high thermal stability, excellent charge carrier mobility, and strong π-π stacking interactions, making thiophene-based polymers highly desirable for various advanced applications.

The modular structure of thiophene-based polymers allows for extensive chemical modifications, enabling the fine-tuning of their electronic, optical, and solubility properties.(Tu et al. 2017) This adaptability has led to their widespread use in organic photovoltaics (OPVs), organic field-effect transistors (OFETs), and light-emitting diodes (OLEDs).(M. Y. Lee et al. 2018) Additionally, their compatibility with solution-processing techniques, such as spin-coating and printing, supports cost-effective manufacturing of flexible and lightweight devices.

One of the emerging areas of research involving thiophene-based conjugated polymers is their potential for biomedical applications, including biosensing and drug delivery. Their amphiphilic nature achieved by designing hydrophilic and hydrophobic copolymer structures can facilitate interactions with biological systems, including crossing the blood-brain barrier. This unique capability positions thiophene-based polymers as promising candidates for next-generation materials in healthcare and bioelectronics. (Inal et al. 2018)

However, challenges such as oxidative stability and scalability in synthesis remain critical considerations. Current research is focused on developing robust derivatives, enhancing environmental stability, and integrating thiophene-based polymers into hybrid systems to unlock their full potential. These advancements reinforce their role as pivotal materials in driving innovation across electronics, energy, and biomedical fields.

1.3.1. Thiophene Based Conjugated Homopolymers and Copolymers

Thiophene-based conjugated polymers, including organic dyes, quantum dots, fluorescent proteins, and conjugated polymer nanoparticles, are pivotal in advanced material development and imaging applications. (Sayar et al. 2018) Thiophene-based conjugated homopolymers, with their repeating thiophene units, exhibit uniform structures that enhance electronic and optical properties, making them ideal for applications in organic electronics like transistors, solar cells, and LEDs. (Yildiz, Alagappan, and Liedberg 2013) Their thermal stability, efficient charge transport, and

processability into thin films further their utility in flexible and lightweight devices.(Coropceanu et al. 2007) Similarly, thiophene-based conjugated copolymers expand these functionalities by incorporating additional monomers, enabling precise control over electronic and structural properties. The inclusion of hydrophilic and hydrophobic units in these copolymers introduces amphiphilic behavior, paving the way for applications in biomedical fields, such as drug delivery and crossing the blood-brain barrier.

Complementing these polymeric materials, fluorescent agents serve as indispensable tools in bioimaging. (Pitsalidis et al. 2022; Braeken et al. 2017) Organic dyes, valued for their specificity in targeting biomolecules, are widely used in cell and tissue imaging. Quantum dots, though offering size-tunable fluorescence and exceptional imaging capabilities, face limitations due to toxicity. (Lim, Shen, and Gao 2015) Fluorescent proteins, with their natural emission properties, are non-toxic alternatives but suffer from lower photostability. Conjugated polymer nanoparticles, derived from thiophene-based materials, emerge as promising agents in this domain. These nanoparticles, ranging from 30 to 100 nm in size, in 3D cell culture, organoid, blood-brain barrier and tissue labeling. (Karabacak et al. 2024) By incorporating both hydrophilic and hydrophobic units, these copolymers can exhibit amphiphilic behavior, making them suitable for interactions with biological systems, including potential applications in drug delivery and blood-brain barrier crossing. Their amphiphilic and optoelectronic properties make them highly effective for advanced imaging and sensing applications, further highlighting the versatility of thiophene-based materials in next-generation electronics and bioanalytic.

1.4.Oxidative Polymerization of Synthesized Polymers

Oxidative polymerization is a widely used method for synthesizing conjugated polymers, including thiophene-based structures.(Torres and Balogh 2012) This process involves the oxidation of monomers, typically in the presence of an oxidizing agent such as ferric chloride ($FeCl_3$) or a similar catalyst, leading to the formation of polymer chains through coupling reactions. (Hebert et al. 2021) The technique is advantageous for its simplicity, scalability, and ability to produce high-molecular-weight polymers under mild

conditions. For synthesized thiophene-based polymers, oxidative polymerization helps maintain the integrity of the conjugated backbone while allowing for the incorporation of functional groups, enabling the design of materials with tailored electronic, optical, and solubility properties. This approach is especially valuable in creating both hydrophilic and hydrophobic derivatives for diverse applications.

Oxidative Polymerization, as a method of forming polymers through oxidation reactions, offers different advantages compared to Suzuki-Miyaura, and Direct Arylation Polymerization methods. This method is particularly notable for its cost-effective and simple reaction conditions, while providing the advantage of being environmentally friendly and reducing solvent requirements. As suggested by Hebert et. al $FeCl_3$ polymerization yields non regio regular polymers. However, the degree of polymerization is high as compared to Suzuki coupling. (Bautista et al. 2021) Oxidative Polymerization is successful in synthesizing high molecular weight polymers, but the polymerization process is less controllable and can lead to wider molecular weight distributions. In contrast, as suggested by Bautista et al. Suzuki-Miyaura, and Direct Arylation Polymerization methods provide better controlled polymerizations, producing high molecular weight polymers and offering narrower distributions. In addition, while these methods offer advantages in terms of functional group tolerance and chain growth, it can be said that oxidative polymerization is preferred for simpler applications and low-cost solutions.

1.5. Sensor Studies of Conjugated Polymers

Sensor studies aim to advance technologies for detecting biomarkers, environmental toxins, and other analytes by developing innovative materials and devices.(Köksal et al. 2024) These studies include designing wearable diagnostic tools and portable devices, such as smartphone-integrated systems for environmental monitoring and real-time biomarker analysis. (Yildiz, Alagappan, and Liedberg 2013; Tokel et al. 2015) The integration of smart polymers, particularly polythiophenes, is central to these sensors due to their unique optical properties that respond to molecular interactions, enabling label-free and effective bioanalytical applications. (Yucel et al. 2024) Additionally, the use of advanced nanomaterials, such as electroactive nanogels

and bio-repellent interfaces, enhances the precision, sensitivity, and biocompatibility of these sensors. This research is critical for creating accessible, efficient, and non-invasive solutions in both healthcare diagnostics and environmental analysis.

1.5.1. Sensor Studies of Conjugated Polymer Dots (Pdots) on the Blood-Brain Barrier (BBB)

Conjugated Polymer Dots (Pdots), a class of nanoscale fluorescent polymers, have emerged as highly promising materials in blood-brain barrier (BBB) research due to their exceptional optical properties, biocompatibility, and versatility. (Englert et al. 2016) The BBB is a highly selective barrier that protects the brain from harmful substances while restricting the delivery of any therapeutic agents and diagnostic tools. Pdots offer a unique combination of properties that make them ideal candidates for applications targeting the BBB. (Li et al. 2016)

Pdots are distinguished by their high fluorescence quantum yield, photostability, and nanoscale size, enabling their use in imaging, biosensing, and drug delivery applications.(Feng et al. 2013) (Karabacak et al. 2024) Their nanoscale dimensions allow for enhanced permeability and retention effects, facilitating their transport across the BBB when functionalized with specific targeting ligands or peptides. This makes Pdots effective carriers for therapeutic agents and diagnostic probes, providing the dual benefit of crossing the BBB and interacting selectively with brain tissues or disease biomarkers. (Y. Liu et al. 2018)

Pdots are particularly valuable in sensor applications due to their sensitivity to environmental changes and molecular interactions. This responsiveness allows for real-time, non-invasive detection of neurological disease biomarkers, enabling early diagnosis and monitoring.(Yuan et al. 2021) Additionally, Pdots' photostability and resistance to photobleaching make them ideal for long-term imaging and tracking within the brain, surpassing many traditional fluorescent dyes and quantum dots in performance.

The versatility of Pdots also extends to their surface chemistry, which can be tailored to optimize interactions with the lipid-rich BBB. Hydrophilic Pdots enhance solubility and biocompatibility, making them suitable for drug delivery systems, while hydrophobic Pdots can better penetrate the lipid bilayer of the BBB. This adaptability

enables the design of multifunctional Pdots that combine therapeutic delivery with advanced imaging and sensing capabilities, offering a comprehensive approach to tackling the challenges the BBB poses. (Zhang et al. 2024)

Pdots represent a groundbreaking material for BBB studies, combining nanoscale size, fluorescence sensitivity, and functional versatility. Their potential to enable non-invasive diagnosis and efficient therapeutic delivery positions them as transformative tools in neurological disease research.(Sim et al. 2020) As the field progresses, Pdots are poised to play a central role in overcoming BBB-related challenges and advancing personalized medical solutions for brain disorders.

1.5.2.Sensor Study of Conjugated Polymers for Detecting Candidiasis

In sensor studies, conjugated polymers can transduce molecular interactions into detectable signals, such as changes in conductivity, fluorescence, or absorbance. (Heydari Gharahcheshmeh and Gleason 2022) This property enables the development of highly specific and efficient sensing platforms. By functionalizing their structure with target-specific moieties, conjugated polymers can be tailored to detect biomarkers for diseases, toxic substances, or environmental pollutants. Their tunable electronic properties, biocompatibility, and stability make them particularly suitable for real-time monitoring applications, including medical diagnostics, environmental analysis, and food safety. The integration of conjugated polymers into sensor systems represents a significant advancement in material science, offering innovative solutions for addressing critical challenges in detection and monitoring technologies. Sensor studies of conjugated polymers for detecting candidiasis using point-of-care (POC) tests focus on developing rapid, sensitive, and cost-effective diagnostic tools for the early detection of Candida infections.(P.-W. Lee et al. 2022) Conjugated polymers, especially those based on thiophene and other conjugated systems, are ideal candidates for this purpose due to their ability to undergo measurable changes in conductivity, fluorescence, or absorption when interacting with specific biomarkers associated with candidiasis. By functionalizing these polymers with recognition elements that specifically bind to Candida cells or related metabolites, these sensors can provide a highly selective response to the presence of Candida species, even at low concentrations.

The use of conjugated polymers in POC tests offers several advantages, including ease of integration into portable, user-friendly devices that can be used in non-laboratory settings, such as clinics or at home.(Syedmoradi et al. 2017) The rapid and real-time detection of candidiasis using these sensors can facilitate earlier diagnosis, reduce the need for invasive testing, and improve treatment outcomes, particularly in high-risk patients like those with weakened immune systems. (Safavieh et al. 2017) Moreover, POC tests utilizing conjugated polymer-based sensors can be developed to be both low-cost and highly accessible, making them invaluable tools for global healthcare, particularly in regions with limited access to advanced laboratory facilities.

CHAPTER 2

MATERIALS AND METHODS

2.1.Materials

Copper(I) Bromide (Sigma-Aldrich CAS: 7787-70-4 (%99.999)), 1-methyl-2-pyrrolidinone CAS: 872-50-4 (NMP) (Sigma Aldrich (%99.5)), Na Metal, 3-bromo-4-methylthiophene (Sigma-Aldrich CAS: 30318-99-1 (%97)), Sodium Bromide (Sigma-Aldrich CAS: 7647-15-6 #Lot: MKBW9982V (%99)), Diethyl ether (Sigma-Aldrich CAS: 60-29-7 (%99), Magnesium Sulfate (Sigma-Aldrich CAS: 7487-88-9 #Lot:MKCJ8677 (>%97)), 3-Bromopropanol (Sigma-Aldrich CAS:627-18-9 #Lot: SHBL9166 (%97)), Toluene (Merck CAS:108-88-3 (>99.5)), Sodium Bisulfate (Sigma Aldrich CAS:7681-38-1 #Lot:BCBQ8936V %95)), Silica gel 60 (0.063-0.200 mm)(Merck KGaA CAS:7631-86-9)), Hexane (Tekkim CAS: 110-54-3 (>%98)), Ethyl Acetate (Tekkim CAS: 114-75-6 (%99.5)), Diallymethylamine (ACROS Organics CAS:2424-01-3#Lot: A0392649 (%98 in water)), Tetrahydrofuran (Sigma-Aldrich CAS:109-99-9 #Lot:BCBR4090V (>%99.9)) Iron (III) Chloride (Sigma-Aldrich CAS:7705-08-0 (%98)), Chloroform (Carlo Erba Reagents CAS: 67-66-3 (>%99.5)), Methanol (ISOLAB chemicals CAS:67-56-1 (>%99.5)), Butanol CAS: 71-6-3 (ACROS organics (>%99.5)) Ethylene Glycol CAS:107-21-1 (Merck (%99.5)) Chloroform-d CAS: 865-49-6 (99.8%, Merck), Deuterium oxide CAS: 7789-20-0 (D_2O, 99.96%, Merck) was purchased.

2.2.Methods

2.2.1.Synthesis of Monomer 1

The synthesis of 3-butoxy-4-methylthiophene (M1) was achieved using 3-bromo-4-methylthiophene (1 g, 5.64 mmol) as the starting material. Initially, 1.18 g of sodium (Na) was gradually added to 20 mL of distilled 1-butanol to prepare a 25% NaOBu/1-butanol solution. Subsequently, 0.5 mL of 1-methyl-2-pyrrolidone (5.20 mmol) and 10 mL of the prepared NaOBu/1-butanol solution (33.0 mmol) were introduced into a dry reaction flask. To this mixture, 3-bromo-4-methylthiophene (1 g, 5.64 mmol) and CuBr (0.8 g, 5.6 mmol) was added. The reaction was conducted under a nitrogen atmosphere at 130 °C using a water-cooled condenser. Upon completion, the reaction mixture was cooled to room temperature, followed by the addition of 10 mL of 0.25% sodium bromide solution with vigorous stirring. The mixture was then filtered and extracted three times with 50 mL portions of diethyl ether. The organic layer was washed thoroughly with deionized water and dried over anhydrous magnesium sulfate ($MgSO_4$). The solvent was removed under reduced pressure using a rotary evaporator, and the crude product was purified by column chromatography using hexane as the eluent. This procedure yielded 0.60 g of 3-butoxy-4-methylthiophene as a light-yellow oil, with an overall yield of 62.5%.

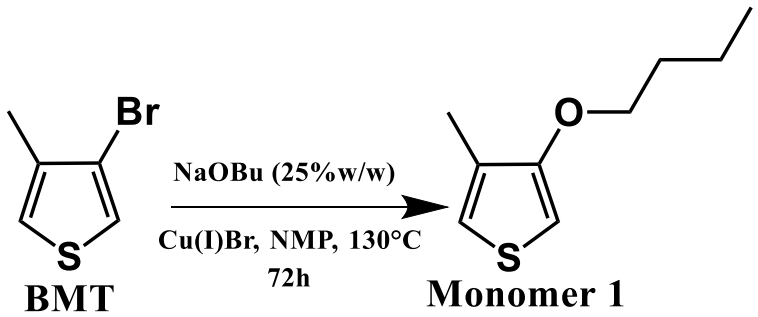

Figure 2.1 Synthesis of 3-butoxy-4-methylthiophene (Monomer 1)

2.2.2.Synthesis of Monomer 2

Synthesis of PC1: The synthesis of a target compound was carried out using 3-bromo-4-methylthiophene (BMT), copper(I) bromide (CuBr), N-methyl-2-pyrrolidone (NMP), and sodium methoxide (NaOMe), following a well-defined procedure. A 25% (w/v) solution of sodium methoxide was first prepared by reacting 2.67 g of sodium metal, pre-washed with hexane to remove residual oil, with 30 mL of anhydrous methanol in a 100 mL round-bottom flask. The reaction was allowed to proceed at room temperature for 3 hours to ensure complete dissolution. For the synthesis, 1.0 g of BMT (5.64 mmol), 0.5 g of CuBr (3.48 mmol), 2 mL of NMP (20.83 mmol), and 4 mL of the prepared NaOMe solution (25% w/v, 17.44 mmol) were added to a 50 mL dry round-bottom flask equipped with a magnetic stirrer. The reaction was conducted under a nitrogen atmosphere at 110 °C for 3 days using a water-cooled condenser system to maintain a controlled environment. Upon completion, the reaction mixture was cooled to room temperature, and 10 mL of deionized water (DI) containing 0.25 g of sodium bromide (NaBr) was added. The resulting mixture was stirred vigorously for 1 hour to facilitate phase separation. The organic product was extracted with diethyl ether at least five times, followed by thorough washing with deionized water. Any residual water in the organic layer was removed using anhydrous magnesium sulfate ($MgSO_4$). The solvent was then evaporated under reduced pressure using a rotary evaporator. Finally, the crude product was purified by column chromatography with hexane as the eluent. This process yielded 0.47 g of the intermediate compound as a pure product, corresponding to a yield of 65%. This synthesis demonstrates an efficient method for the preparation of the desired compound with a satisfactory yield. (^{1}H NMR (400 MHz, CDCl 3, δ, ppm,) 6.84 (1H, d),6.18 (1H, d), 3.84 (3H, s), 2.11 (3H, s))

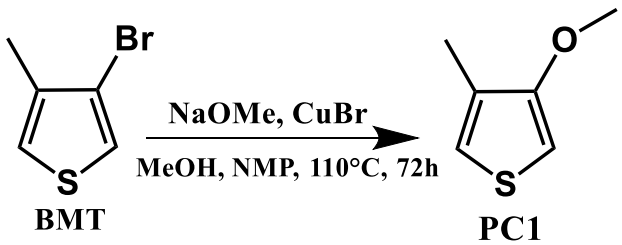

Figure 2.2. Synthesis of Precursor 1 (PC1)

Synthesis of PC2 (3-(3-Bromopropoxy)-4-Methylthiophene): The synthesis of 3-(3-bromopropoxy)-4-methylthiophene is accomplished using 3-methoxy-4-methylthiophene, 3-bromo-1-propanol, sodium bisulfate (NaHSO4), and toluene. The synthesis steps are detailed as follows:

A 50 mL round-bottom flask is charged with 3-methoxy-4-methylthiophene (0.42 g, 3.30 mmol), 3-bromo-1-propanol (1.0 g, 7.2 mmol), sodium bisulfate (62 mg, 0.45 mmol), and toluene (8 mL). The reaction mixture is stirred under a nitrogen atmosphere at 100 °C for 24 hours. After completion of the reaction, the flask is allowed to cool to room temperature. The toluene is evaporated using a rotary evaporator before the extraction phase. The reaction mixture is extracted with diethyl ether at least five times and subsequently washed with water. The organic phase is dried over magnesium sulfate (MgSO4) and the diethyl ether is removed using a rotary evaporator.The crude product is purified using column chromatography. Initially, hexane is used for the separation of unreacted starting materials, followed by a solvent mixture of 8:1 hexane-ethyl acetate for further purification. As a result, 3-(3-bromopropoxy)-4-methylthiophene is obtained as a colorless oil, weighing 0.50 g, with a yield of 65%. This compound is intended for use in the synthesis of monomers 2 and 3.

In conclusion, the synthesis of the target compound was successfully achieved with a yield of 65% by following the outlined steps. (1 H NMR (400 MHz, CDCl 3, δ 6.83 (1H, d), 6.19 (1H, d), 4.08 (2H, m),3.59 (2H, m), 2.34 (2H, m), 2.09 (3H, s))

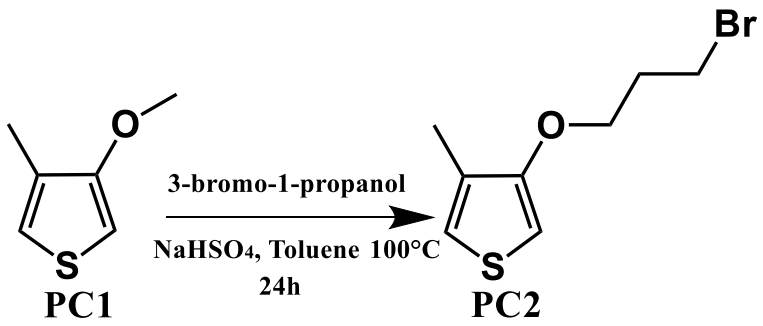

Figure 2.3. Synthesis of Precursor 2 (PC2)

Synthesis of Monomer 2: In this study, Monomer 2 was synthesized via the reaction of the bromopropoxy group in 3-(3-bromopropoxy)-4-methylthiophene with a selected tertiary amine group. The detailed synthesis procedure is as follows:

3-(3-bromopropoxy)-4-methylthiophene (0.25 g, 1.06 mmol), N-allyl-N-methylprop-2-en-1-amine (1.5 mL, 10.7 mmol), and tetrahydrofuran (THF) (15 mL) were added to a 50 mL round-bottom flask. The reaction mixture was heated to 72 °C and stirred for 2 days under a nitrogen atmosphere using a water-cooled condenser.

After the reaction was completed, the crude product was washed with THF and centrifuged at 3000 rpm for several minutes, repeating the process at least three times to precipitate the desired product. During each cycle, the supernatant was carefully collected and discarded. The resulting white precipitate was dried under vacuum in a desiccator, yielding the final monomer as a solid residue. This procedure successfully led to the synthesis of Monomer 2.

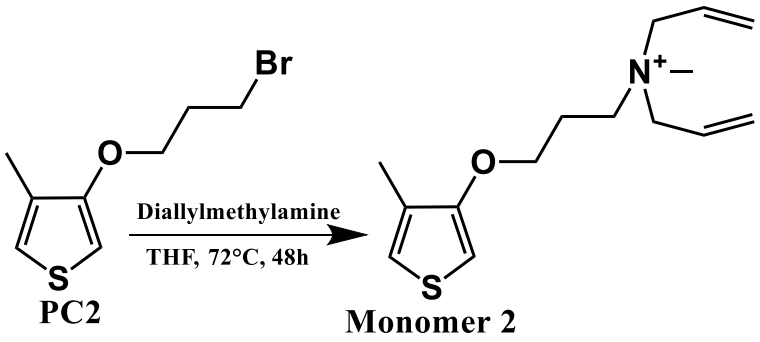

Figure 2.4. Synthesis of Monomer 2 (M2)

2.2.3. Synthesis of Homopolymers and Copolymers

2.2.3.1. Synthesis of Monomer 1 Homopolymer

Monomer 1 was polymerized by oxidative polymerization. For this polymerization reaction, 20 mg (0.12 mmol) of Monomer 1 was taken into a vial and dissolved in 1.5 ml of chloroform. 78 mg (0.48 mmol) of $FeCl_3$ was prepared by dissolving in 2 ml of chloroform. After the Monomer 1 and $FeCl_3$ solutions were completely dissolved, the Monomer solution was added dropwise into the $FeCl_3$. Then the reaction medium was inert, and the reaction continued for 24 hours.

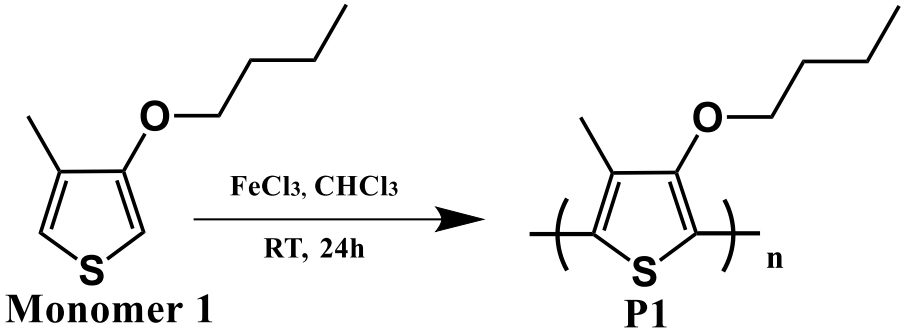

Figure 2.5. Synthesis of P1 polymer

When the polymerization was completed, the polymers in the vial formed black solid particles as precipitates. To purify these polymers, the reaction medium was taken into a falcon. Methanol was added drop by drop into the falcon and it was aimed to dissolve and remove the $FeCl_3$ in the medium. After washing with methanol 3 times, the polymer was dried by vacuuming in a desiccator.

2.2.3.2. Synthesis of P2 (10:1 Ratio M1/M2) Copolymer

Copolymer P2 was synthesized via oxidative polymerization. 20 mg (0.12 mmol) of Monomer 1 and 3.3 mg (0.012 mmol) of Monomer 2 were combined in a vial and dissolved in 1.5 mL of chloroform. Separately, 90 mg (0.55 mmol) of $FeCl_3$ was dissolved in 2 mL of chloroform. After complete dissolution of both the monomer and $FeCl_3$

solutions, the monomer solution was gradually added dropwise to the $FeCl_3$ solution. The reaction medium was then purged with an inert gas, and the polymerization reaction was allowed to proceed for 24 hours.

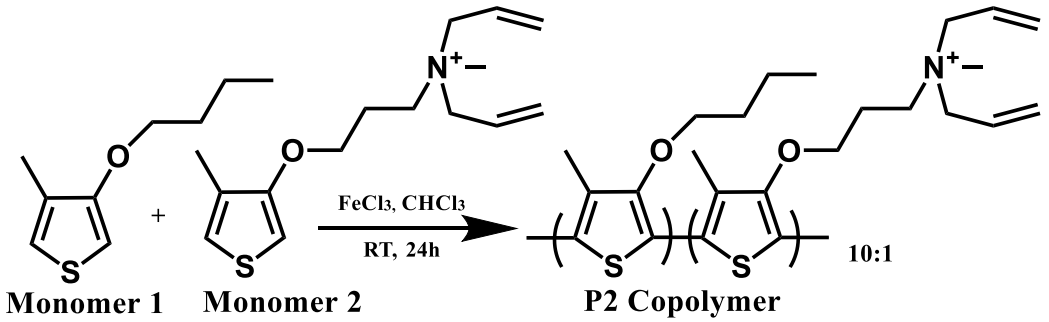

Figure 2.6. Synthesis of P2 polymer

Upon completion of the polymerization, the polymers precipitated as black solid particles within the vial. To purify the resulting polymers, the reaction mixture was transferred to a falcon tube. Methanol was then added dropwise to the falcon tube, aiming to dissolve and remove the residual $FeCl_3$ from the medium. The polymer was washed three times with methanol and subsequently dried under vacuum in a desiccator.

2.2.3.3. Synthesis of P3 (5:1 Ratio M1/M2) Copolymer

Copolymer P3 was polymerized by oxidative polymerization. For this polymerization reaction, 20 mg (0.12 mmol) of Monomer 1 and 6.6 mg (0.025 mmol) of Monomer 2 (5:1) were taken into a vial and dissolved in 2 ml chloroform. 95 mg (0.59 mmol) of $FeCl_3$ was dissolved in 2 ml chloroform. After the monomers and $FeCl_3$ solutions were completely dissolved, the Monomer solution was added dropwise into the $FeCl_3$. Then the reaction medium was inert, and the reaction continued for 24 hours.

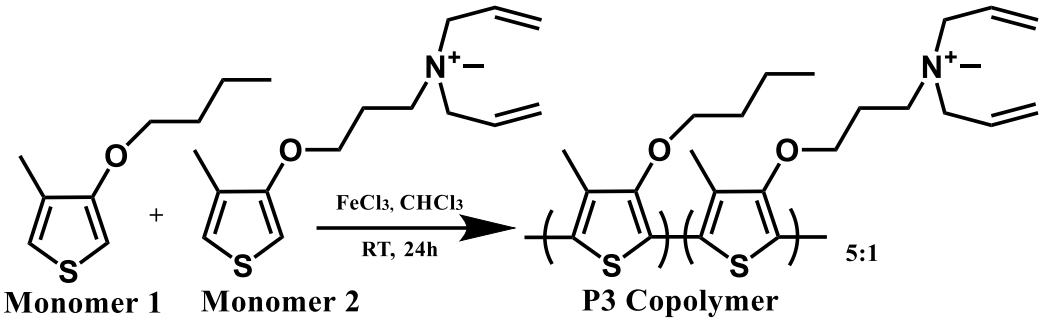

Figure 2.7. Synthesis of P3 polymer

After the polymerization was complete, the polymers precipitated as black solid particles within the vial. To purify the resulting polymers, the reaction mixture was transferred to a falcon tube. Methanol was then added dropwise to the tube to dissolve and remove the $FeCl_3$ from the solution. The polymer was washed three times with methanol and subsequently dried under vacuum in a desiccator.

2.2.3.4. Synthesis of P4 (1:1 Ratio M1/M2) Copolymer

Copolymer P4 was synthesized through oxidative polymerization. In this reaction, 10 mg (0.06 mmol) of Monomer 1 and 16 mg (0.06 mmol) of Monomer 2 were placed in a vial and dissolved in 2 mL of chloroform. Separately, 78 mg (0.48 mmol) of $FeCl_3$ was dissolved in another 2 mL of chloroform. Once the monomer and $FeCl_3$ solutions were fully dissolved, the monomer solution was gradually added dropwise to the $FeCl_3$ solution. The reaction mixture was then made inert, and polymerization proceeded for 24 hours.

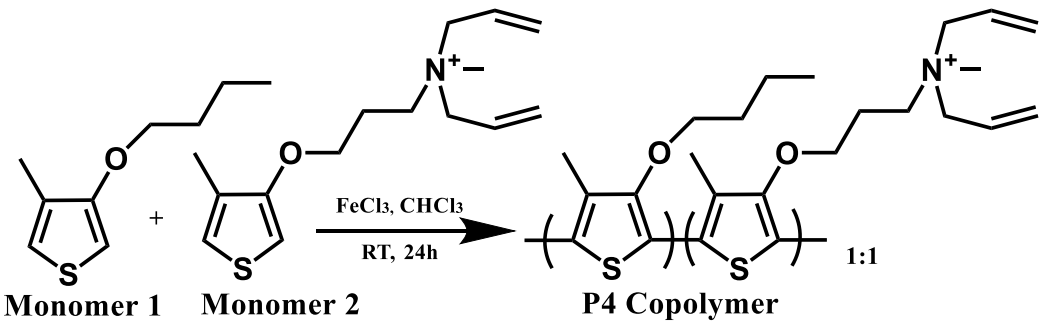

Figure 2.8. Synthesis of P4 polymer

At the end of the polymerization, the polymers precipitated as black solid particles in the vial. To purify these polymers, the reaction mixture was transferred to a falcon tube. Methanol was then added dropwise to dissolve and remove the $FeCl_3$. After three washes with methanol, the polymer was dried under vacuum in a desiccator.

2.2.3.5. Synthesis of P5 (1:5 Ratio M1/M2) Copolymer

Copolymer P5 was produced by oxidative polymerization. For this reaction, 2.6 mg (0.015 mmol) of Monomer 1 and 20 mg (0.075 mmol) of Monomer 2 were added to a vial and dissolved in 2 mL of chloroform. In a separate vial, 58.4 mg (0.36 mmol) of $FeCl_3$ was dissolved in 2 mL of chloroform. After both solutions were fully dissolved, the monomer solution was slowly added dropwise to the $FeCl_3$ solution. The reaction mixture was then purged with inert gas, and polymerization was allowed to continue for 24 hours.

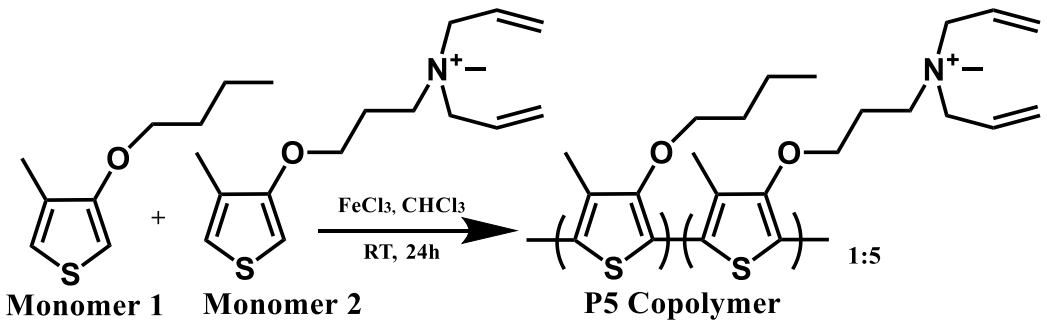

Figure 2.9. Synthesis of P5 polymer

After the polymerization was completed, the polymers precipitated as black solid particles in the vial. To purify these polymers, the reaction mixture was transferred to a Falcon tube. Methanol was then added drop by drop to dissolve and remove any remaining $FeCl_3$. Following three washes with methanol, the polymer was dried under vacuum in a desiccator.

2.2.3.6. Synthesis of P6 (1:10 Ratio M1/M2) Copolymer

Copolymer P6 was prepared using oxidative polymerization. For this reaction, 1.28 mg (0.0075 mmol) of Monomer 1 and 20 mg (0.075 mmol) of Monomer 2 were added to a vial and dissolved in 2 mL of chloroform. Separately, 53.5 mg (0.33 mmol) of $FeCl_3$ was dissolved in an additional 2 mL of chloroform. After both the monomer and $FeCl_3$ solutions were completely dissolved, the monomer solution was slowly added dropwise to the $FeCl_3$ solution. The reaction medium was then purged with inert gas, and polymerization was allowed to continue for 24 hours.

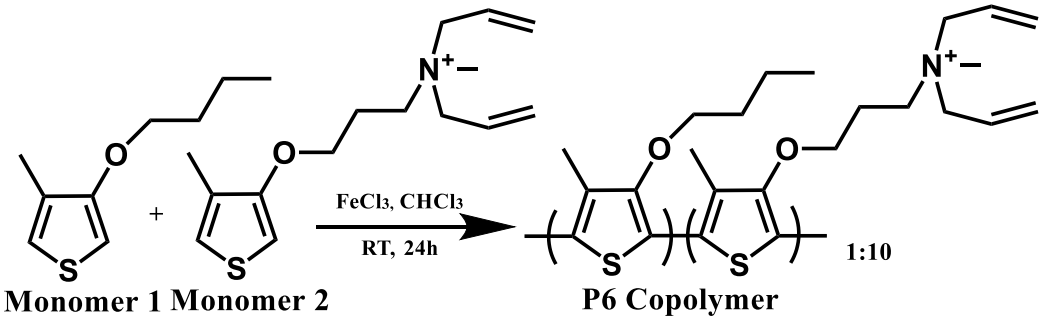

Figure 2.10. Synthesis of P6 polymer

After the polymerization was complete, the polymers appeared as black solid particles in the flask. For purification, the reaction mixture was transferred to a Falcon tube, where methanol was slowly added dropwise to dissolve and remove the remaining $FeCl_3$. After washing with methanol 3 times, the polymer was dried in desiccator under vacuum.

2.2.3.7. Synthesis of P7 (M2 Homopolymer)

Monomer 2 was polymerized by oxidative polymerization. For this polymerization reaction, 20 mg (0.075 mmol) of Monomer 2 was taken into a vial and dissolved in 1.5 ml of chloroform. 48.8 mg (0.30 mmol) of $FeCl_3$ was prepared by dissolving in 2 ml of chloroform. After the Monomer 2 and $FeCl_3$ solutions were

completely dissolved, the Monomer solution was added dropwise into the $FeCl_3$. Then the reaction medium was inert, and the reaction continued for 24 hours.

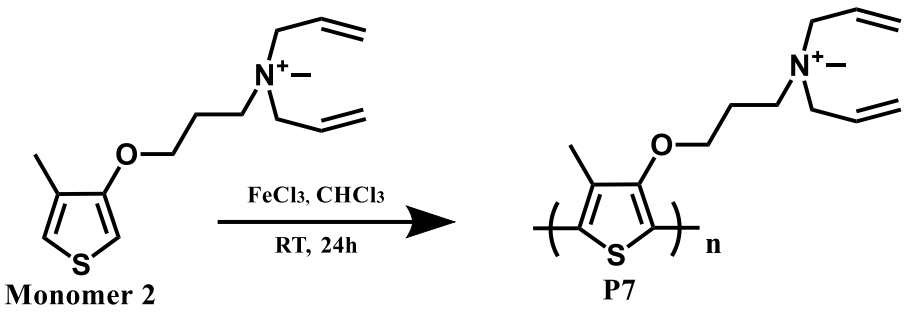

Figure 2.11. Synthesis of P7 polymer

Upon completion of polymerization, the polymers appeared as black solid particles in the vial. For purification, the reaction mixture was transferred to a Falcon tube, where methanol was gradually added drop by drop to dissolve and eliminate any residual $FeCl_3$. After washing the polymer three times with methanol, it was vacuum-dried in a desiccator.

2.2.4. Purifications of the Polymers

2.2.4.1. Methanol Rinsed Polymer Precipitates

Polymer washing with methanol is a basic purification technique frequently used after polymer synthesis. In this process, methanol removes unreacted monomers, low molecular weight oligomers, catalysts, and other by-products from the polymer sample. The low boiling point and polarity of methanol make it ideal for cleaning unwanted impurities without dissolving the polymer. Usually, the polymer sample is mixed with methanol in a container and gently stirred. This process facilitates the cleaning of remaining impurities.(Yildiz et al. 2006). The efficiency of the washing process is increased by renewing the methanol in the solution several times. Sometimes, to provide high purity, a rinse with other solvents can be used after the methanol. After the washing process is completed, the polymer sample is separated from the methanol and dried under vacuum to ensure that all solvent residues evaporate. This method is a highly effective,

low-cost purification process in polymer chemistry that allows the preservation of sensitive polymer structures.

2.2.4.2.Diethyl Ether Rinsed Polymer Precipitates

The purification of Diethyl Ether was not initially considered a part of the planned procedure. Over time, particles observed in the 0.5 mg/mL P7 polymer solution led to polymer degradation. Residual $FeCl_3$ in the aqueous environment, which was not fully removed, caused corrosion. This highlighted that MeOH posed challenges for cationic and water-soluble polymers like P7. Due to the polymer's partial solubility in MeOH, repeated washes eventually dissolved the entire polymer. These findings indicate that an alternative solvent should be used for rinsing instead of MeOH. Subsequent research and trials determined that Diethyl Ether could effectively remove $FeCl_3$ residues without dissolving the polymer.

2.2.5. Characterization Experiments

2.2.5.1. Nuclear Magnetic Resonance (NMR) Spectroscopy Analysis

Nuclear Magnetic Resonance (NMR) Spectroscopy is a powerful analytical technique used to determine the structure, dynamics, and chemical environment of molecules, particularly organic compounds. NMR spectroscopy works by exploiting the magnetic properties of certain atomic nuclei. When placed in a strong magnetic field, nuclei such as hydrogen ^{1}H or carbon ^{13}C absorb and re-emit radiofrequency energy at specific frequencies unique to their environment within the molecule. By analyzing the resulting NMR spectra, which display peaks corresponding to different nuclei and their interactions, scientists can determine the molecular structure, identify functional groups, and study molecular conformation. NMR is essential in chemistry, biochemistry, and materials science due to its non-destructive nature and high precision in elucidating molecular details.

Figure 2.12. 400 MHz Varian Nuclear Magnetic Resonance Spectroscopy.

2.2.5.2.Matrix-assisted Laser Desorption Ionization Time-of-flight Mass Spectrometry (MALDI-TOF MS) Analysis

Matrix-assisted Laser Desorption Ionization Time-of-flight Mass Spectrometry (MALDI-TOF MS) is an analytical technique widely used to determine the molecular weight and structure of large biomolecules, such as proteins, peptides, and polymers. In MALDI-TOF MS, a sample is mixed with a matrix compound that absorbs laser energy and aids in desorption and ionization of the sample molecules. A laser beam then excites this matrix-sample mixture, causing the molecules to ionize. These ions are accelerated in an electric field and travel through a flight tube, where their time of flight (TOF) is measured. The time taken to reach the detector depends on the mass-to-charge ratio of the ions, allowing for the calculation of their molecular weights. MALDI-TOF MS is valued for its high sensitivity, rapid analysis, and ability to analyze complex mixtures.

Figure 2.13. MALDI-TOF MS Device.

2.2.5.3.Varioscan Wellplate Reader UV-FL

UV-fluorescence (UV-FL) analysis is a technique widely used to characterize the optical properties of compounds, especially in fields such as materials science and polymer research. In this method, UV light typically excites a sample, causing electronic transitions that emit fluorescence at a characteristic wavelength. By examining both absorbance and emission spectra, valuable information can be obtained about the molecular structure, conjugation, and environment of the analyzed sample. This information is particularly useful for understanding and evaluating energy transfer processes.

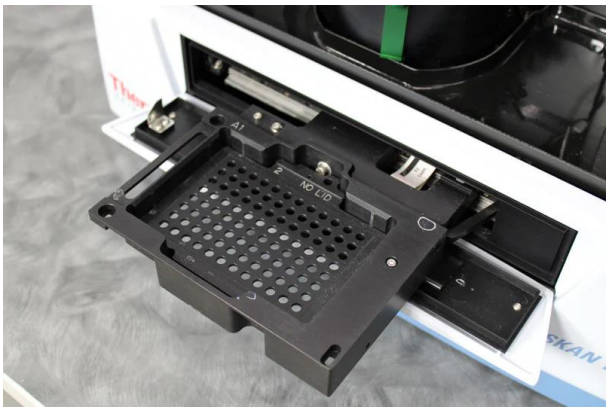

Figure 2.14. Varioscan Wellplate Reader

2.2.5.4. Malvern DLS and Zeta-Sizer Instrument

Dynamic Light Scattering (DLS):

Dynamic Light Scattering is a technique widely used for measuring the size of small particles or molecules in a sample. It relies on the scattering of light by particles in motion, specifically using the principles of Brownian motion. As particles scatter light, the fluctuations in the intensity of this scattered light at a specific angle are analyzed to determine particle size distribution. DLS is particularly useful for characterizing solution nanoparticles, proteins, and polymers.

Zeta-Sizer:

The Zeta-Sizer, developed by Malvern Panalytical, is a device that operates based on DLS principles. It measures particle size, zeta potential, and molecular weight. Zeta potential provides insight into particles' surface charge, which in turn informs the stability of a suspension. A low zeta potential indicates a higher likelihood of particles aggregating and settling, whereas a high zeta potential suggests a stable suspension. The Zeta-Sizer is widely utilized in fields like biotechnology, pharmaceuticals, chemistry, and material sciences for its precise particle characterization capabilities.

Figure 2.15. Dynamic Light Scattering and Zeta-Sizer devices

2.2.5.5. FS5 Instrument

The FS5 Spectrofluorometer, produced by Edinburgh Instruments, is a high-performance instrument designed for comprehensive fluorescence spectroscopy applications. It is particularly valued for its ability to measure fluorescence and phosphorescence with exceptional sensitivity and precision. The FS5 covers a broad spectral range, allowing users to capture detailed fluorescence emission and excitation spectra, as well as time-resolved fluorescence measurements. FS5 device was used for Quantum Yield measurements of synthesized polymers.

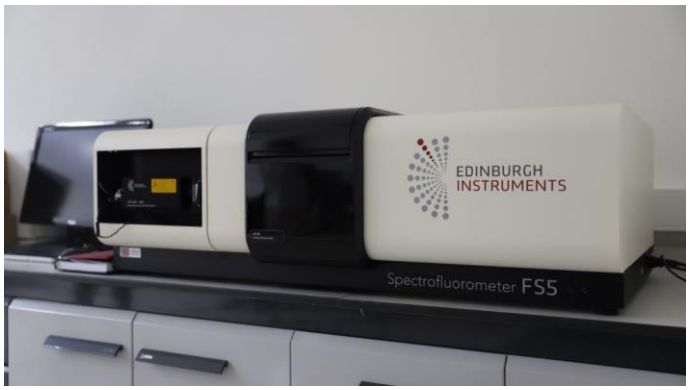

Figure 2.16. FS5 Quantum Yield Spectrofluorometer

2.2.5.6. Raman Spectroscopy Instrument

A Raman Spectrometer is an analytical instrument designed to identify molecular composition and structure by utilizing Raman scattering. When a sample is irradiated with a laser, a small fraction of the light is scattered at different energies, creating a unique "Raman fingerprint" for each molecule. By analyzing the Raman spectrum, researchers can obtain detailed information about molecular vibrations, chemical bonds, and crystal structures, making it highly useful for material identification and characterization.

Raman spectrometers are used in a wide range of fields, including chemistry, materials science, pharmaceuticals, and forensics. They are especially valuable for non-destructive analysis, as samples do not need to be altered for testing. Modern Raman instruments often come with advanced features such as confocal microscopy, which

enables spatially resolved measurements and can operate across a variety of wavelengths, from the UV to near-infrared, to suit diverse application needs.

Figure 2.17. Raman Spectrometer Instrument

CHAPTER 3

RESULT AND DISCUSSION

3.1.Characterization of Monomers and Polymers

The characterization of the monomers and polymers was conducted using ^{1}H NMR, ^{13}C NMR, MALDI-TOF MS, UV-FL spectroscopy, Dynamic Light Scattering (DLS), Raman Spectroscopy, and Zeta Sizer techniques to gain detailed insight into their structural and chemical properties. These analyses provided comprehensive information on the structure and characteristic features of the monomers.

3.1.1. Characterization of Monomer 1

The synthesis of the M1 molecule was initiated with 1 g of (3-bromo-4-methylthiophene) BMT as the starting reactant. After purification, the final product was obtained with a mass of 0.6 g. This outcome corresponds to an approximate reaction yield of 62.5%, indicating an efficient synthesis process for the Monomer 1. Similar synthesis protocols from the literature were referenced for comparison. For instance, a study by Iwatsuki et al. yielded 48% with a similar method, while Tanaka et al. reported a yield of 52%. The M1 synthesis achieved in this project demonstrates a higher yield compared to the referenced studies.

The figure shows the H NMR spectra of Monomer 1. The synthesis was confirmed with the proton numbers and splitting's in the HNMR spectrum. To calculate the proton number with the normalization method, the proton in position 5 is assumed to be 1. Signals observed from protons 2 and 5 indicate aromatic protons. Signals in the 1-2 ppm range indicate an aliphatic environment.

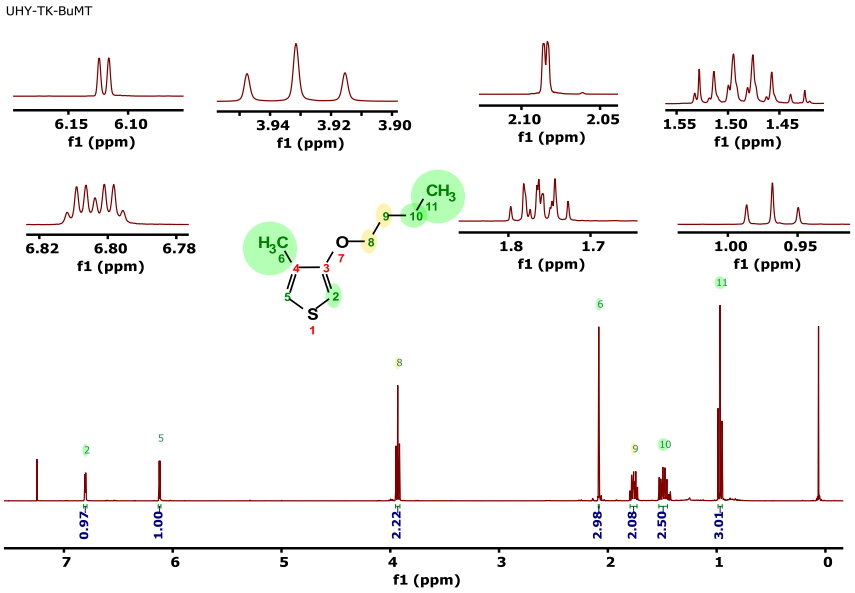

Figure 3.1. ^{1}HNMR spectrum of the Monomer 1

Monomer 1 was confirmed with the ^{13}CNMR spectrum. The signals seen in the range of 130-160ppm indicate carbons in the aromatic ring. The low chemical shift suggests an aliphatic carbon between 10-30ppm. The presence of nine different signals in the spectrum gives the number of C in the molecule. ^{13}C NMR (400 MHz, $CDCl_3$) δ 156.28, 129.26, 119.65, 95.79, 77.32, 77.00, 76.69, 69.67, 31.28, 19.29, 13.88, 12.68.

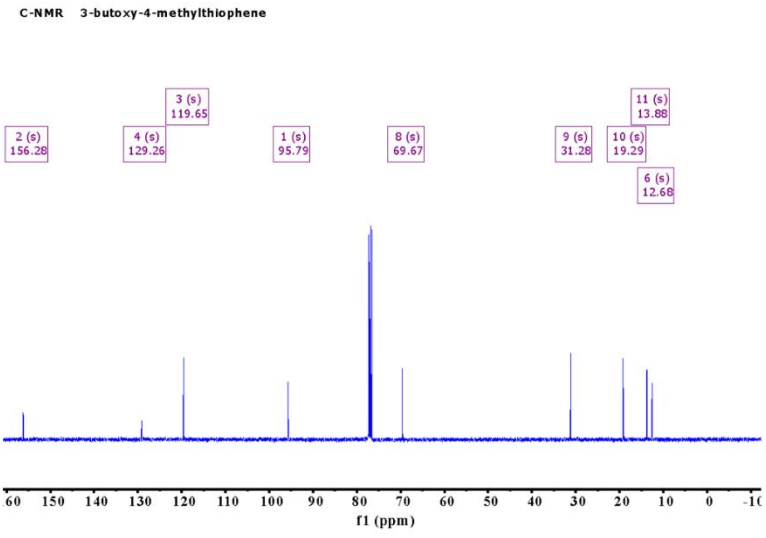

Figure 3.2 ^{13}CNMR spectrum of the Monomer 1

3.1.2.Characterization of Monomer 2

Synthesis of monomer 2 is achieved through 3-step reactions. For precursor 1, it is performed by substitution reaction between 3-bromo-4-methylthiophene and NaOMe. The reaction was catalyzed by Cu(I)Br (Copper(I) bromide), NMP used as solvent in this reaction. The reaction takes place at 110°C for 72 hours. Then, precursor 1 reacts with 3-bromopropanol in Toluene to synthesize precursor 2. The obtained precursor 2 is then reacted with diallyl methylamine to synthesize monomer 2.

The figure shows the H NMR spectra of Monomer 2. To calculate the proton number with the normalization method, the proton in position 2 is assumed to be 1. Signals observed from protons 2 and 5 indicate aromatic protons. Moreover, signals in the 5.8-6.2 ppm range indicate C=C double bonds terminal groups of the monomer.

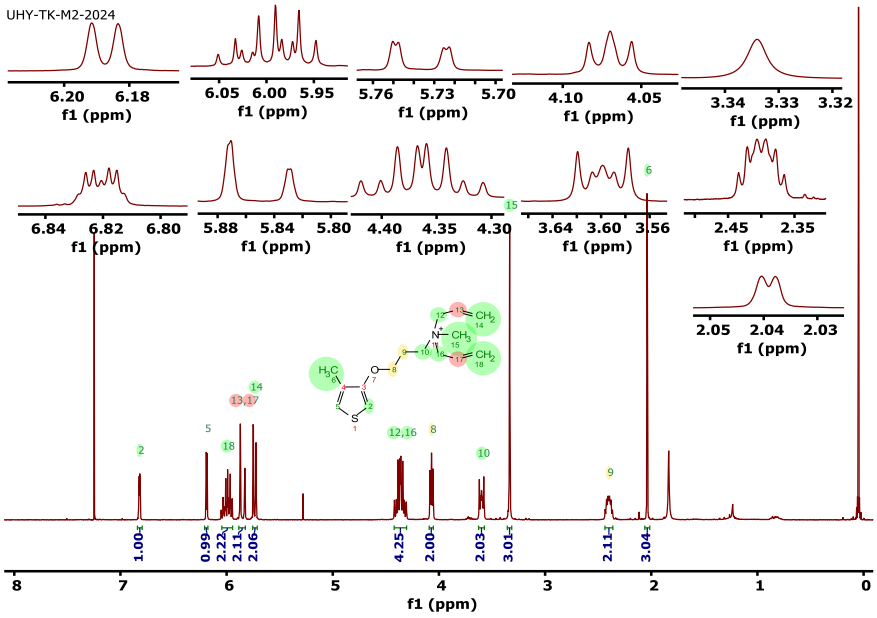

Figure 3.3 ^{1}HNMR spectrum of the Monomer 2

Monomer 2 was confirmed with the CNMR spectrum. The signals seen in the range of 120-160ppm indicate carbons in the aromatic ring and terminal C=C double bonds. The presence of 12 different signals in the spectrum gives the number of C, which are not symmetric in the molecule.

(^{13}C NMR (400 MHz, $CDCl_3$) δ 154.79, 130.23, 129.98, 128.37, 124.02, 123.85, 120.50, 97.23, 77.34, 77.02, 76.71, 65.87, 63.70, 22.95, 12.74.)

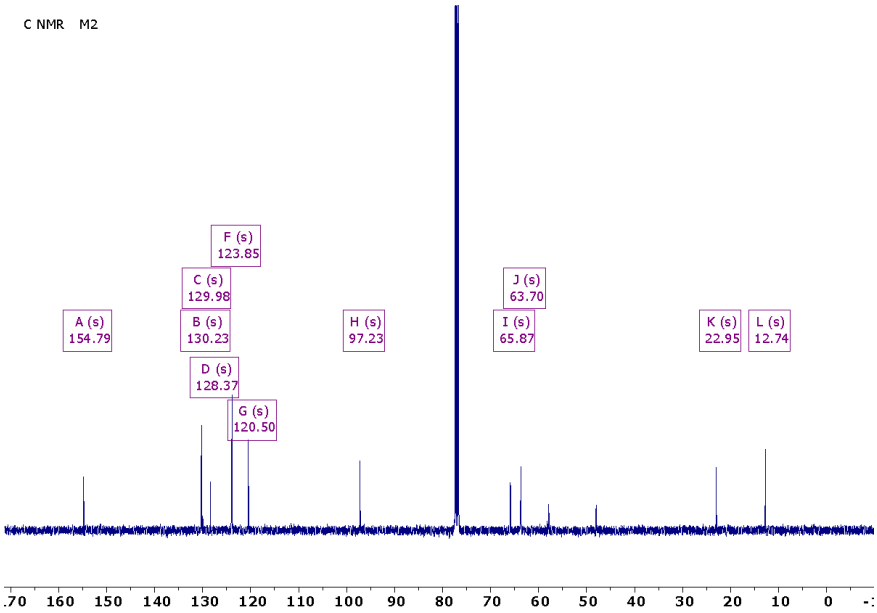

Figure 3.4 ^{13}CNMR spectrum of the Monomer 2

This mass spectrometry result shows the mass/charge ratio (m/z) of the compound analyzed under positive electrospray ionization (+ESI). A single and intense peak at 266.23464 m/z was observed in the spectrum. No other peak or fragmentation product was observed in the spectrum, indicating that the sample was of high purity and the ionization process was successful. The signal intensity of approximately 8 x 10^7 supports the presence of sufficient amounts of the analyte and that the analysis conditions were appropriate. This result indicates the presence of the targeted compound and can be said to support NMR analysis for definitive structure confirmation.

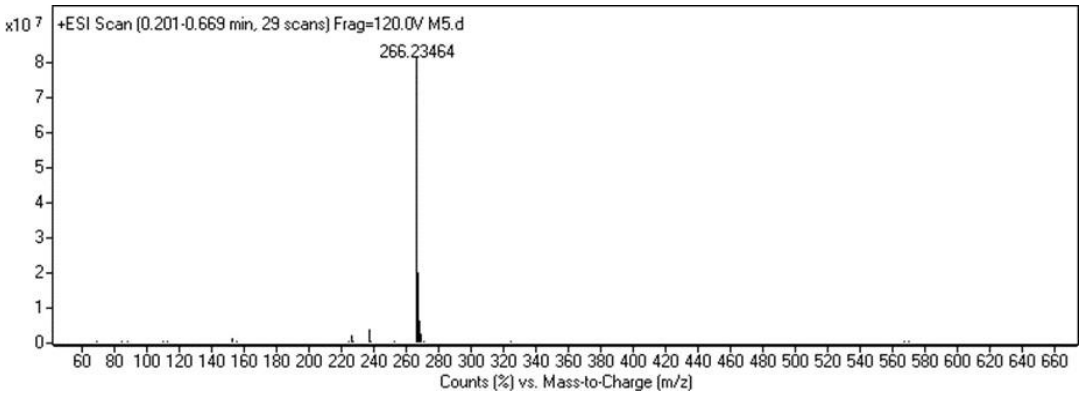

Figure 3.5 MALDI-TOF-MS Spectrum of Monomer 2

3.2. Characterization of the Polymers

3.2.1. ^{1}HNMR spectrums of the Polymers

Proton Nuclear Magnetic Resonance (H-1 NMR) spectroscopy is a powerful characterization method that allows detailed investigation of the molecular structure, composition and dynamic properties of polymers. Unlike small molecule H-1 NMR analysis, polymer spectra usually show broader peaks and overlapping signals due to chain heterogeneity and complex molecular structure. Figures demonstrate the ^{1}H-NMR spectra of P1, P2, P3, P4, P5, P6 and P7 polymers.

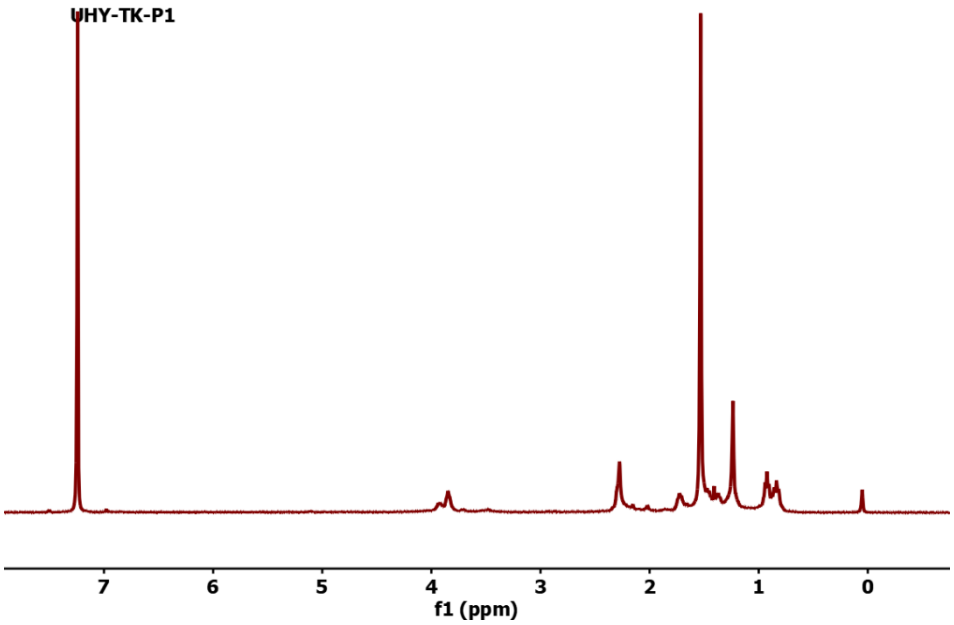

Figure 3.6 ^{1}H-NMR spectra of the P1 polymer.

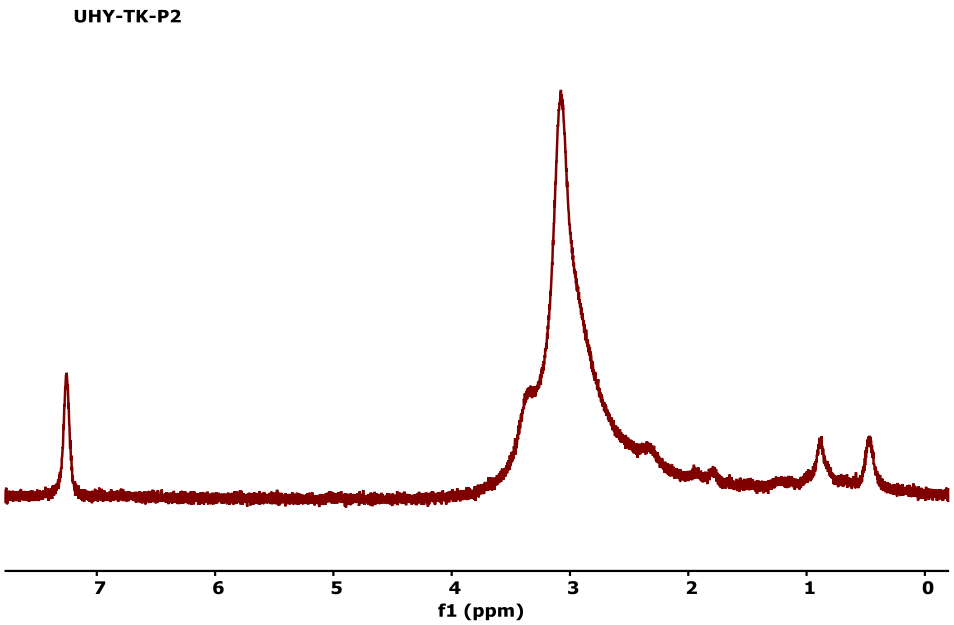

Figure 3.7 ^{1}H-NMR spectra of the P2 copolymer.

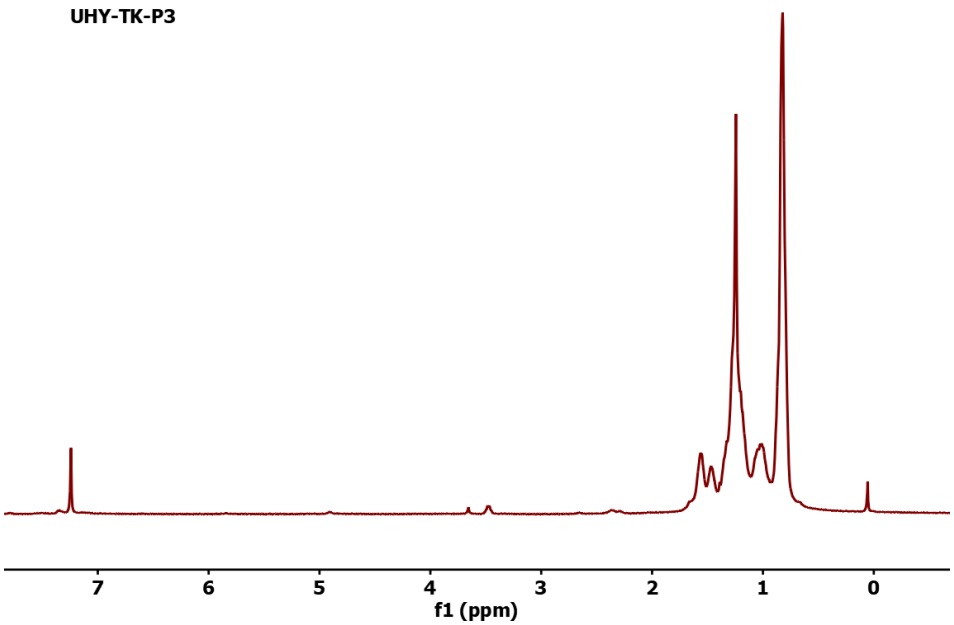

Figure 3.8 ^{1}H-NMR spectra of the P3 copolymer.

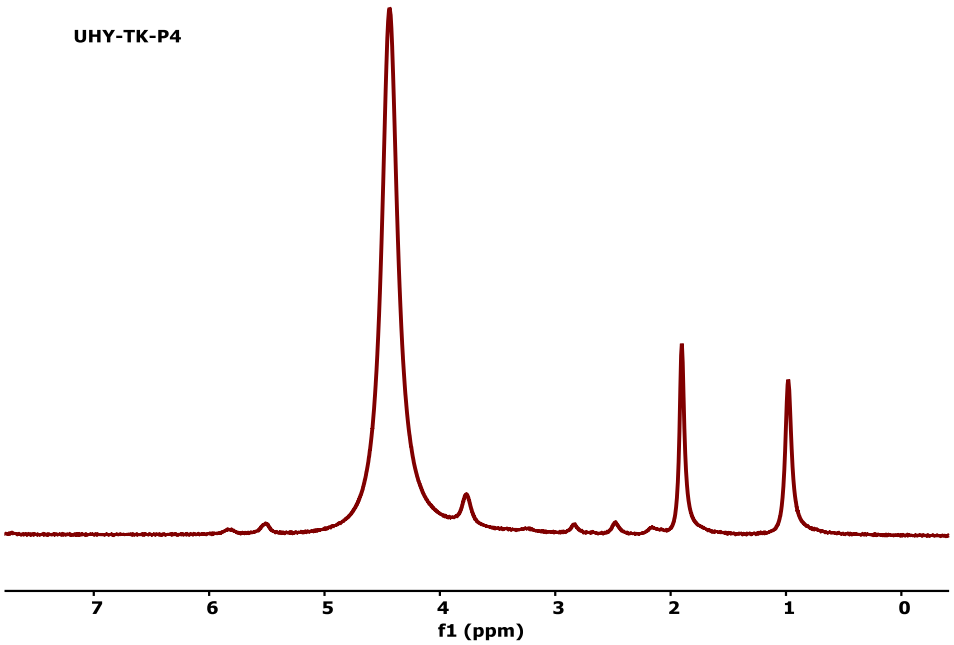

Figure 3.9 ^{1}H-NMR spectra of the P4 copolymer.

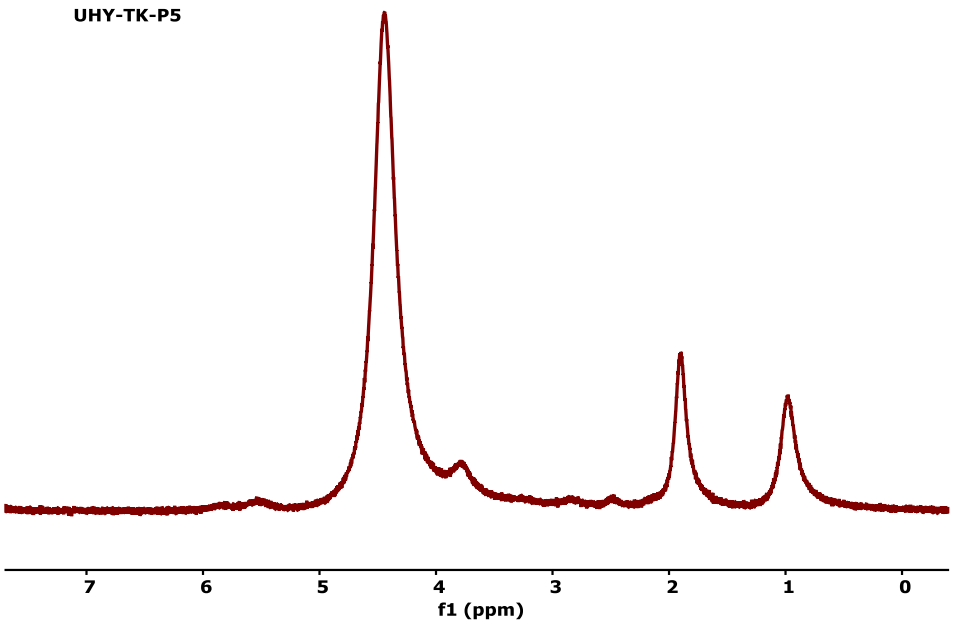

Figure 3.10 ^{1}H-NMR spectra of the P5 copolymer.

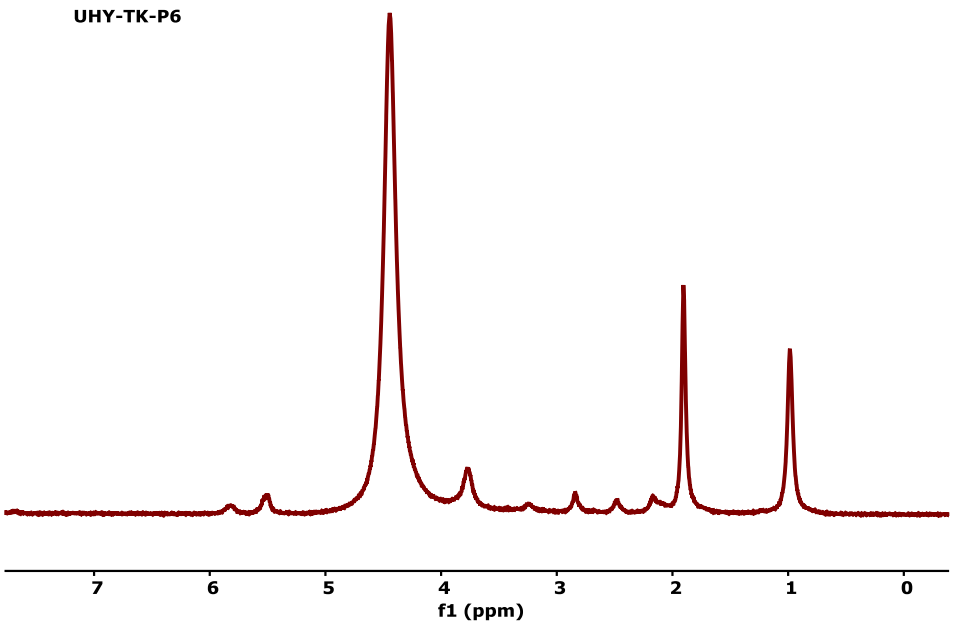

Figure 3.11 ^{1}H-NMR spectra of the P6 copolymer.

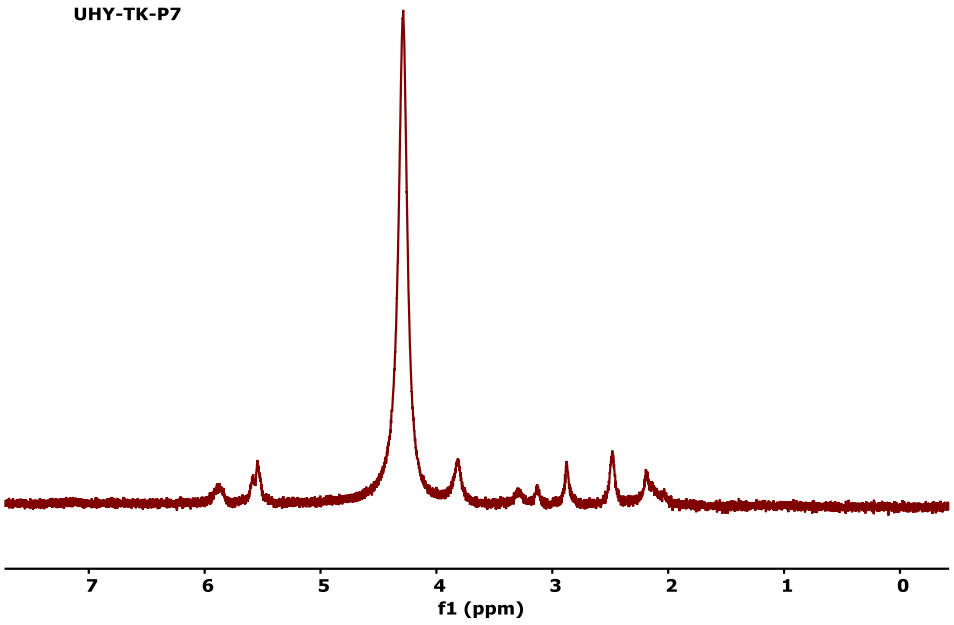

Figure 3.12 ^{1}H-NMR spectra of the P7 homopolymer.

As the M1 ratio in polymers increases, broadened peaks in the range of 1-3 ppm are observed to become dominant. This broadening is due to the structural properties of the M1 monomer and is clear in the proton NMR spectrum of the polymer.

As the M2 ratio in polymers increases, spectra with high intensity peaks in the range of 4-5 ppm are observed. These peaks become especially pronounced due to the binding of ethylene groups to amine groups. The effect of ethylene groups leads to the formation of intense signals in the range of 4-5 ppm and is clearer in the proton NMR spectrum of the copolymer.

P1-P2 and P3 analyzed in $CDCl_3$ due to their hydrophobic nature. P4-P5-P6 and P7 were analyzed in D_2O because of their higher hydrophobicity.

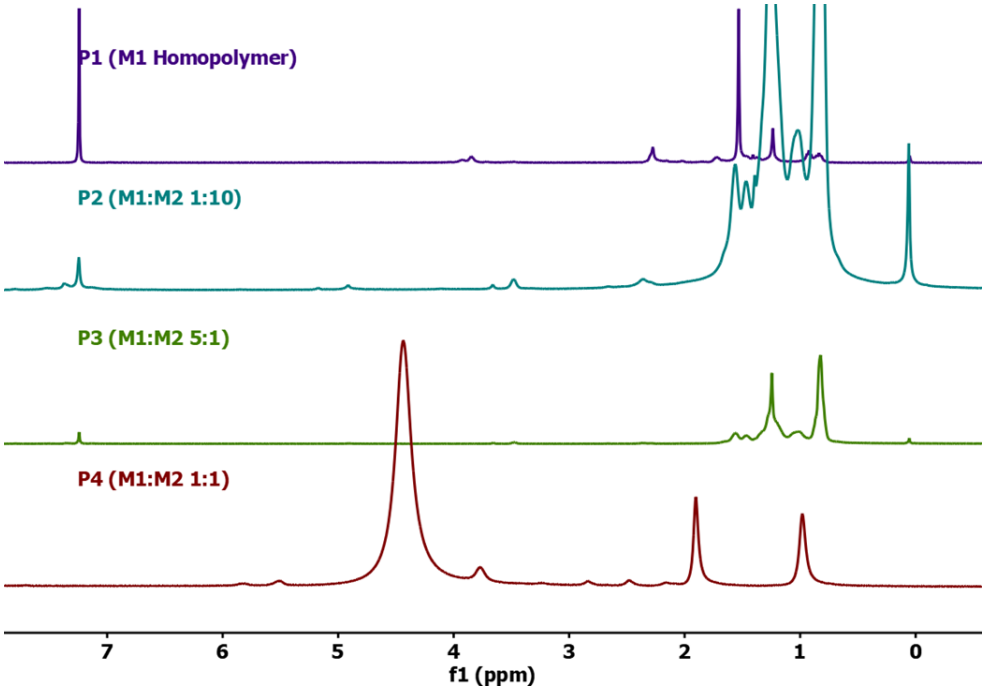

Figure 3.13. Stack Illustration of P1-P4 ^{1}H-NMR Spectrum

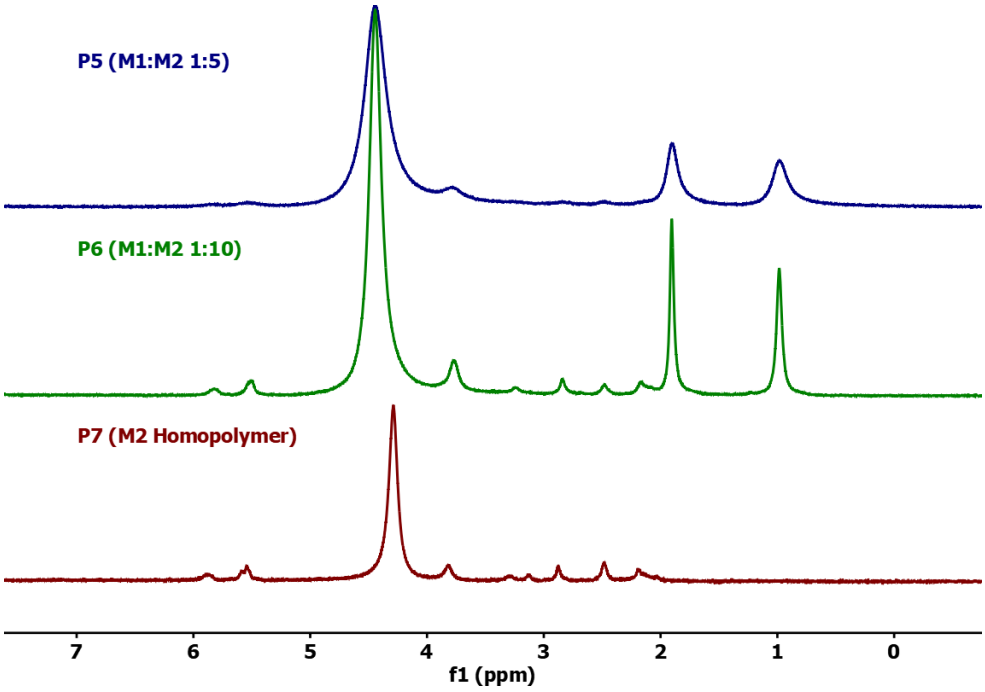

Figure 3.14. Stack Illustration of P5-P7 ^{1}H-NMR Spectrum

3.2.2.. MALDI-TOF MS Analysis of Polymers

Figure 3.15 shows the chemical structure and mass spectrum of the P1 polymer synthesized using the M1 monomer. The signals seen between 0-2000 m/z in Figure 1 can be thought to originate from relatively low-mass oligomers. The elements showing lower signal intensity in the 2500-3500 m/z range are thought to originate from the P1 polymer. The low signal intensity is due to the ionization barriers of the high-mass polymers. Considering that the average mass distribution is at the 3000m/z center and considering the M1 monomer weight (170g/mol), it was concluded that the average degree of polymerization (3000/170) is “18”. In Figure, the 2750-2850g/mol cross-section of the P1 polymer chain is shown closely.

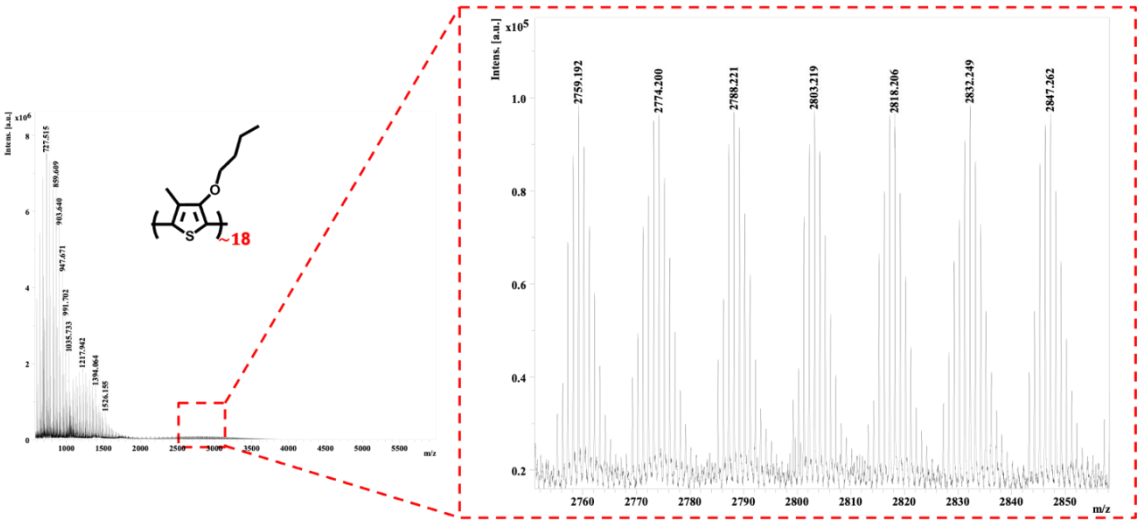

Figure 3.15. Mass spectrum representation P1 polymer

The 1100-1400 g/mol section of the P1 mass spectrum is shown closely in Figure 3.16. There are two clearly distinct trends in the spectrum. In both trends, a mass difference of approximately 44 a.u is seen between the signals. It is thought that these mass differences occur because of the breaking of the -O-CH2-CH2- bonds at the butoxy end attached to the thiophene ring at position 3.

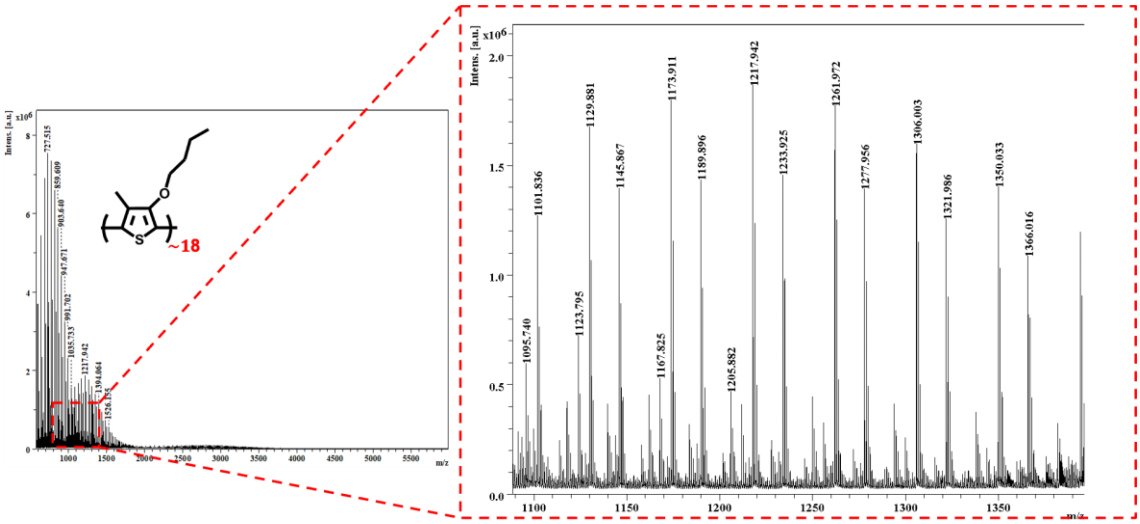

Figure 3.16. Representation of the mass spectrum of P1 polymer in the 1100-1400 au range

The structure and mass spectrum of P2 (M1:M2 10:1) polymer are shown in Figure 3.17. The molecular weight of M1 was calculated as 170.27 g/mol, and the

molecular weight of M2 was calculated as 266.42 g/mol. While the 2866.365 au value of the sample corresponding to the signal seen in Figure 3.17 was calculated as the target value, considering the initial ratios of M1 and M2, it can be thought that M2 reacted more than expected, but it can be understood that this distribution was obtained due to the increase in the M2 ratio in the chain and the acceleration of the separation of the cationic charge from the polymerization medium. 2700-2900 g/mol range of the polymer spectrum was also examined. The molecular weight difference between the peak values corresponds to 14-15au. It can be interpreted as the rupture of -CH3 and -CH2- found in the end groups of M1. For M2, it is thought to occur because of the breaking of the -CH3 or =CH2 bonds attached to the allyl group.

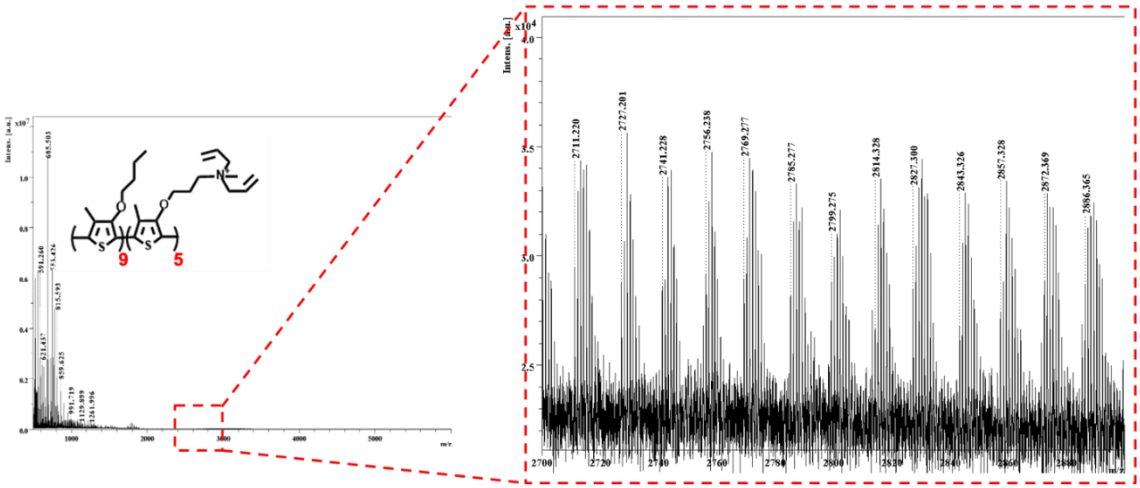

Figure 3.17. Mass spectrum representation P2 copolymer

The structure and mass spectrum of the P3 (M1:M2 5:1) polymer are shown in Figure 3.18. When the molecular weight differences between the signals are examined, changes of 14-16 a.u are observed. The molecular fragmentations that can be observed in this range may be due to the -CH3 and -CH2- and -O- degradations found in both monomers. It has been evaluated that the -O-CH2-CH2- group is located at the butoxy end attached to the thiophene ring from the 3rd position, and the low intensity signals belong to the -O-CH2-CH2- group located at the 3rd position of M2, which is relatively sparse.

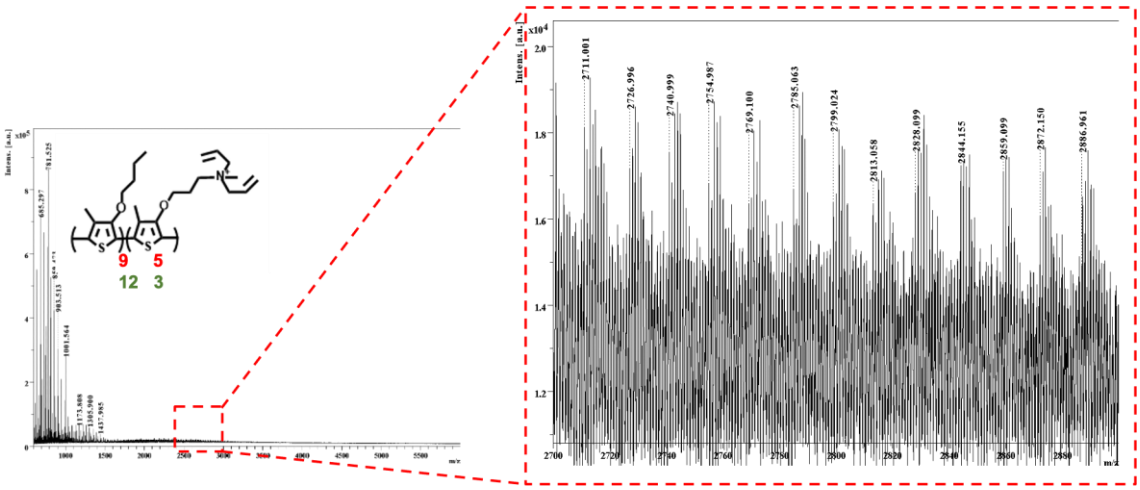

Figure 3.18. Mass spectrum representation P3 copolymer

Figure 3.19 shows the structure and mass spectrum of the polymer P4 (M1:M2 1:1). It was understood that the low signal intensity distribution observed around 3000 m/z belonged to the polymer, as in the previous examples. In the figure, signals at 14-15-16a.u values were also seen from the polymer chain for P4, as in other polymers. These signals are thought to be due to the breakage of the end groups found in both molecules, such as -CH2-, CH3- and -O-.

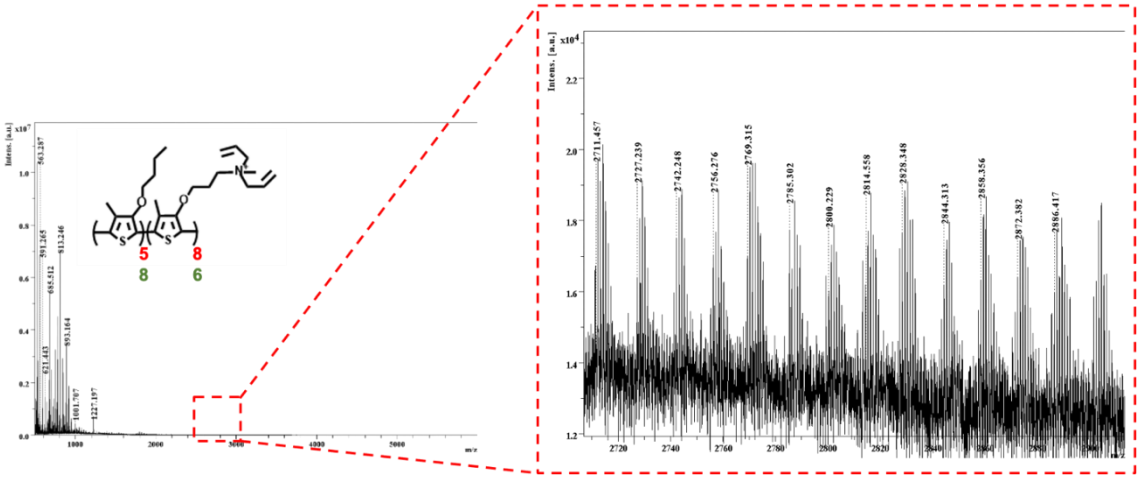

Figure 3.19. Mass spectrum representation P4 copolymer

Figure 3.20 shows P5 (M1:M2 1:5) and its mass spectrum. In this spectrum range, as in other polymers, signals of 14-15 a.u were observed from the polymer chain. These

signals are signals taken from end groups found in both molecules, such as -CH2- and CH3-.

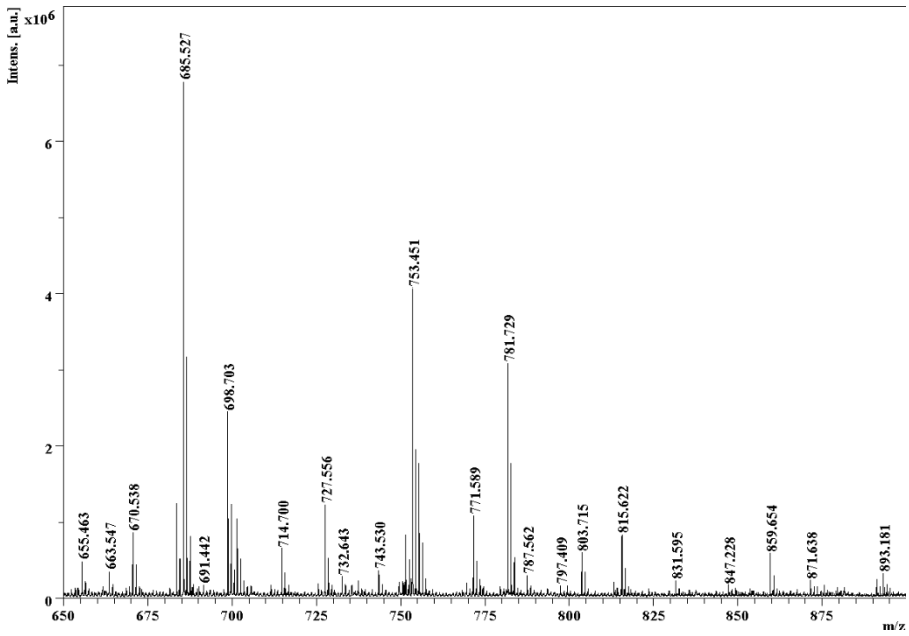

Figure 3.20. Representation of the mass spectrum of P5 (M1:M2 1:5) copolymer in the 650-900 au range

In Figure 3.21, the 650-900 g/mol section of the P5 polymer spectrum was examined. The difference in the value of 96 a.u between the 781.729 a.u and 685.527 a.u signals is the same as the molecular weight of the Diallylamine group broken off from Monomer 2. The Diallylamine end of the Diallylmethylamine group used in the transition from intermediate 2 to M2 also weighs 96 a.u. It was evaluated that the methyl group could be separated independently of this group.

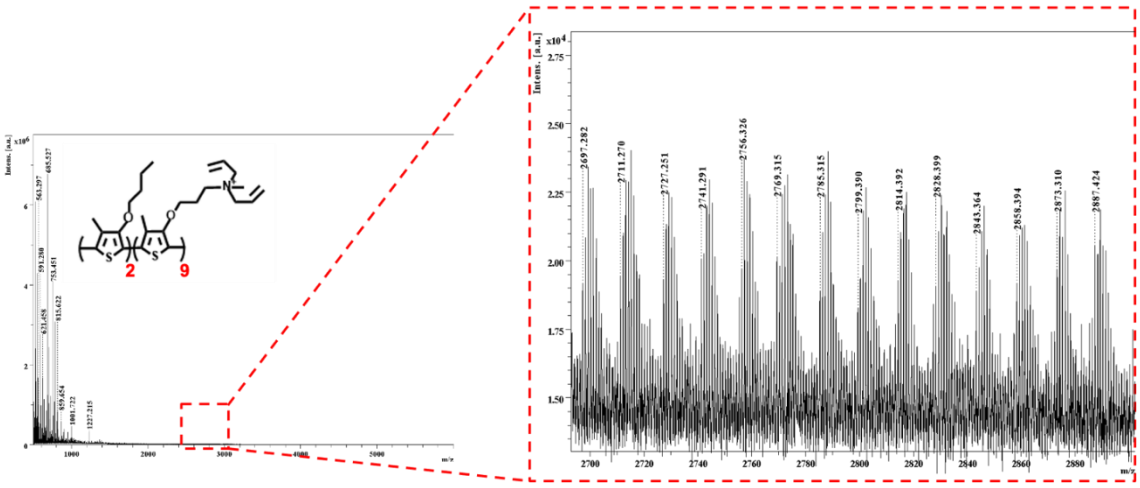

Figure 3.21. Mass spectrum representation P5 copolymer

The mass spectrum of polymer P6 (M1:M2 1:10) is shown in Figure 3.22. The set of results that gives the only possibility of matching the initial stoichiometry suggests that the dominant copolymer structure may be as suggested. The decrease in signal intensity as the M2 ratio increases suggests that the ionization efficiency of copolymers in which this monomer is concentrated is lower than that of copolymers in which the M1 monomer is dominant.

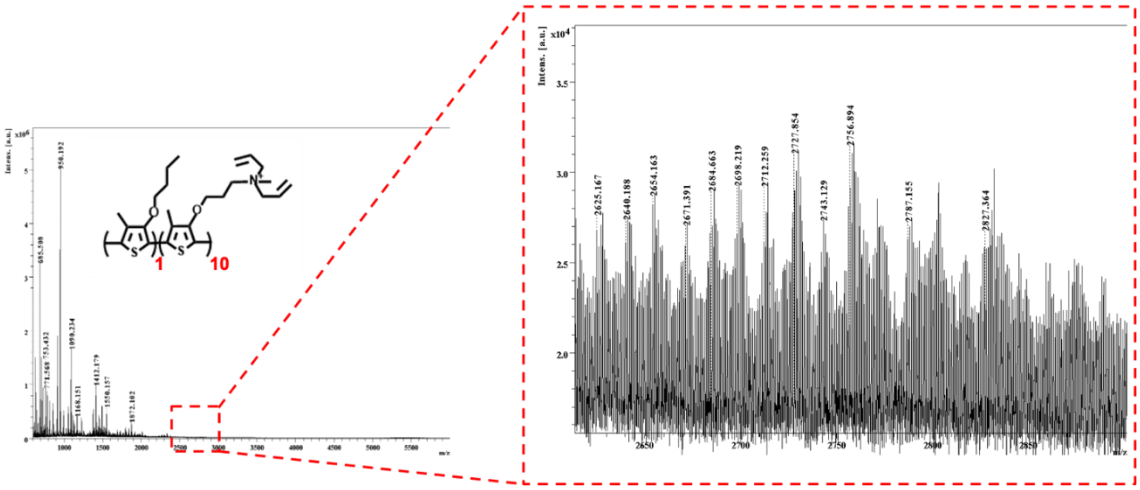

Figure 3.22. Mass spectrum representation P6 copolymer

Figure 3.23 shows the structure and mass spectrum of the polymer obtained from P7, that is, cationic monomer (M2). It is understood that polymers up to 2800 g/mol can be ionized. Considering the molecular weight of M2 (266.42 g/mol), it is calculated that

the polymers obtained with the help of the spectrum consist of polymer chains of 11 monomers.

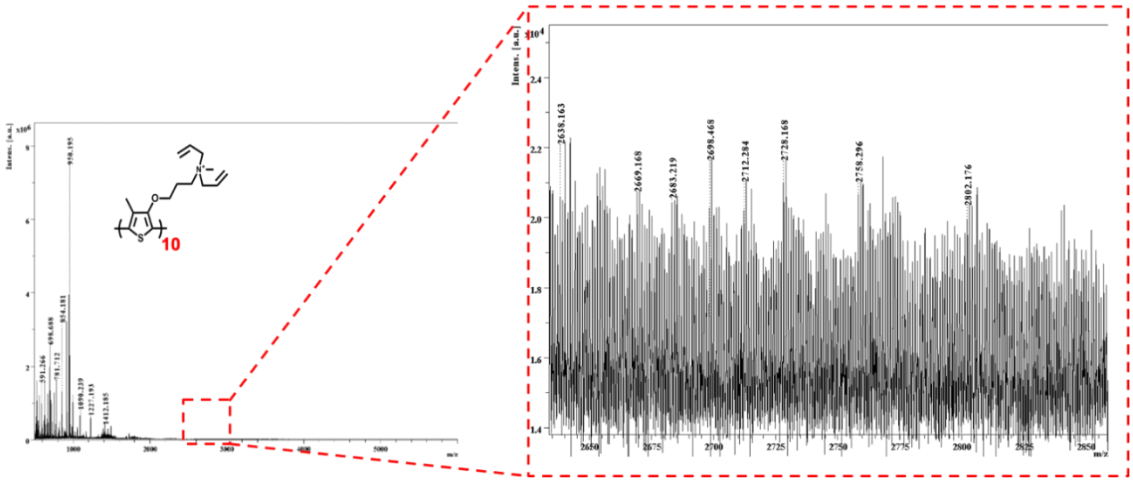

Figure 3.23. Mass spectrum representation P7 polymer

3.2.3. Optical Characteristics of the Polymers

The P1 polymer, a homopolymer composed entirely of Monomer 1, was optically characterized through UV and fluorescence spectroscopy. The maximum absorbance wavelength of P1 dissolved in chloroform was measured as 435 nm. In the subsequent fluorescence spectroscopy analysis, excitation wavelength is 400 nm), the maximum emission wavelength was determined as 550 nm.

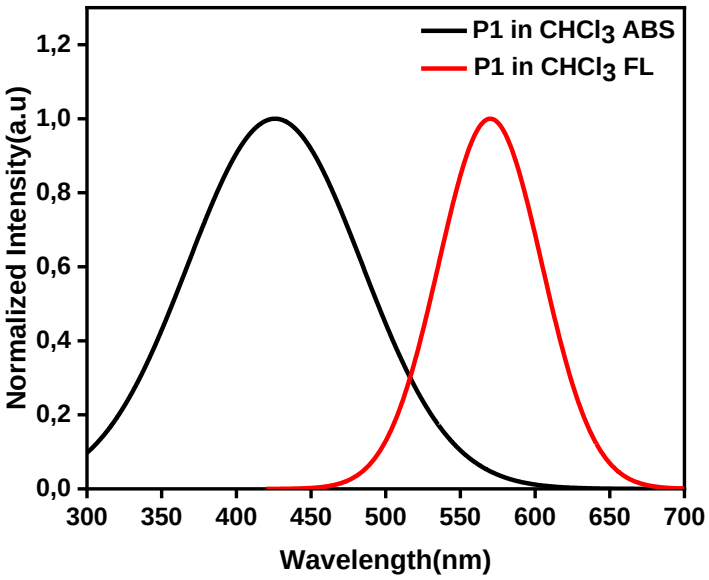

Figure 3.24 Normalized Absorbance Fluorescence Spectrums of the P1 in $CHCl_3$

The normalized UV spectrum of the P2 (copolymer, which contains M1/M2 in a 10:1 ratio) has the absorbance maximum wavelength of P2 polymer was measured as 343 nm. In the subsequent fluorescence spectroscopy analysis, (λ_{ex} at 340 nm) the emission maximum wavelength was determined as 580 nm.

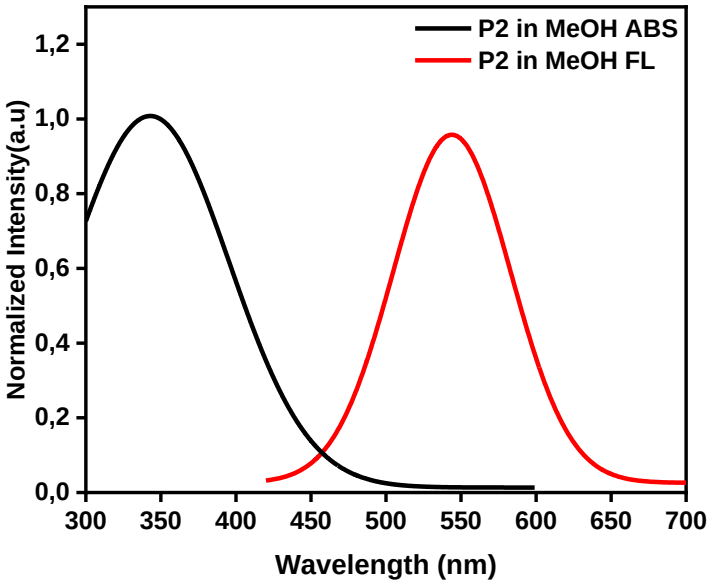

Figure 3.25. Normalized Absorbance Fluorescence Spectrums of the P2 in MeOH

The normalized UV spectrum of the P3 (copolymer, which contains M1/M2 in a 5:1 ratio), could be analyzed in methanol due to its partially soluble structure. When dissolved in methanol, the P3 polymer showed absorbance maximum wavelength of 366 nm. In subsequent fluorescence spectroscopic analysis, (λ_{ex} at 400 nm) P3 gave emission maximum (λ_{em}) at 550 nm.

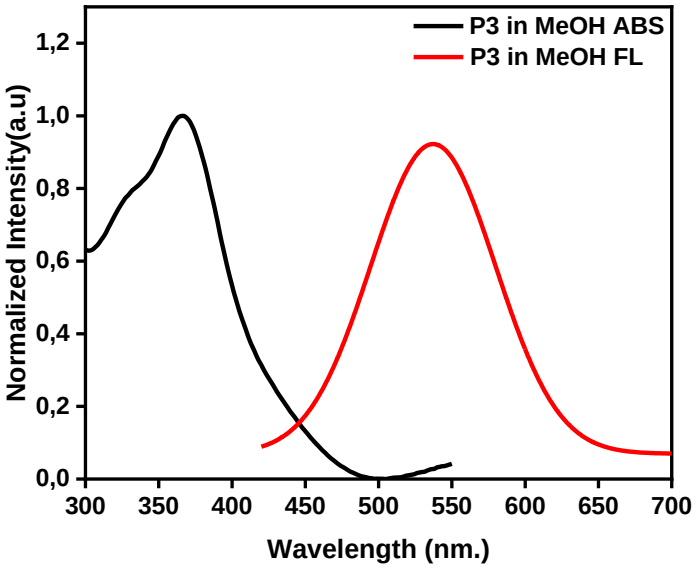

Figure 3.26. Normalized Absorbance Fluorescence Spectrums of the P3 in MeOH

The normalized UV spectrum of P4, a copolymer containing M1 and M2 in a 1:1 ratio, was analyzed in methanol due to its partial solubility in this solvent. When dissolved in methanol, P4 exhibited an absorbance maximum at 367 nm. Subsequent fluorescence spectroscopic analysis, with an excitation wavelength (λ_{ex}) of 370 nm, revealed an emission maximum (λ_{em}) at 543 nm.

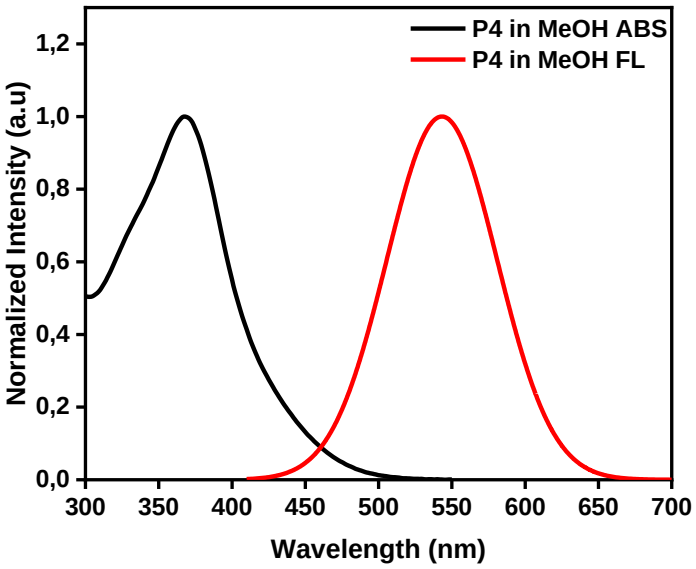

Figure 3.27. Normalized Absorbance Fluorescence Spectrums of the P4 in MeOH

The normalized UV spectrum of P5, a copolymer containing M1/M2 in a 1:5 ratio, was analyzed in methanol. When dissolved in methanol, the P5 polymer exhibited an absorbance maximum at 375 nm. In subsequent fluorescence spectroscopic analysis, with an excitation wavelength (λ_{ex}) of 400 nm, P5 showed an emission maximum (λ_{em}) at 544 nm.

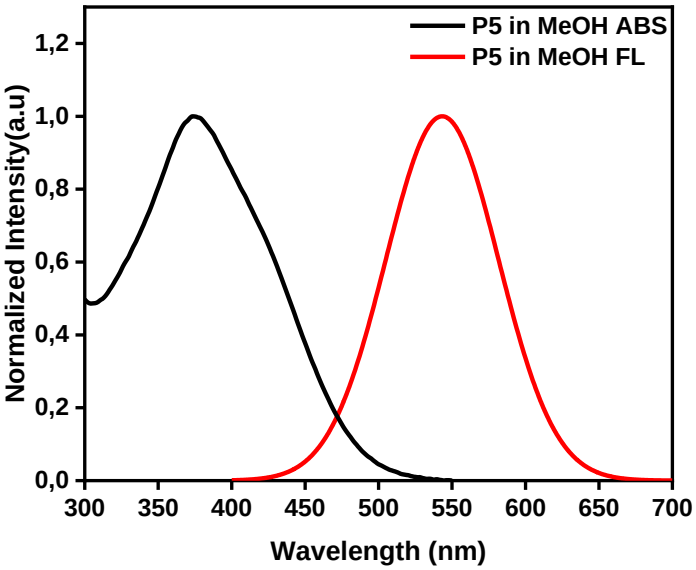

Figure 3.28. Normalized Absorbance Fluorescence Spectrums of the P5 in MeOH

The normalized UV spectrum of the P6 (copolymer, which contains M1/M2 in a 1:10 ratio), could be analyzed in methanol due to its partially soluble structure. When dissolved in methanol, the P6 polymer showed absorbance maximum wavelength of 381 nm. In subsequent fluorescence spectroscopic analysis, (λ_{ex} at 300 nm) P3 gave emission maximum (λ_{em}) at 546 nm.

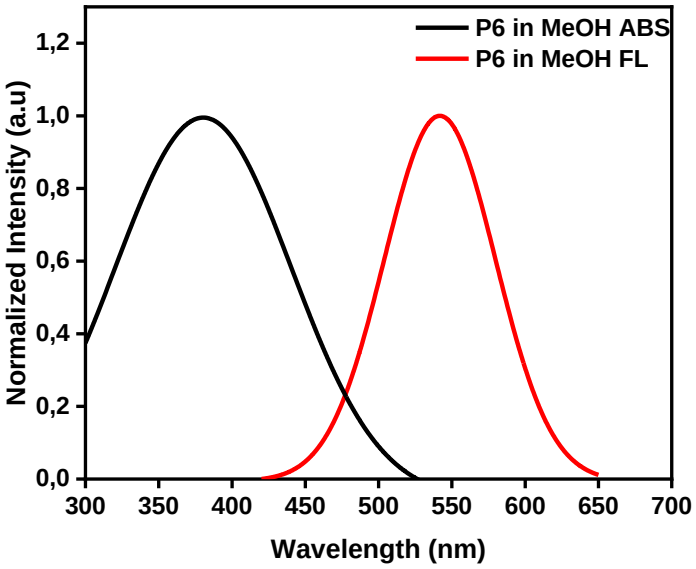

Figure 3.29. Normalized Absorbance Fluorescence Spectrums of the P6 in MeOH

The P7 polymer, a homopolymer composed entirely of Monomer 2, was optically characterized through UV and fluorescence spectroscopy. When dissolved in methanol, the UV spectrum of P7, obtained with an excitation wavelength of 350 nm, displayed a maximum absorbance at 435 nm. In the subsequent fluorescence spectroscopic analysis, with an excitation wavelength (λ_{ex}) of 400 nm, the P7 homopolymer exhibited an emission maximum (λ_{em}) at 542 nm.

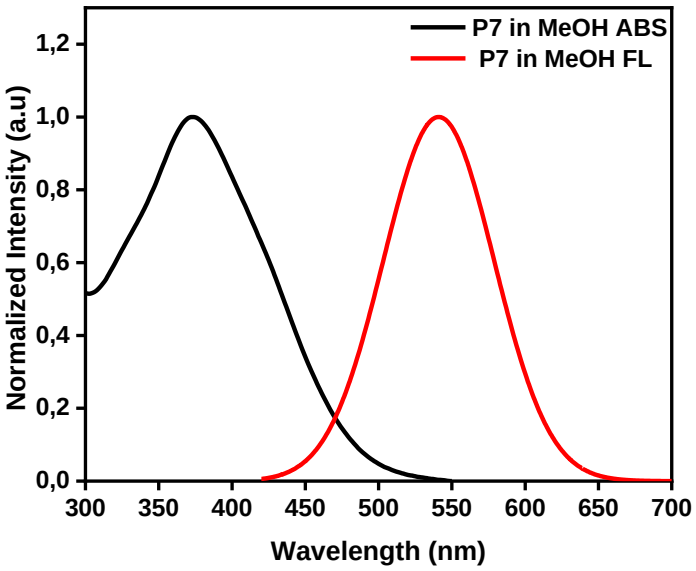

Figure 3.30. Normalized Absorbance Fluorescence Spectrums of the P7 in MeOH

Table 3.1. Normalized Absorbance Fluorescence λmax of Polymers

Polymer Name	**Polymer Ratio M1:M2**	**ABS-FL λmax of the Polymers**
P1	Homopolymer	435nm-550nm
P2	10:1	343nm-550nm
P3	5:1	366nm-550nm
P4	1:1	367nm-543nm
P5	1:5	375nm-544nm
P6	1:10	381nm-546nm
P7	Homopolymer	373nm-542nm

3.2.4. Dynamic Light Scattering Analysis of the MeOH Rinsed Polymers

For DLS analysis, samples were prepared in Methanol and Ethylene Glycol at a concentration of 0.1 mg/ml. Three consecutive measurements were conducted, and the hydrodynamic radius of the polymers were calculated. These analysis is done with the correlation function, which is a mathematical function that examines how the scattered light changes over time to measure the size of the particles.

Polymer Dots with the Nanophase separation method and the formed Pdot solutions were examined as well. The stock polymer solution prepared by x mg/ 1mL in ethylene glycol or in methanol is then diluted 10 fold or 30 fold with water. All diluted samples were subjected to sonication for 1 hour.

In Figure 3.31, polymer solutions dissolved in methanol exhibit particle diameters of approximately 100 nm. In Figure 3.33, when the polymers were diluted with water at a 1:10 ratio, most of the polymer solutions showed reduced particle sizes, except for P2 and P7, which formed nanoparticles with diameters around 10 nm. In Figure 3.35, when the polymer solutions were further diluted at a 1:30 ratio, smaller nanoparticles were observed compared to both the 1:10 dilution and methanol-based analyses. To evaluate the effect of sonication on particle size, diluted polymer solutions were sonicated at room temperature for 1 hour, and the measurements were repeated. In Figure 3.37, sonication of the 1:10 diluted polymer solutions was effective only for P5 and P6, where nanoparticles with diameters around 10 nm were observed. Finally, in Figure 3.39, sonication of the 1:30 diluted polymer solutions resulted in a higher nanoparticle intensity compared to the 1:10 dilution, indicating a more pronounced effect at the higher dilution ratio.

In Figure 3.41, the polymers dissolved in ethylene glycol (EG) exhibit diameters of approximately 100 nm. In Figure 3.43, the polymers were diluted with water at a 1:10 ratio, they were spread across a wide range on the graph, suggesting that polymers of various sizes are freely distributed in the environment. Nanoparticles around 10 nm were also observed. In Figure 3.45, polymers were diluted with water at a 1:30 ratio, smaller nanoparticles were observed compared to the 1:10 dilution. Figures 3.47 and 3.49 show that both 1:10 and 1:30 diluted polymer solutions were sonicated at room temperature for

1 hour, and the aqueous analyses were repeated. Upon comparison, polymers that had broader spectra before sonication exhibited a more limited size distribution after sonication, indicating a more uniform particle size distribution following the treatment.

In figure 3.31. Dynamic Light Scattering Intensity/Size spectrums show size distribution analysis of P2-P7 in methanol, (stock concentration is 0.1 mg/ mL) the results imply that all polymers exhibit hydrodynamic radius around 100 nm.

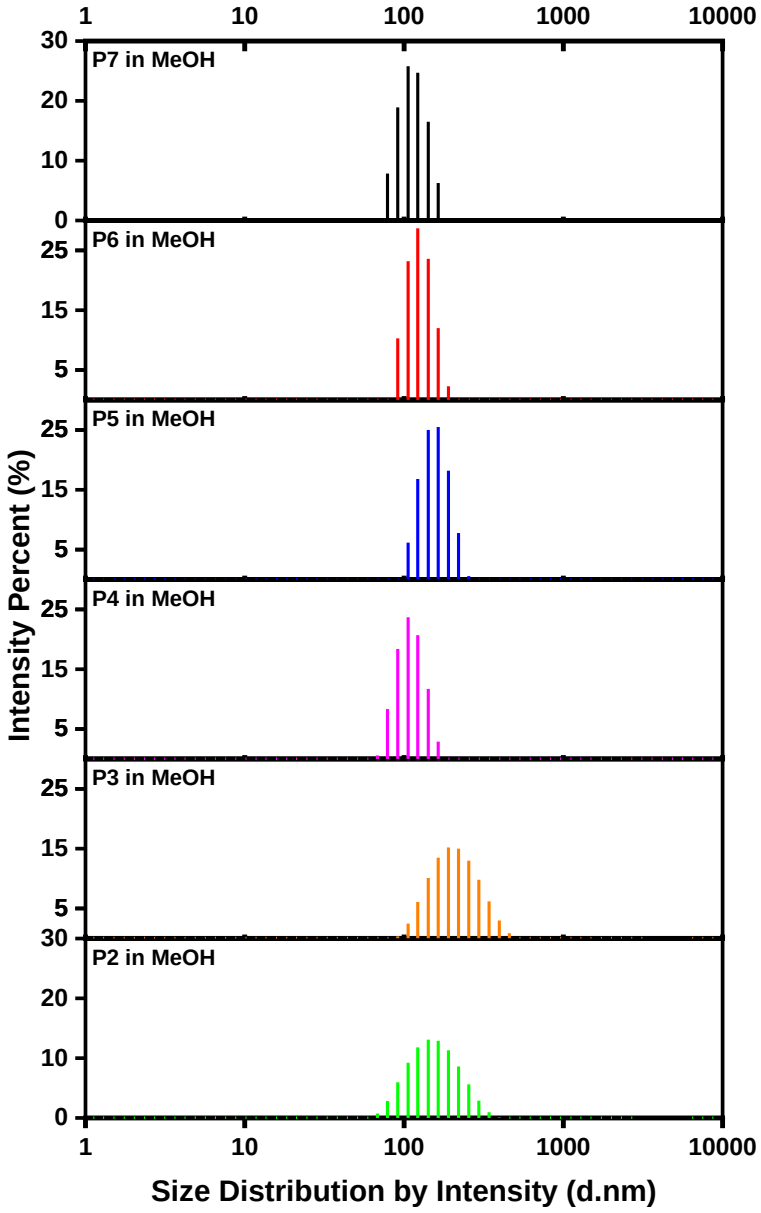

Figure 3.31. Dynamic Light Scattering Intensity/Size spectrums of P2-P7 in MeOH

In Figure 3.32. Spectrums show intensity autocorrelation versus time graph of P2-P7 in methanol, (stock concentration is 0.1 mg/ mL) as all polymers exhibit multi modal type decay time distributions.

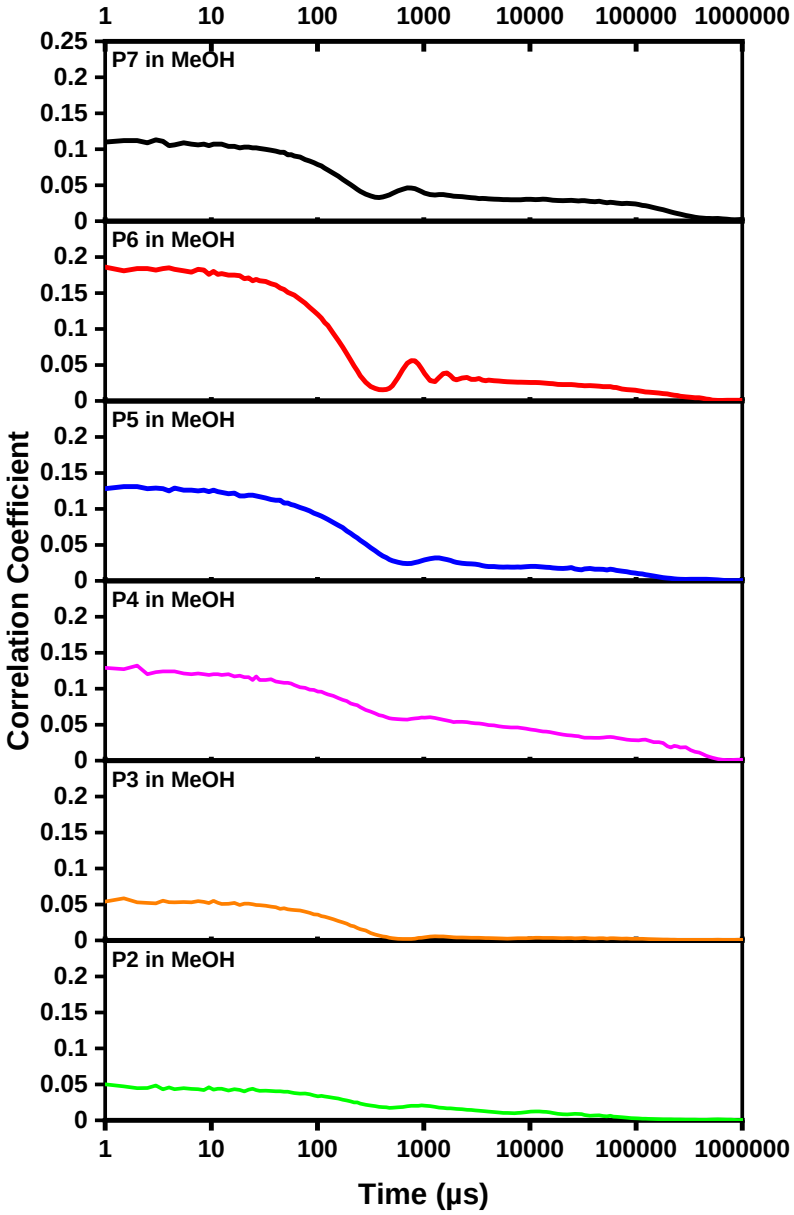

Figure 3.32. Dynamic Light Scattering Correlation/Time spectrums of the P2-P7 in MeOH

Figure 3.33. Intensity/Size spectrums show size distribution analysis of P2-P7 in 1:10 MeOH/W. P6 and P5 contain narrow and small-sized particles (~10-50 nm), P4 contains distinct populations with double peaks, and P2 and P7 contain broad and large-sized particles (~100 nm).

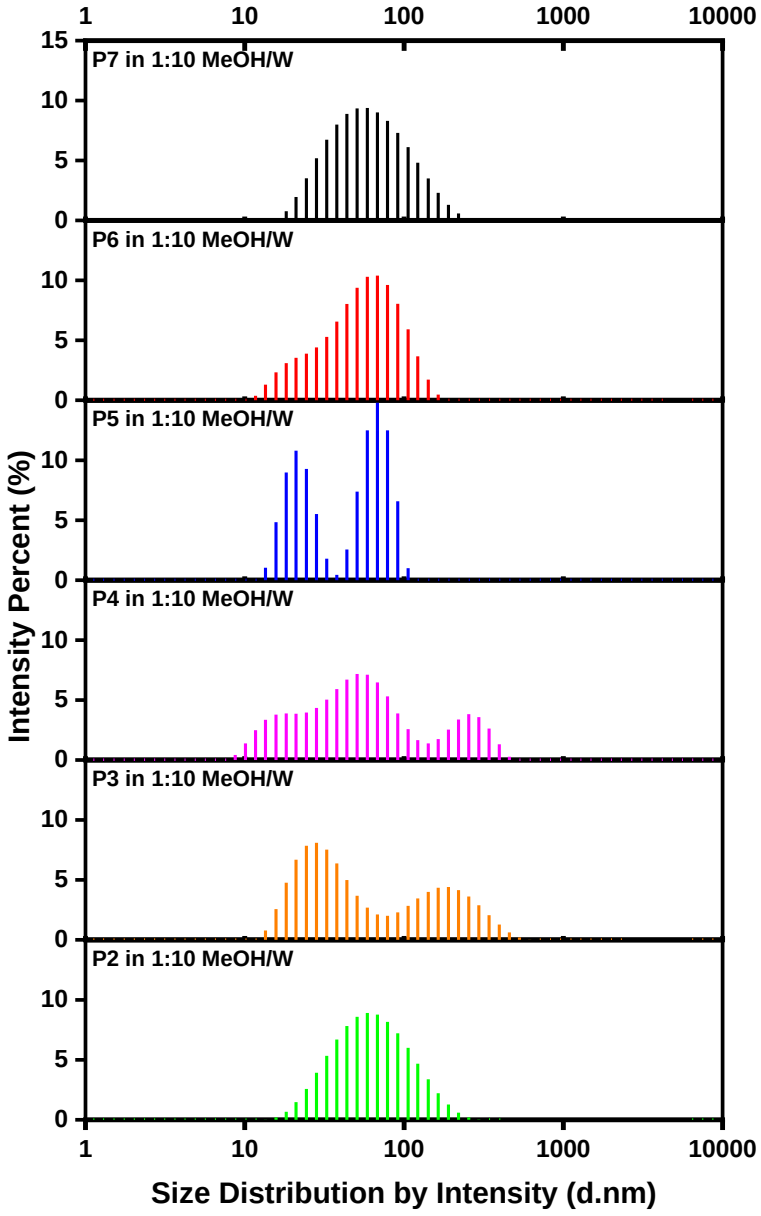

Figure 3.33. Dynamic Light Scattering Intensity/Size spectrums show size distribution analysis of P2-P7 in 1:10 MeOH/W

In Figure 3.34. Spectrums show intensity autocorrelation versus time graph of P2-P7 in 1:10 MeOH/W, (stock concentration is 0.01 mg/ mL) All polymers exhibit the similar type of decay time distribution.

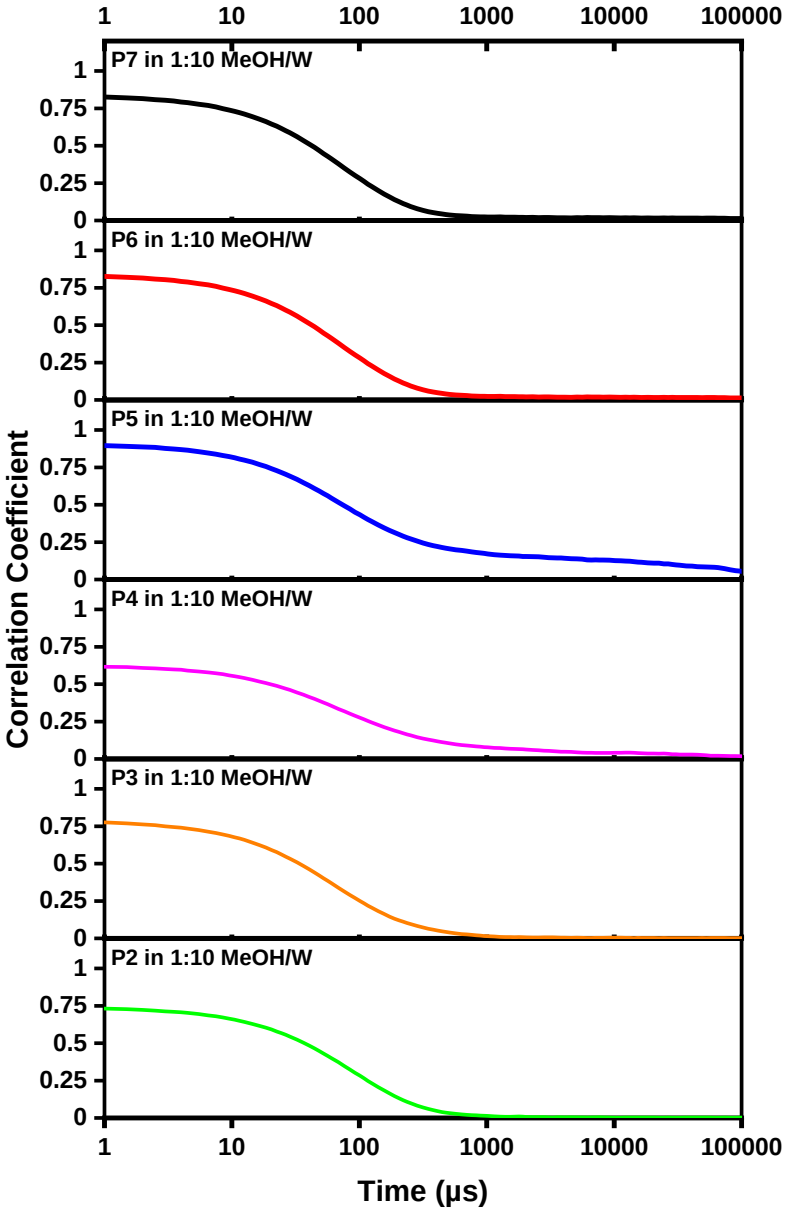

Figure 3.34. Dynamic Light Scattering Correlation/Time spectrums of the P2-P7 in 1:10 MeOH/W

In Figure 3.35 Dynamic Light Scattering Intensity/Size spectrums show size distribution analysis of P2-P7 in 1:30 MeOH/W, P3 and P7 contain narrow (50-100nm) and, P6 contain small-sized particles (~10-50 nm), P4 contains distinct populations with double peaks, and P2, P5 and P7 contain broad and large-sized particles (~100 nm).

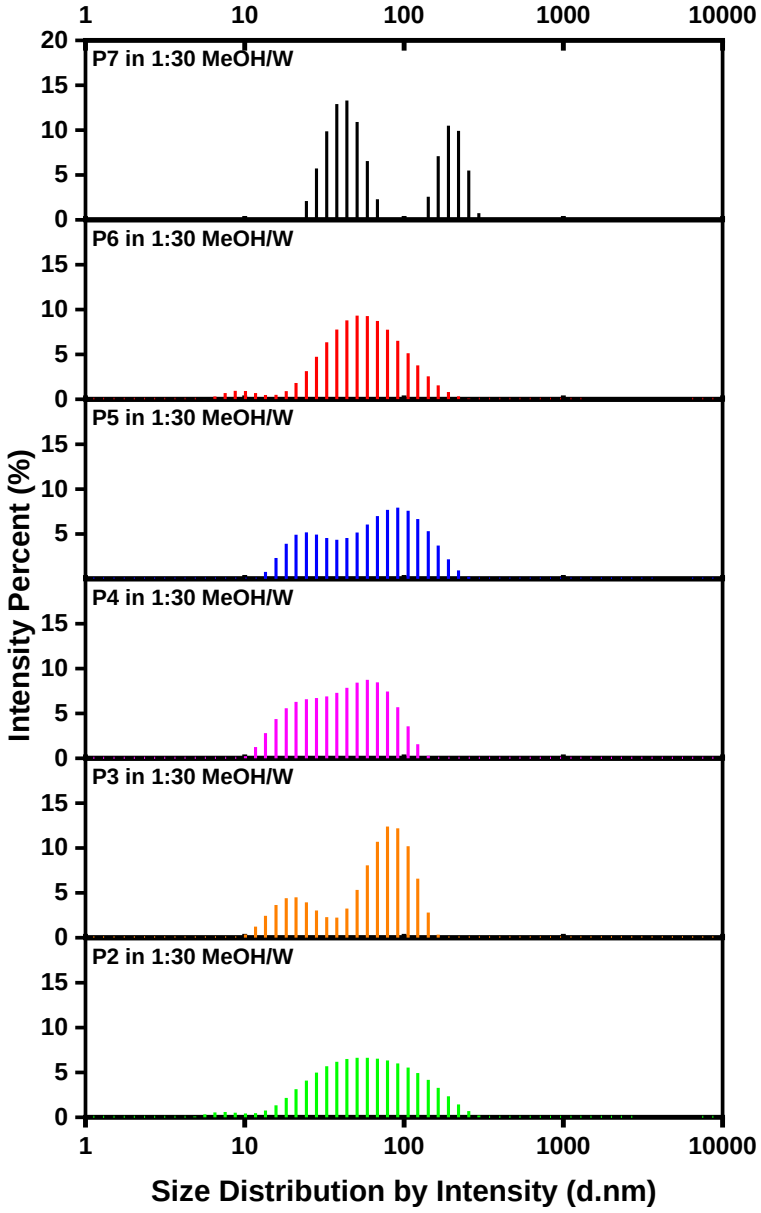

Figure 3.35. Dynamic Light Scattering Correlation/Time spectrums of the P2-P7 in 1:30 MeOH/W

In Figure 3.36. Spectrums show intensity autocorrelation versus time graph of P2-P7 in 1:30 MeOH/W, (stock concentration is 0.003 mg/ mL) All polymers exhibit the same type of decay time distribution except P7.

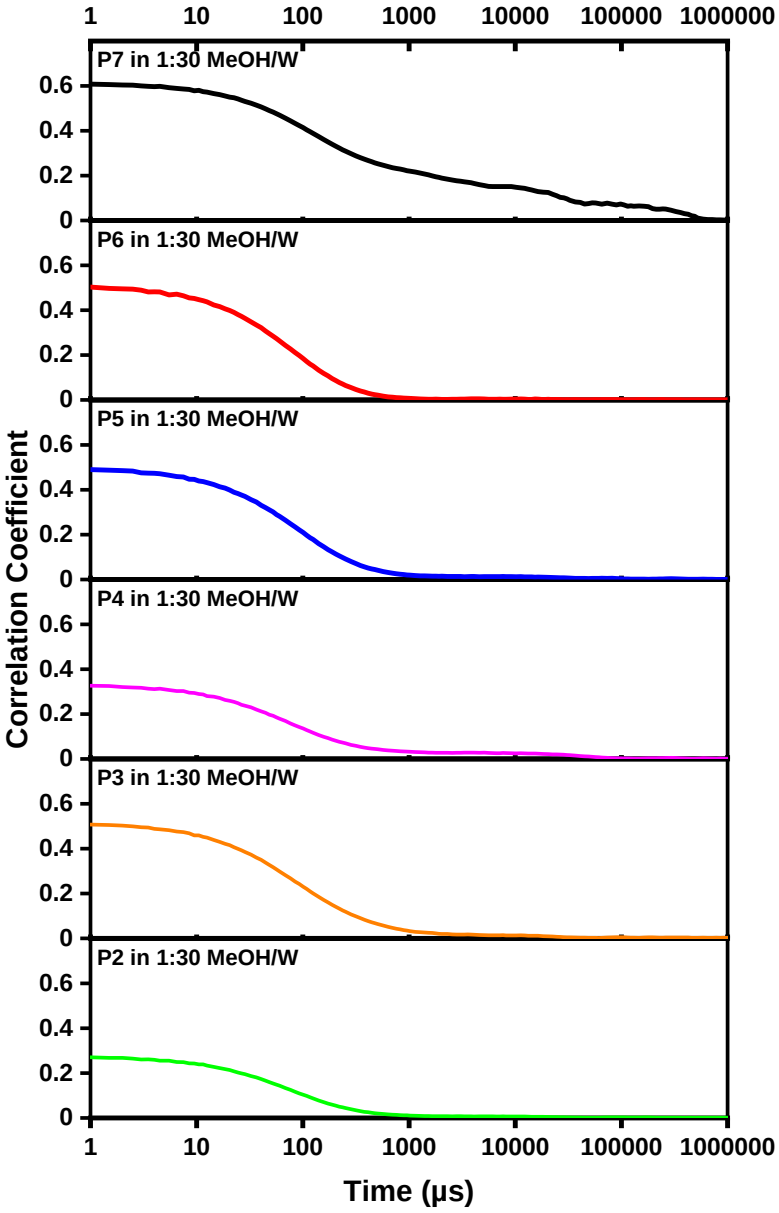

Figure 3.36. Dynamic Light Scattering Correlation/Time spectrums of the P2-P7 in 1:30 MeOH/W

In Figure 3.37. Dynamic Light Scattering Intensity/Size spectrums show size distribution analysis of P2-P7 in 1:10 MeOH/W, (stock concentration is 0.01 mg/ mL) the results imply that all polymers exhibit hydrodynamic radius around 100 nm.

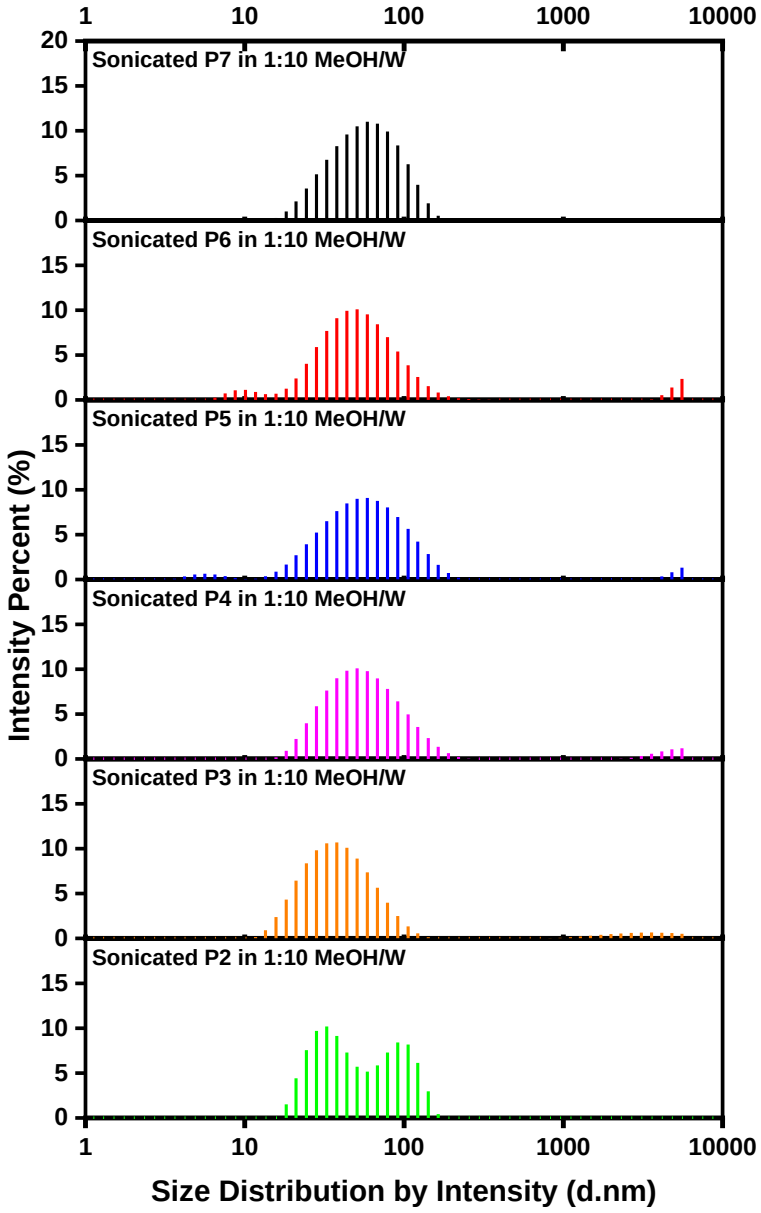

Figure 3.37. Dynamic Light Scattering Sonicated Intensity/Size spectrums of the P2-P7 in 1:10 MeOH/W

In Figure 3.38. Spectrums show intensity autocorrelation versus time graph of Sonicated P2-P7 in 1:10 MeOH/W, (stock concentration is 0.01 mg/ mL) All polymers exhibit the same type of decay time distribution except P2.

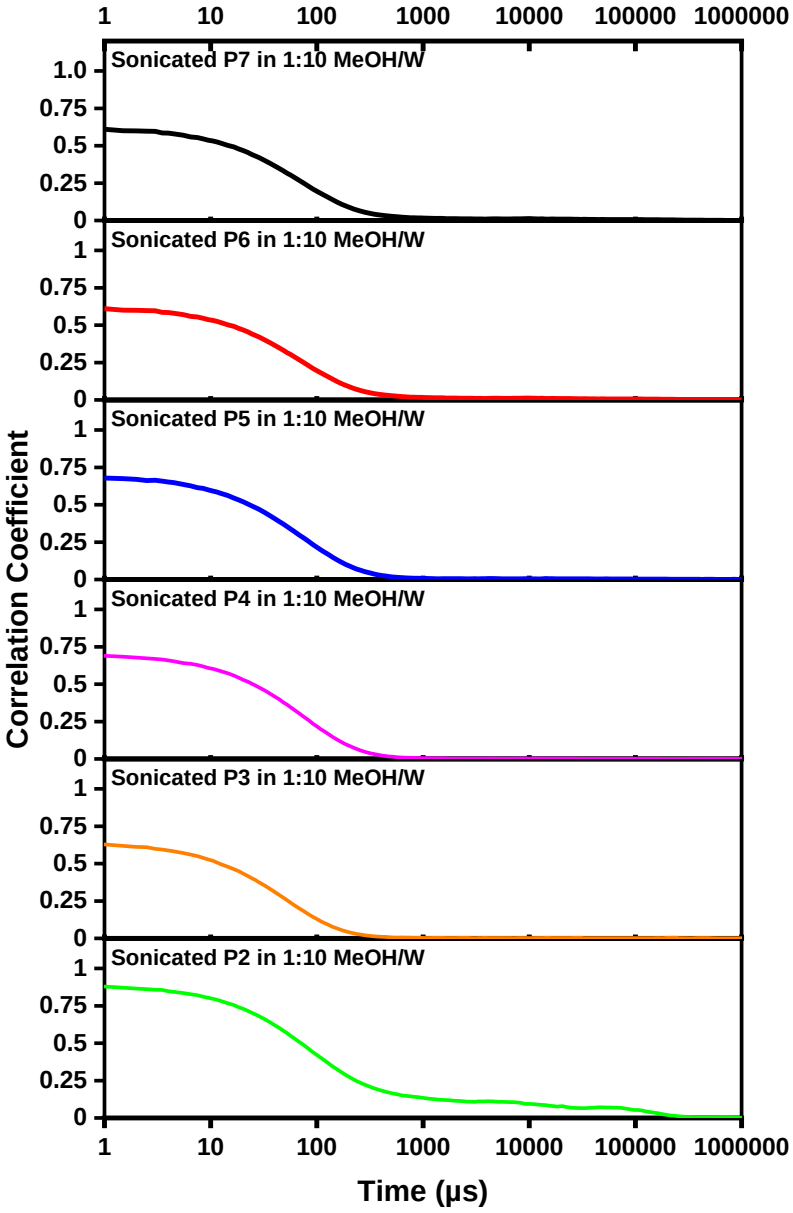

Figure 3.38. Dynamic Light Scattering Sonicated Correlation/Time spectrums of the P2-P7 in 1:10 MeOH/W

In Figure 3.39. Dynamic Light Scattering Intensity/Size spectrums show size distribution analysis of sonicated P2-P7 in 1:30 MeOH/W, (stock concentration is 0.003 mg/ mL) All polymers contain narrow (50-100nm) and, all polymers P6 contain small-sized particles (~10-50 nm). P2, contains broad and large-sized particles (~100 nm).

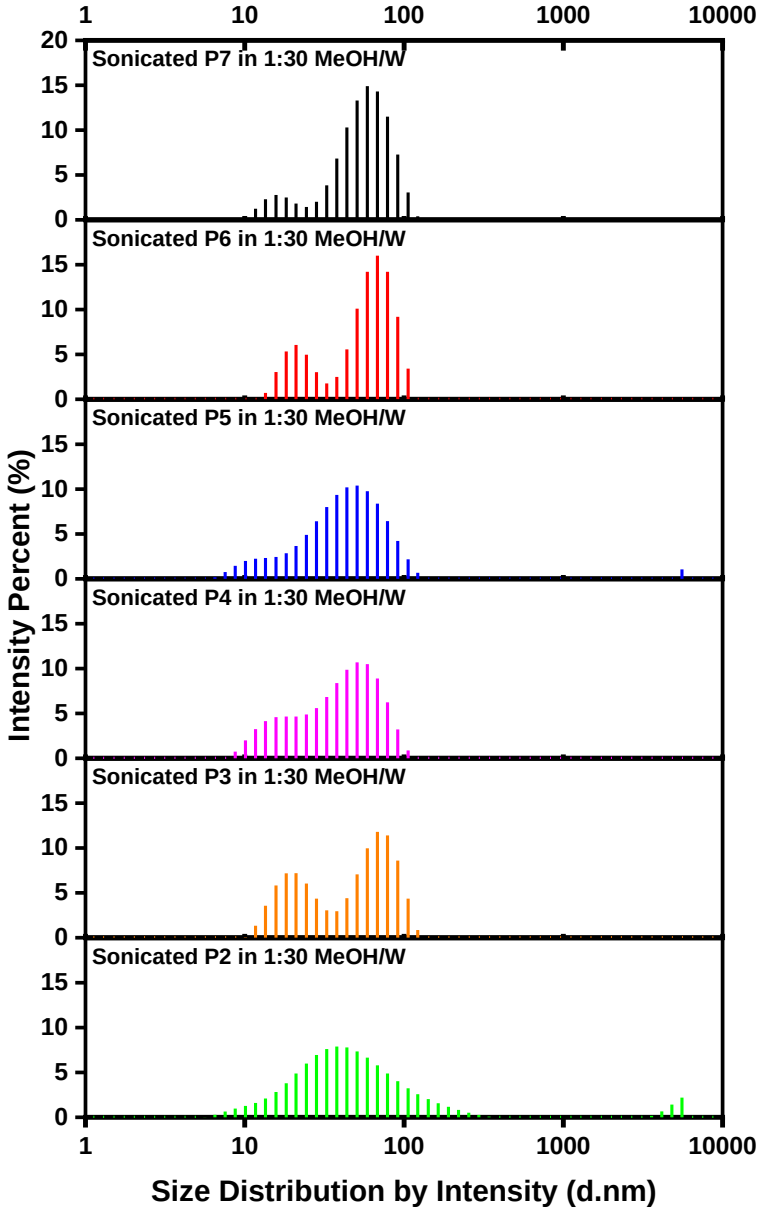

Figure 3.39. Dynamic Light Scattering Sonicated Intensity/Size spectrums of the P2-P7 in 1:30 MeOH/W

In Figure 3.40. Spectrums show intensity autocorrelation versus time graph of Sonicated P2-P7 in 1:30 MeOH/W, P4- P7 polymers exhibit a similar type of decay time distribution (approximately 100.000µs). P2 and P3 polymers exhibit a similar type of decay time distribution (approximately 400 µs).

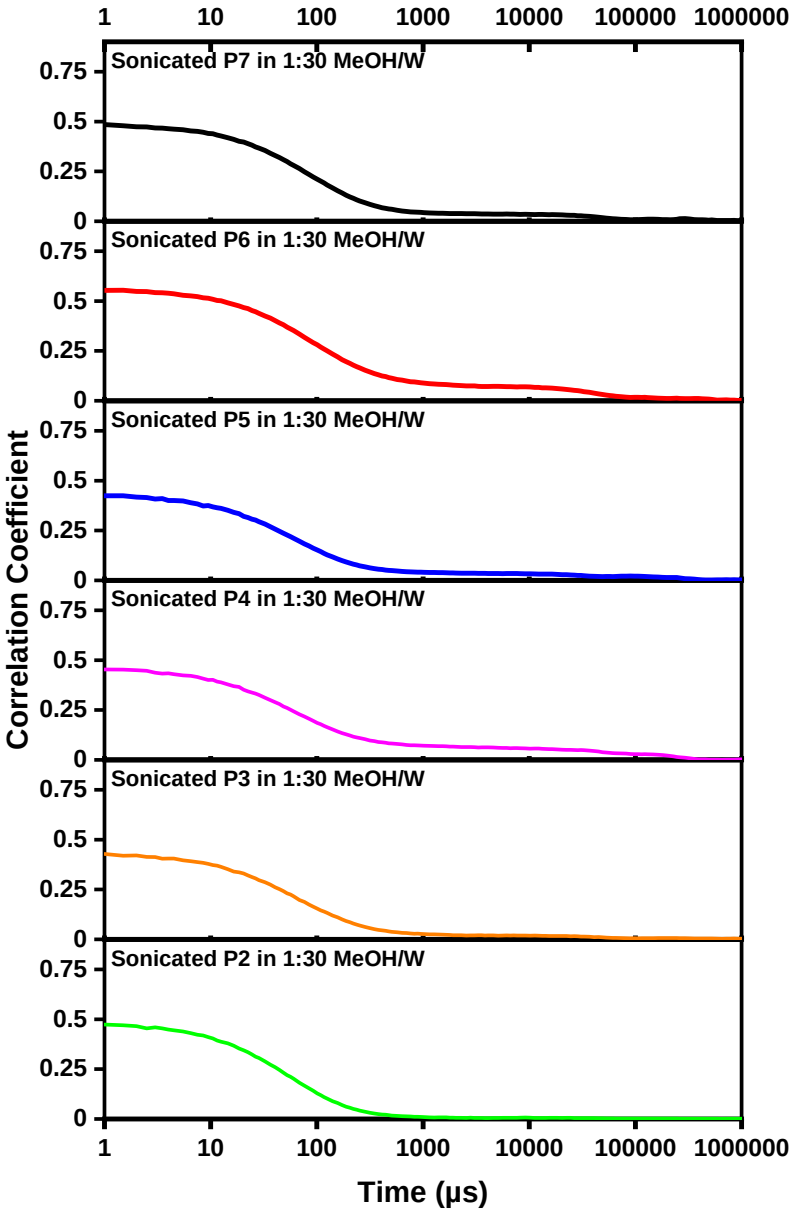

Figure 3.40. Dynamic Light Scattering Sonicated Correlation/Time spectrums of the P2-P7 in 1:30 MeOH/W

Table 3.2. Peak intensity values of size measurements of P2-P7 polymers analyzed in MeOH, 1:10 MeOH/W, 1:30 MeOH/W and after sonication at 1:10 and 1:30 ratios.

Polymers in MeOH MeOH/W	Intensity (%)	Intensity (%) in 1:10	Intensity (%) in 1:30	Sonicated Intensity (%) in 1:10	Sonicated Intensity (%) in 1:30
P2	150nm.	61nm.	53nm	30-94nm.	40nm.
P3	195nm.	25-174nm	20-79nm.	36nm.	18-68nm.
P4	108nm.	15-51-245nm.	20-62nm.	51nm.	13-50nm.
P5	150nm.	20-70nm.	23-86nm.	4-56nm.	9-50nm.
P6	127nm.	18-60nm.	8-54nm.	8-52nm.	22-70nm.
P7	110nm.	53nm.	39-204nm.	53nm.	16-58nm.

In Figure 3.41. Dynamic Light Scattering Intensity/Size spectrums show size distribution analysis of P2-P7 in Ethylene Glycol, (stock concentration is 0.1 mg/ mL) the results imply that all polymers exhibit hydrodynamic radius around 100 nm.

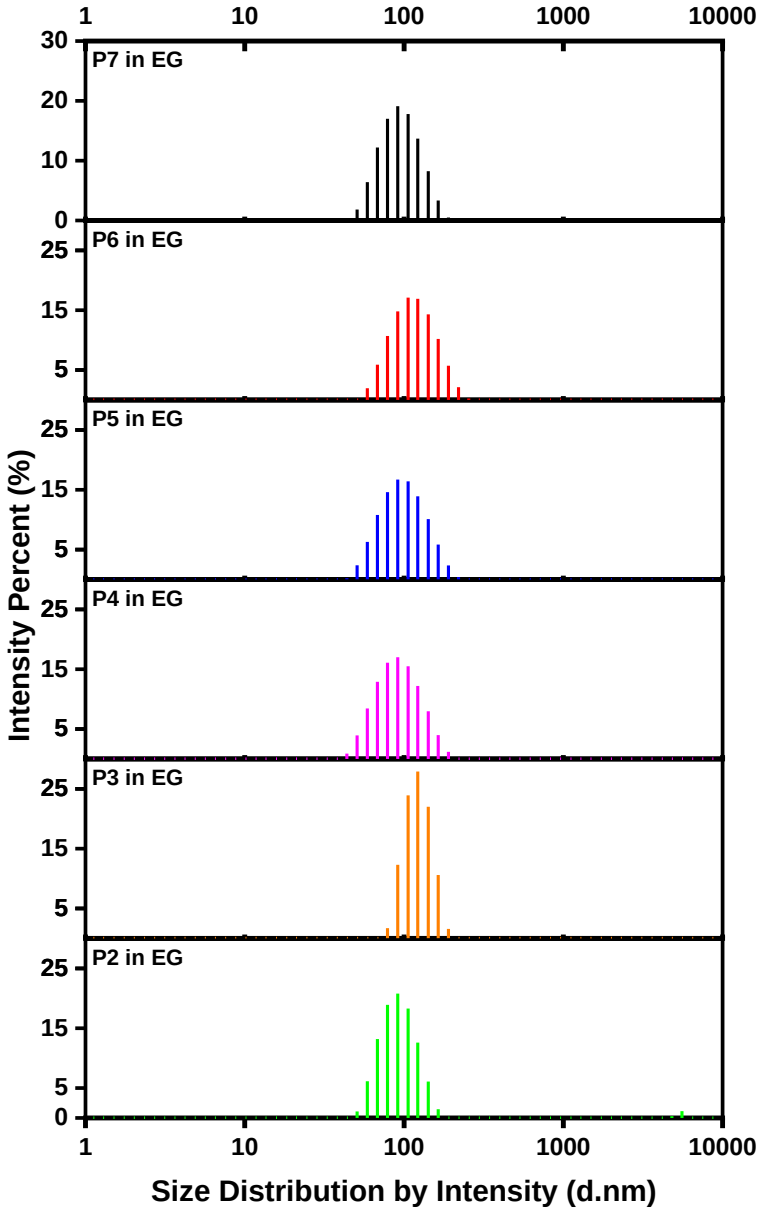

Figure 3.41. Dynamic Light Scattering Intensity/Size spectrums of the P2-P7 in EG

In Figure 3.42 Spectrums show intensity autocorrelation versus time graph of P2-P7 in EG, All polymers exhibit a similar type of decay time distribution (approximately 10.000µs).

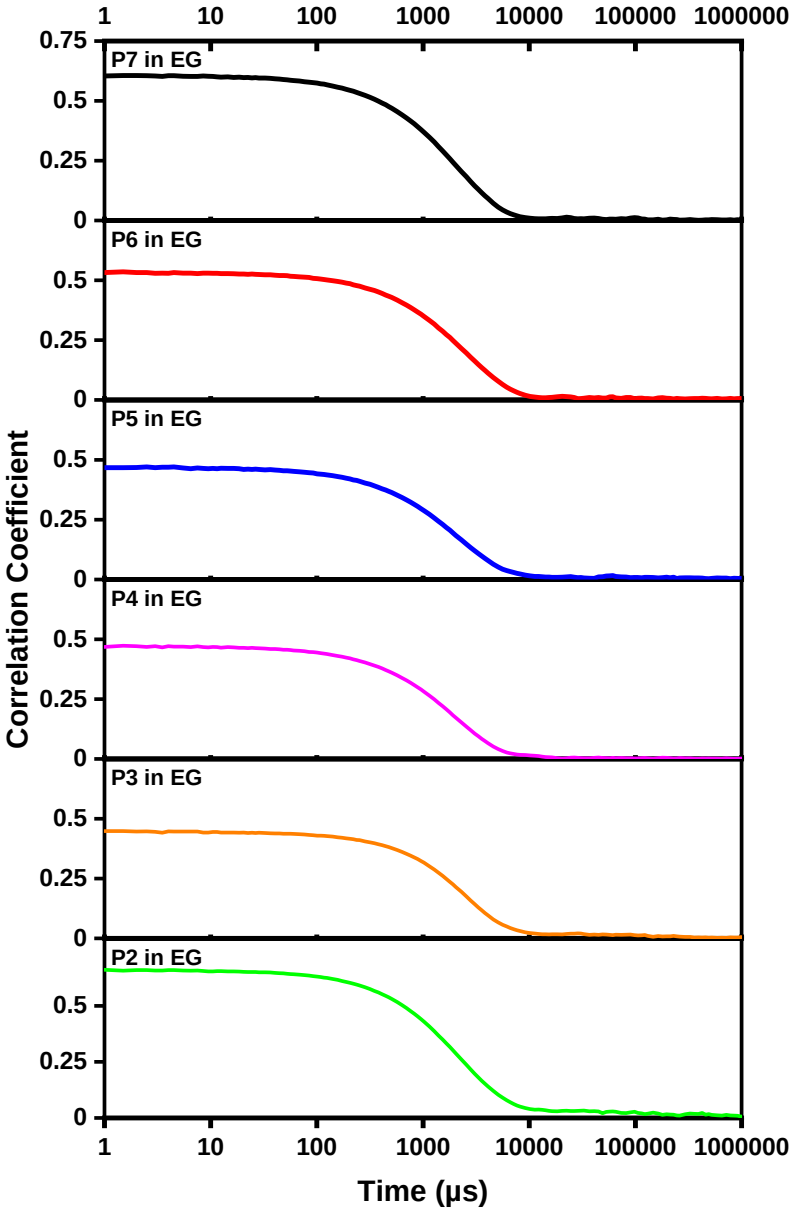

Figure 3.42. Dynamic Light Scattering Correlation/Time spectrums of the P2-P7 in EG

In Figure 3.43 Dynamic Light Scattering Intensity/Size spectrums show size distribution analysis of P2-P7 in 1:10 EG/W, (stock concentration is 0.01 mg/ mL), all polymer solutions contain broad range, and size range of the particles (~10 to~1000 nm).

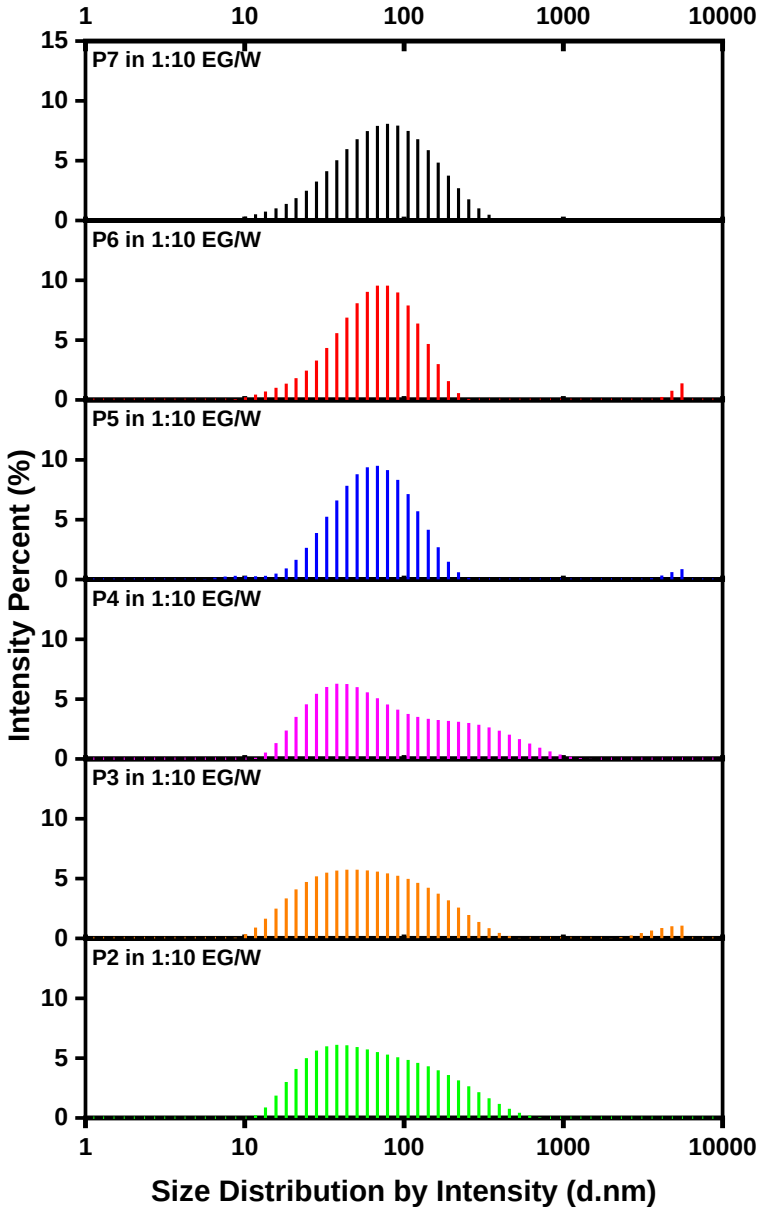

Figure 3.43. Dynamic Light Scattering Intensity/Size spectrums of the P2-P7 diluted 1:10 ratio in EG/W

In Figure 3.44. spectrums show intensity autocorrelation versus time graph of P2-P7 in 1:10 EG/W, (stock concentration is 0.01 mg/ mL) All polymers exhibit the same type of decay time distribution. (approximately 1.000µs).

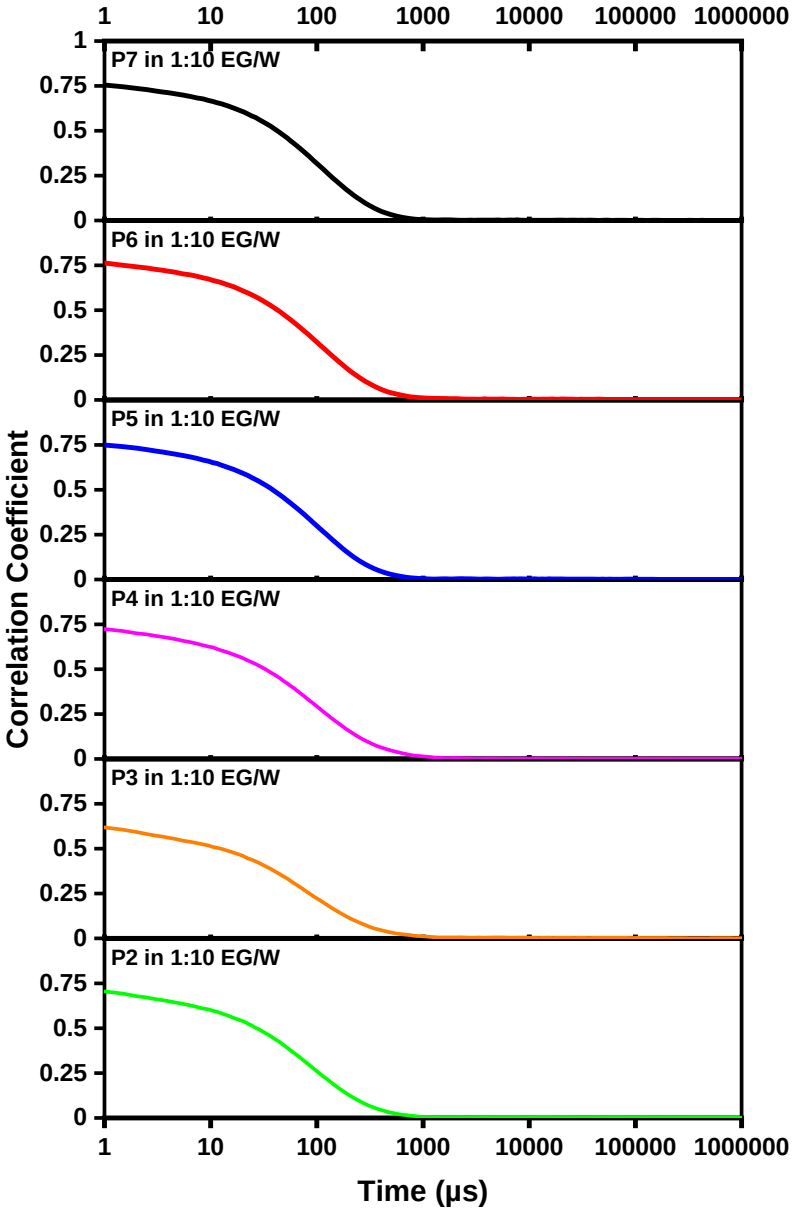

Figure 3.44. Dynamic Light Scattering Correlation/Time spectrums of the P2-P7 in 1:10 EG/W

In Figure 3.45. Intensity/Size spectrums show size distribution analysis of P2-P7 in 1:30 EG/W. P5, P6 and P7 contain small-sized particles (~10-30 nm), and distinct populations with double peaks, and P3 contains broad and large-sized particles (~200 nm).

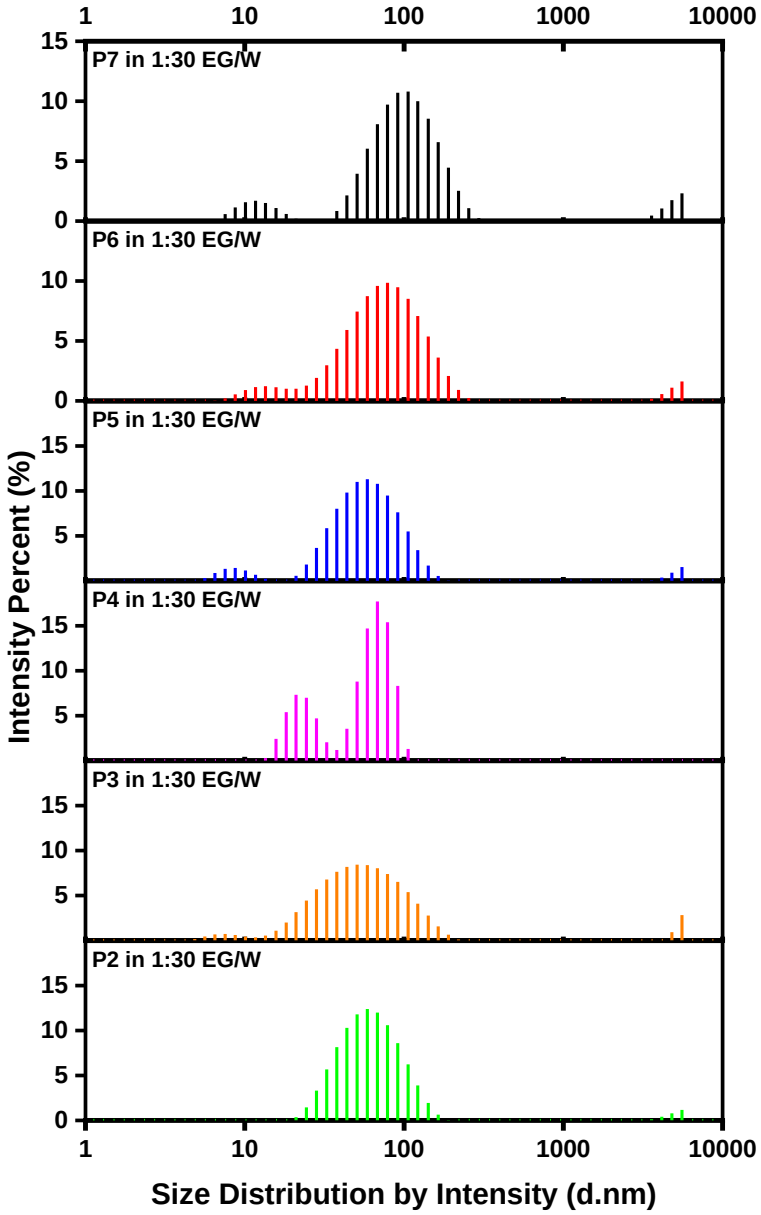

Figure 3.45. Dynamic Light Scattering Intensity/Size spectrums of the P2-P7 diluted 1:30 ratio in EG/W

In Figure 3.46. spectrums show intensity autocorrelation versus time graph of P2-P7 in 1:30 EG/W, (stock concentration is 0.003 mg/ mL) All polymers exhibit the same type of decay time distribution (approximately 1.000µs) except P4 polymer (approximately 10.000µs).

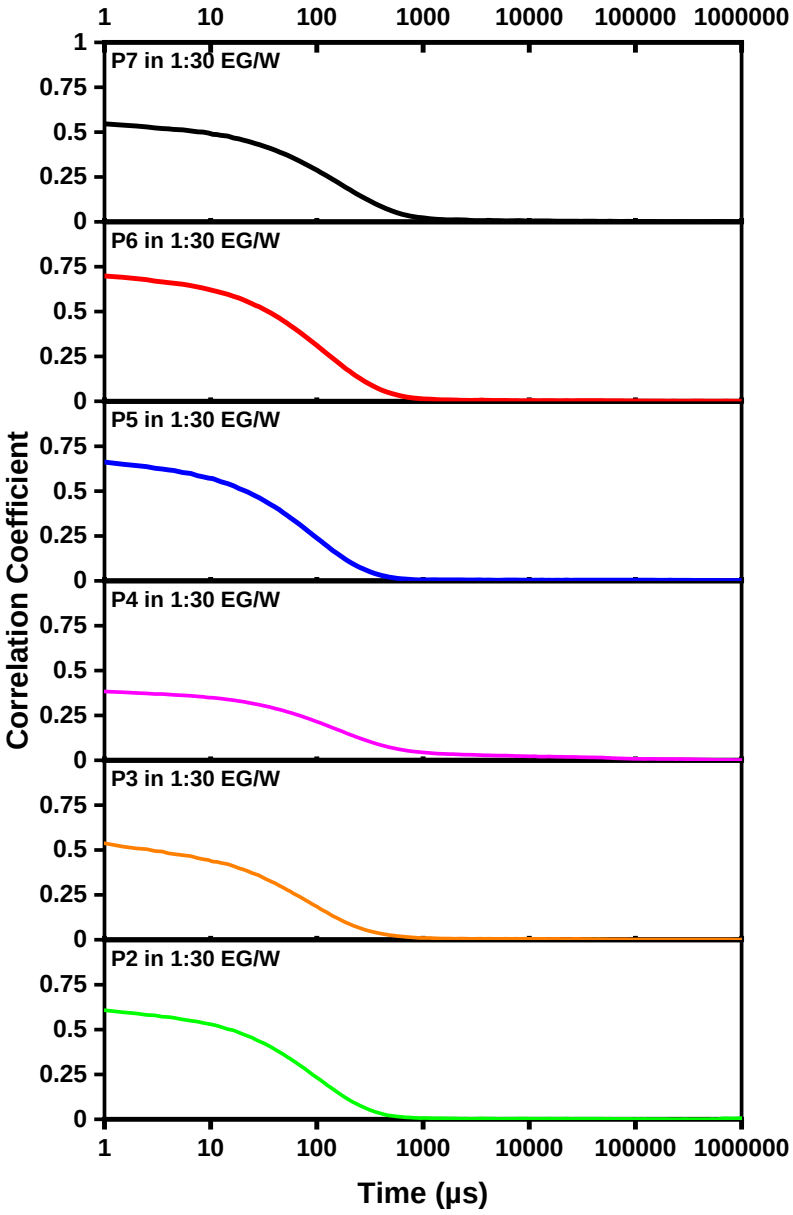

Figure 3.46. Dynamic Light Scattering Correlation/Time spectrums of the P2-P7 in 1:30 EG/W

In Figure 3.47, Intensity/Size spectrums show size distribution analysis of Sonicated P2-P7 in 1:10 EG/W. P6 and P5 have a narrow size distribution and contain small particles (~10-30 nm). P4 has the smallest size distribution and has narrow peak distribution, P2 and P3 have broader distributions compared to the others.

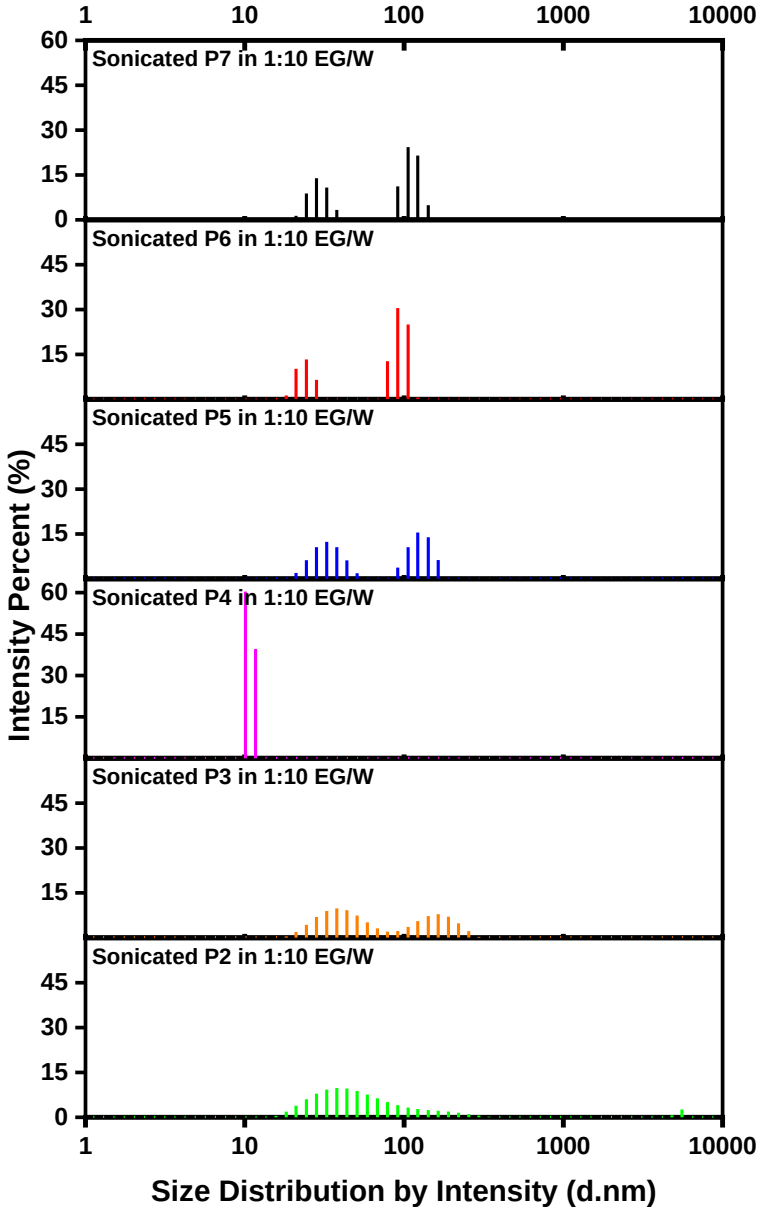

Figure 3.47. Dynamic Light Scattering Sonicated Intensity/Size spectrums of the P2-P7 in 1:10 EG/W

In Figure 3.48. spectrums show intensity autocorrelation versus time graph of Sonicated P2-P7 in 1:30 EG/W. All polymers exhibit multi modal type decay time distributions.

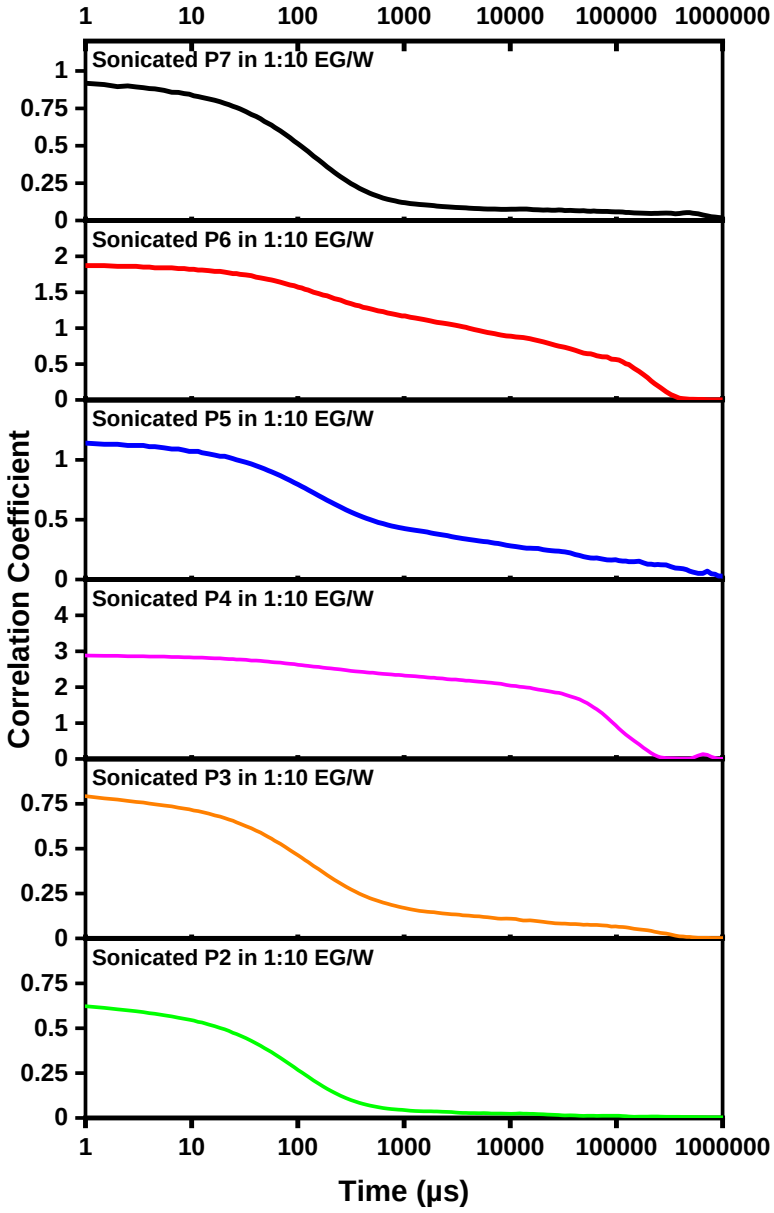

Figure 3.48. Dynamic Light Scattering Sonicated Correlation/Time spectrums of the P2-P7 in 1:10 EG/W

In Figure 3.49 Intensity/Size spectrums show size distribution analysis of Sonicated P2-P7 in 1:30 EG/W. P4, P5, and P7 contain small-sized particles (~10-50 nm), P5 and P7 contain broad and large-sized particles (~500 nm). P3 and P4 have narrow size distributions.

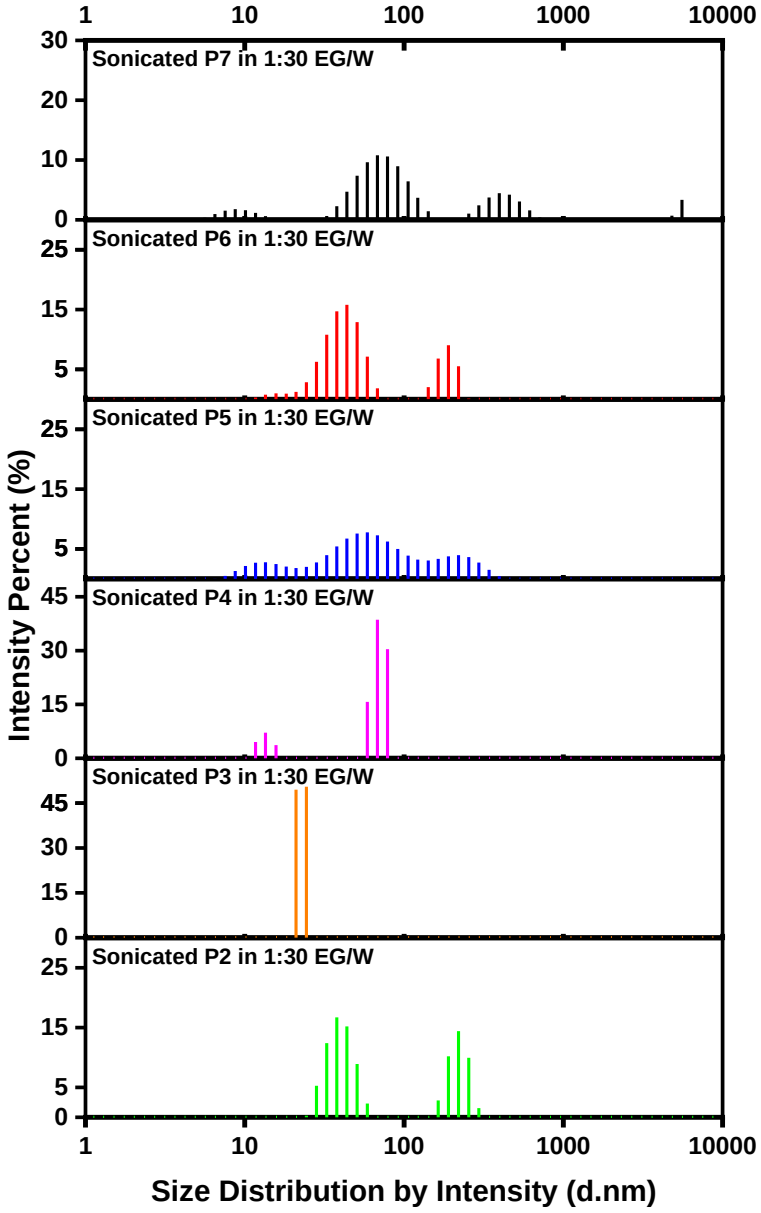

Figure 3.49. Dynamic Light Scattering Sonicated Intensity/Size spectrums of the P2-P7 in 1:30 EG/W

In Figure 3.50. spectrums show intensity autocorrelation versus time graph of Sonicated P2-P7 in 1:30 EG/W. P5, P6 and P7 polymers exhibit the same type of decay time distribution (approximately 50.000µs). P2, P3, and P4 polymers exhibit the same type of decay time distribution (approximately 10.000µs).

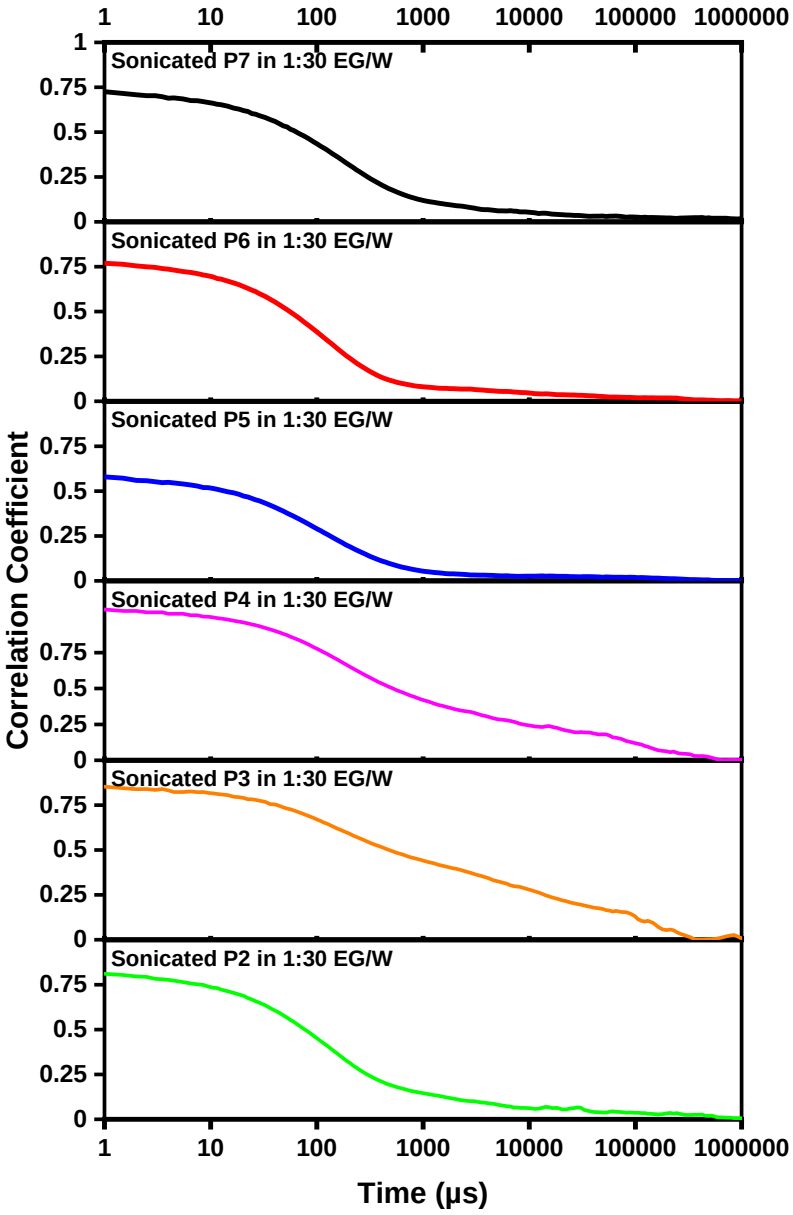

Figure 3.50. Dynamic Light Scattering Sonicated Correlation/Time spectrums of the P2-P7 in 1:30 EG/W

Table 3.3. Peak intensity values of size measurements of P2-P7 polymers analyzed in EG, 1:10 EG/W, 1:30 EG/W and after sonication at 1:10 and 1:30 ratios.

Polymers in EG EG/W	Intensity (%)	Intensity (%) in 1:10	Intensity (%) in 1:30	Sonicated Intensity (%) in 1:10	Sonicated Intensity (%) in 1:30
P2	90nm.	36nm.	57nm	40nm.	38-214nm.
P3	121nm.	42nm	7-50nm.	40-163nm.	23nm.
P4	92nm.	39nm.	21-70nm.	9nm.	13-67nm.
P5	100nm.	62nm.	8-56nm.	31-118nm.	12-57-204nm.
P6	113nm.	75nm.	12-77nm.	23-92nm.	44-200nm.
P7	90nm.	78nm.	10-99nm.	28-106nm.	8-72-414nm.

3.2.5. DLS Analysis of the Diethyl Ether Rinsed Polymers

After washing the polymer solutions with MeOH, prepared at a concentration of 0.5 mg/mL, it was observed that small red particles formed over time. Since the expected fluorescence (FL) values could not be obtained in the analyses, it was suspected that there might be $FeCl_3$ in the polymers. Therefore, the polymers were washed with MeOH to remove $FeCl_3$. However, polymers with cationic structures such as P7 were completely dissolved after a few washes. Therefore, it was decided to wash the polymers with a different solvent. After searching for suitable solvents, it was found that diethyl ether did not dissolve the polymer and successfully removed $FeCl_3$ from the solution. The samples were prepared in Methanol and Ethylene Glycol at a concentration of 0.1 mg/ml for DLS analysis. The prepared samples were analyzed by taking measurements three times. The diameters of the polymers were calculated with the help of Intensity and Correlation spectra and the light scattering fluctuations caused by the Brownian motion of the particles were analyzed with the correlation method. This analysis is done with the correlation function, which is a mathematical function that examines how the scattered light changes over time to measure the size of the particles. Then, the samples were diluted with water at a ratio of 1:10 and 1:30 and it was planned to create Polymer Dots with the Nanophase separation method and the formed Pdot solutions were examined with Intensity and Correlation graphs. The samples prepared with water at a ratio of 1:10 and 1:30 were subjected to sonication for 1 hour and the effect of sonication on Pdot formation was examined.

The correlation graphs of the polymers rinsed with diethyl ether were too high to correctly interpret the particle size. The correlation constant, which is normally expected to be around one, gave results around 4-5 in the analyses. In addition, because of the analyses, particle sizes were observed to cluster in very narrow ranges. No sonication effect was observed in the size analyses performed with EG, and since the accuracy of the results was uncertain, analyses after sonication in MeOH were not performed.
Although the results obtained were different and remarkable, MeOH rinsed polymers were used in the targeted Pdot studies.

In Figure 3.51 Dynamic Light Scattering Intensity/Size spectrums show size distribution analysis of Diethyl Ether rinsed P2-P7 in methanol, P3 and P5 polymers contain small size particles (<10nm). Only P6 polymer have contains larger-size particles. All polymers have narrow size distributions.

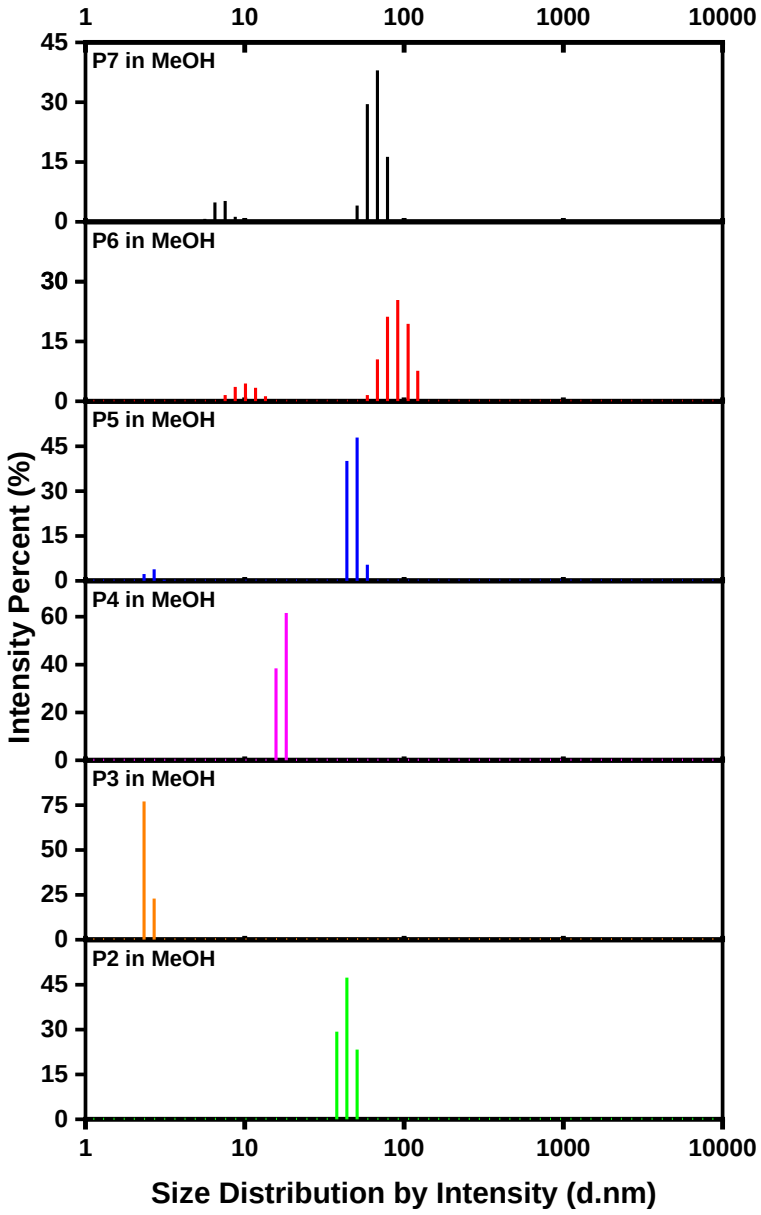

Figure 3.51. Dynamic Light Scattering Intensity/Size Spectrums of the Diethyl Ether Rinsed P2-P7 in MeOH

In Figure 3.52 spectrums show intensity autocorrelation versus time graph of Diethyl Ether rinsed P2-P7 in methanol. All polymers exhibit multi modal type decay time distributions.

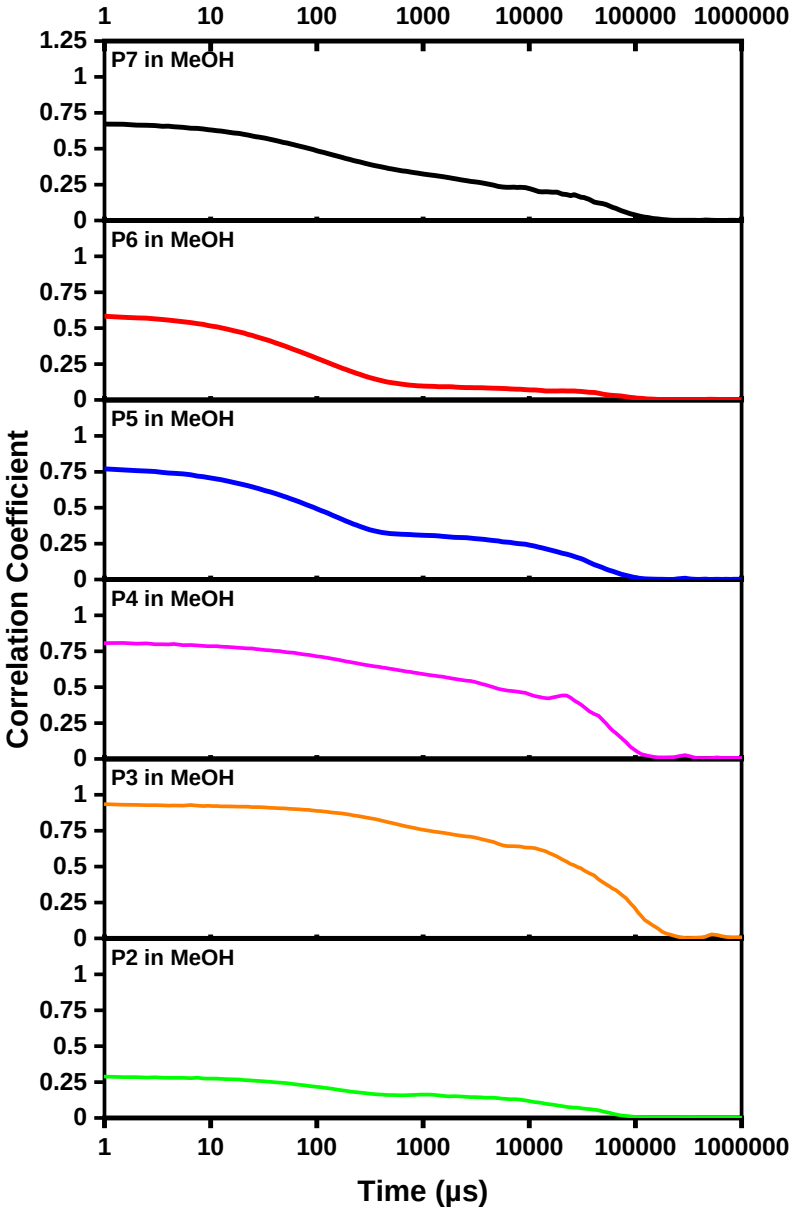

Figure 3.52. Dynamic Light Scattering Intensity/Size Spectrums of the Diethyl Ether Rinsed P2-P7 in MeOH

In Figure 3.53 Intensity/Size spectrums show size distribution analysis of Diethyl Ether rinsed P2-P7 in 1:10 MeOH/W. The results imply that all polymers exhibit hydrodynamic radius around 50-150 nm.

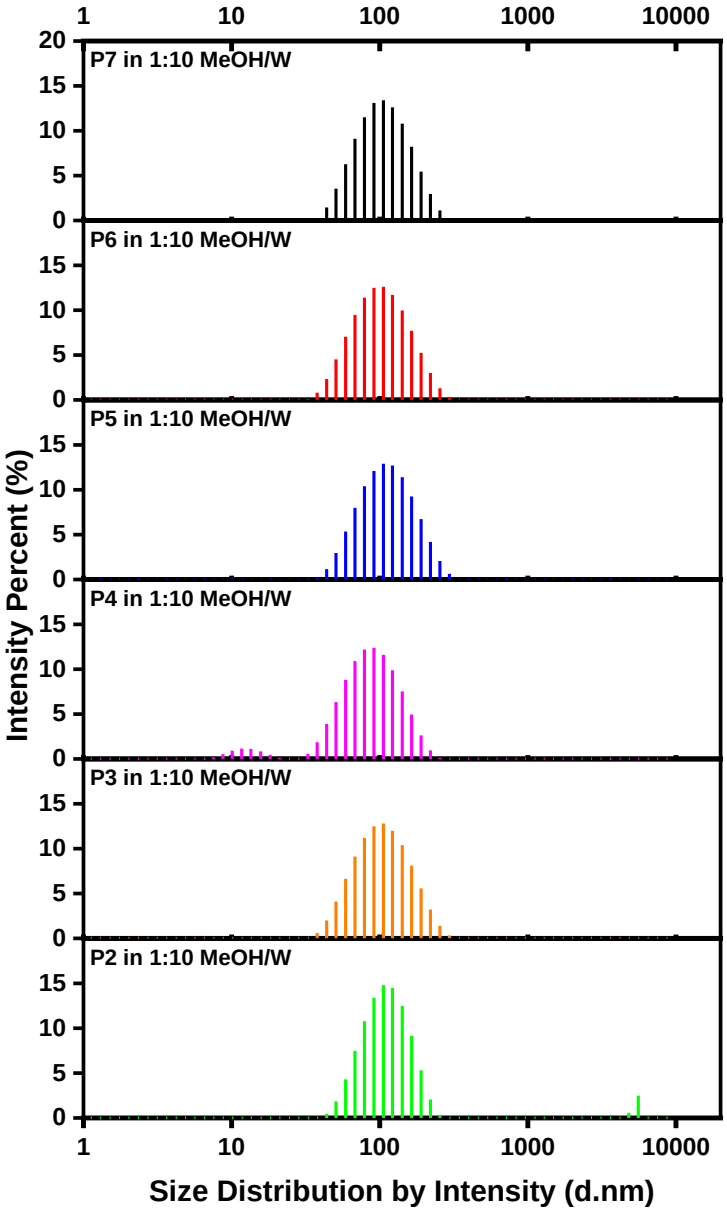

Figure 3.53. Dynamic Light Scattering Intensity/Size spectrums of the Diethyl Ether Rinsed P2-P7 diluted 1:10 ratio in MeOH/W

In Figure 3.54 the spectra display intensity autocorrelation versus time graphs for Diethyl Ether rinsed P2-P7 in a 1:10 MeOH/W solution, with a stock concentration of 0.01 mg/mL. All polymers demonstrate a similar decay time distribution, approximately 1.000 µs.

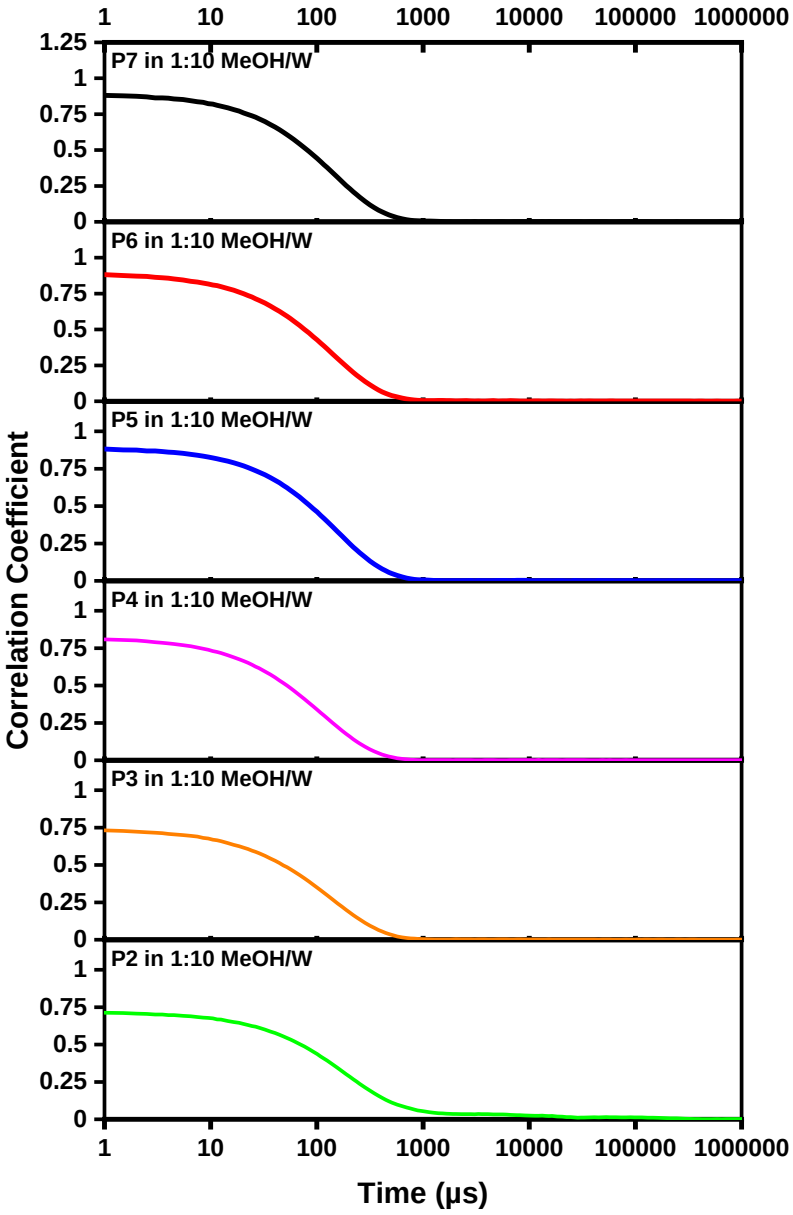

Figure 3.54. Dynamic Light Scattering Correlation/Time spectrums of the Diethyl Ether Rinsed P2-P7 in 1:10 MeOH/W

In Figure 3.55 Intensity/Size spectrums show size distribution analysis of Diethyl Ether rinsed P2-P7 in 1:30 MeOH/W. The results imply that P2 polymer distinct populations with double peaks and all other polymers exhibit hydrodynamic radius around 50-150 nm.

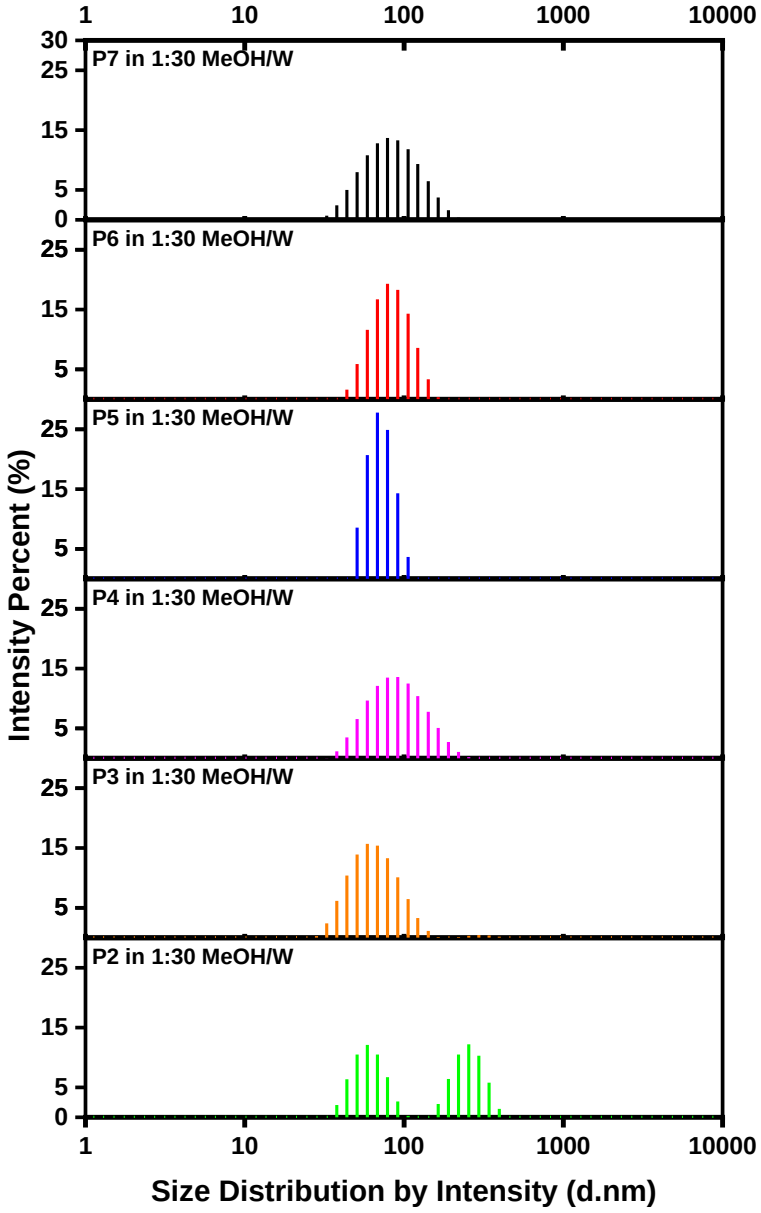

Figure 3.55. Dynamic Light Scattering Intensity/Size spectrums of the Diethyl Ether Rinsed P2-P7 diluted 1:30 ratio in MeOH/W

In Figure 3.56 the spectra display intensity autocorrelation versus time graphs for P2-P7 in a 1:30 EG/W solution, with a stock concentration of 0.003 mg/mL. P4-P7 polymers demonstrate a similar decay time distribution, approximately 1.000 µs. P2 and P3 polymers have a time distribution, approximately 500 µs.

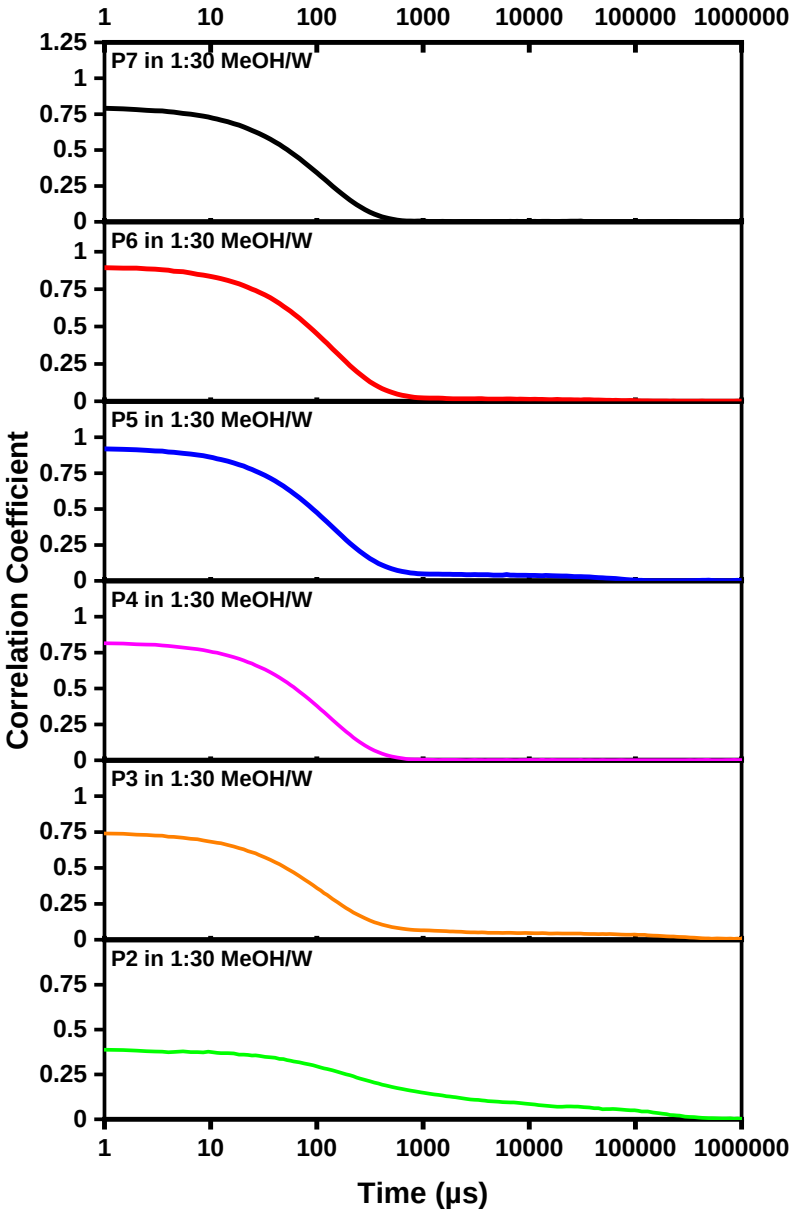

Figure 3.56. Dynamic Light Scattering Correlation/Time spectrums of the Diethyl Ether Rinsed P2-P7 in 1:30 MeOH/W

Table 3.4. Peak intensity values of size measurements of P2-P7 polymers analyzed in MeOH, 1:10 MeOH/W, 1:30 MeOH/W.

Polymers in MeOH MeOH/W	Intensity (%)	Intensity (%) in 1:10	Intensity (%) in 1:30
P2	44nm.	115nm.	61-257nm
P3	3nm.	101nm	61nm.
P4	17nm.	107nm.	86nm.
P5	3-45nm.	12-88nm.	68nm.
P6	10-90nm.	99nm.	77nm.
P7	6-64nm.	104nm.	82nm.

In Figure 3.57 Dynamic Light Scattering Intensity/Size spectrums show size distribution analysis of Diethyl Ether rinsed P2-P7 in Ethylene Glycol, (stock concentration is 0.1 mg/ mL) the results imply that all polymers exhibit hydrodynamic radius around 100 nm. P5 and P7 polymers have broader radius range.

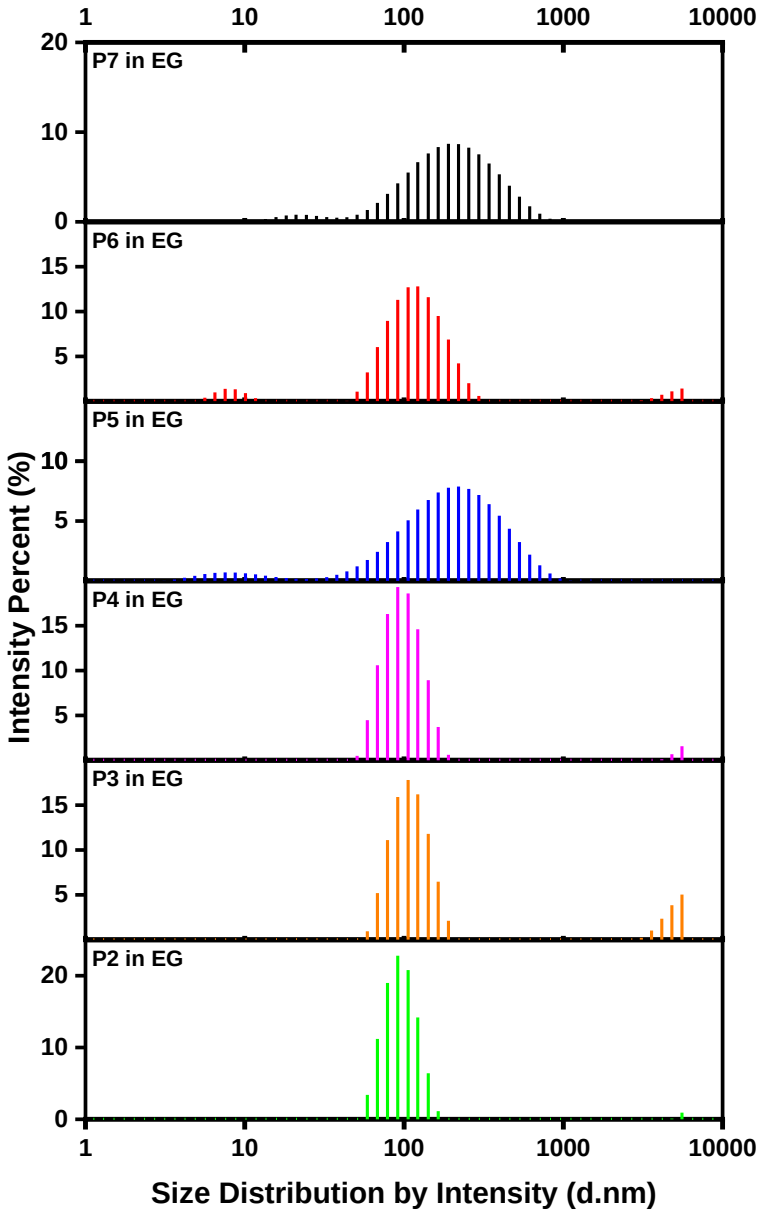

Figure 3.57. Dynamic Light Scattering Correlation/Time spectrums of the Diethyl Ether Rinsed P2-P7 in EG

In Figure 3.58 spectrums show intensity autocorrelation versus time graph of Diethyl Ether rinsed P2-P7 in EG, All polymers exhibit different type of decay time distribution, and all correlation coefficients are low (0,1-0,3 a.u)

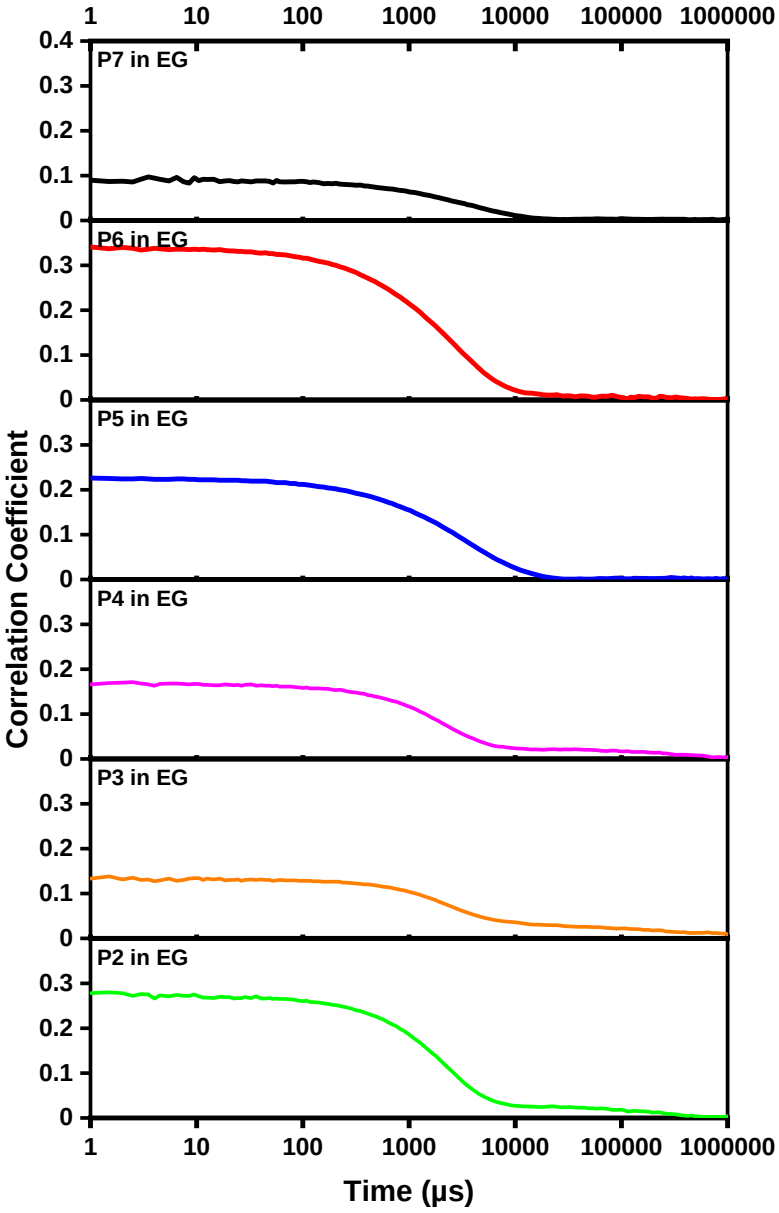

Figure 3.58. Dynamic Light Scattering Correlation/Time Spectrums of the Diethyl Ether Rinsed Spectrums of the P2-P7 in EG

In Figure 3.59 Intensity/Size spectrums show size distribution analysis of Diethyl Ether rinsed P2-P7 in 1:10 EG/W. The results imply that P2 and P3 polymers have distinct populations with double peaks. P4 polymer has a larger radius approximately 500nm. All polymers have broader size distribution.

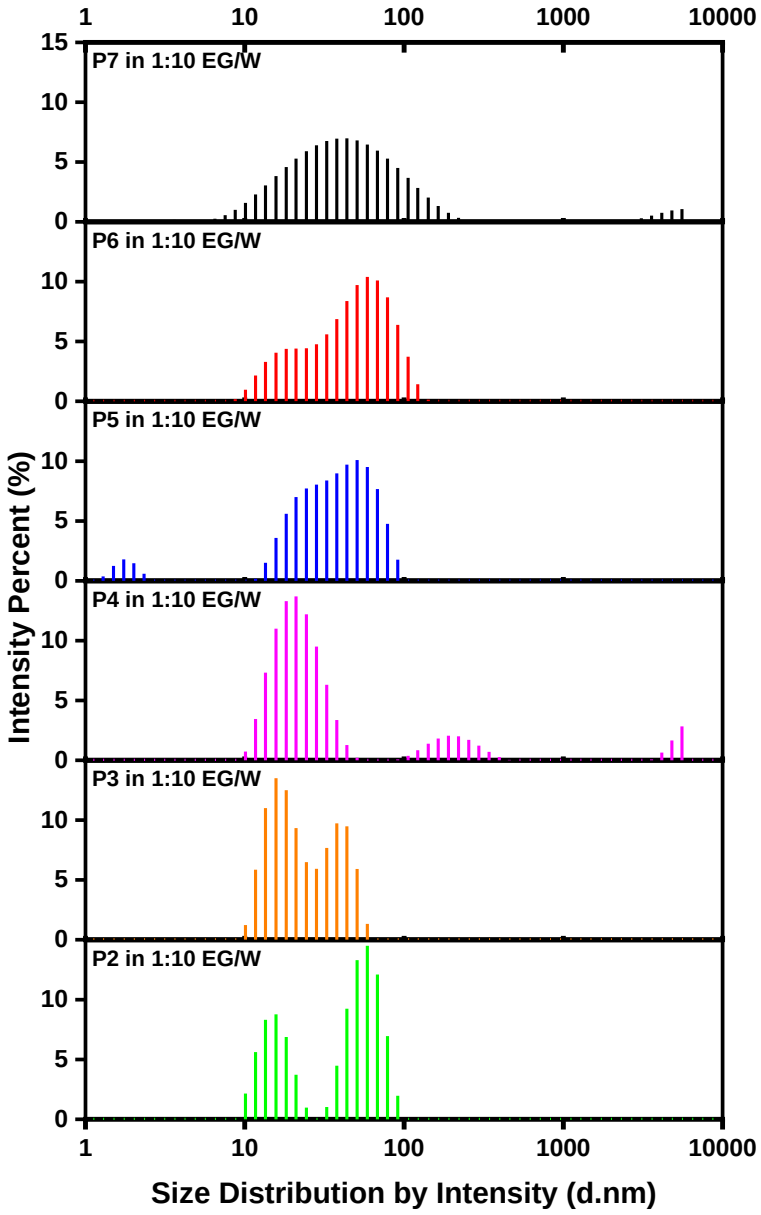

Figure 3.59. Dynamic Light Scattering Intensity-Size Spectrums of the Diethyl Ether Rinsed P2-P7 in 1:10 EG/W

In Figure 3.60. spectrums show intensity autocorrelation versus time graph of Diethyl Ether rinsed P2-P7 in 1:10 EG/W. All polymers exhibit multi modal type decay time distributions. Correlation Coefficients of the polymers are between 0.25-0.75a.u.

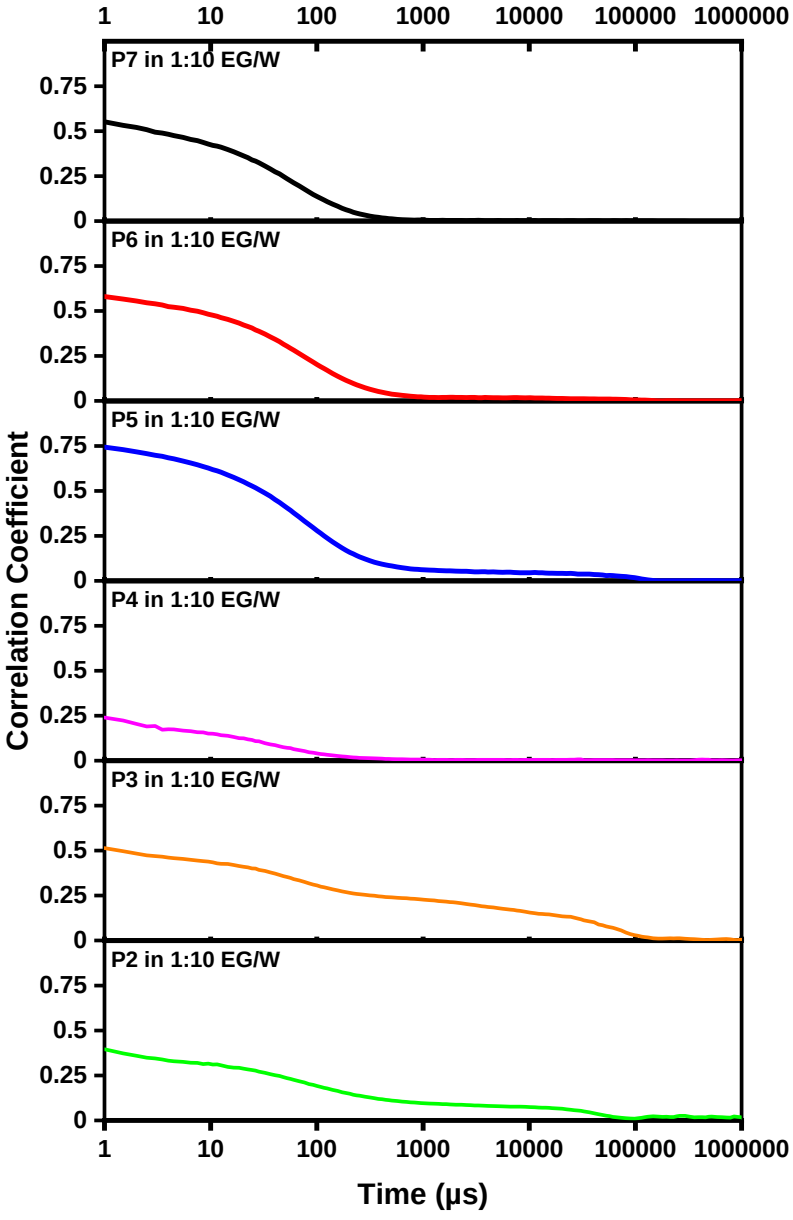

Figure 3.60. Dynamic Light Scattering Correlation/Time Spectrums of the Diethyl Ether Rinsed P2-P7 in 1:10 EG/W

In Figure 3.61. Intensity/Size spectrums show size distribution analysis of Diethyl Ether rinsed P2-P7 in 1:30 EG/W. The results imply that P5, P6 and P7 polymers have distinct populations with double peaks. P2 and P4 polymers have narrow size distributions. P2 has small size polymer particles (Pdots) approximately 1-2nm.

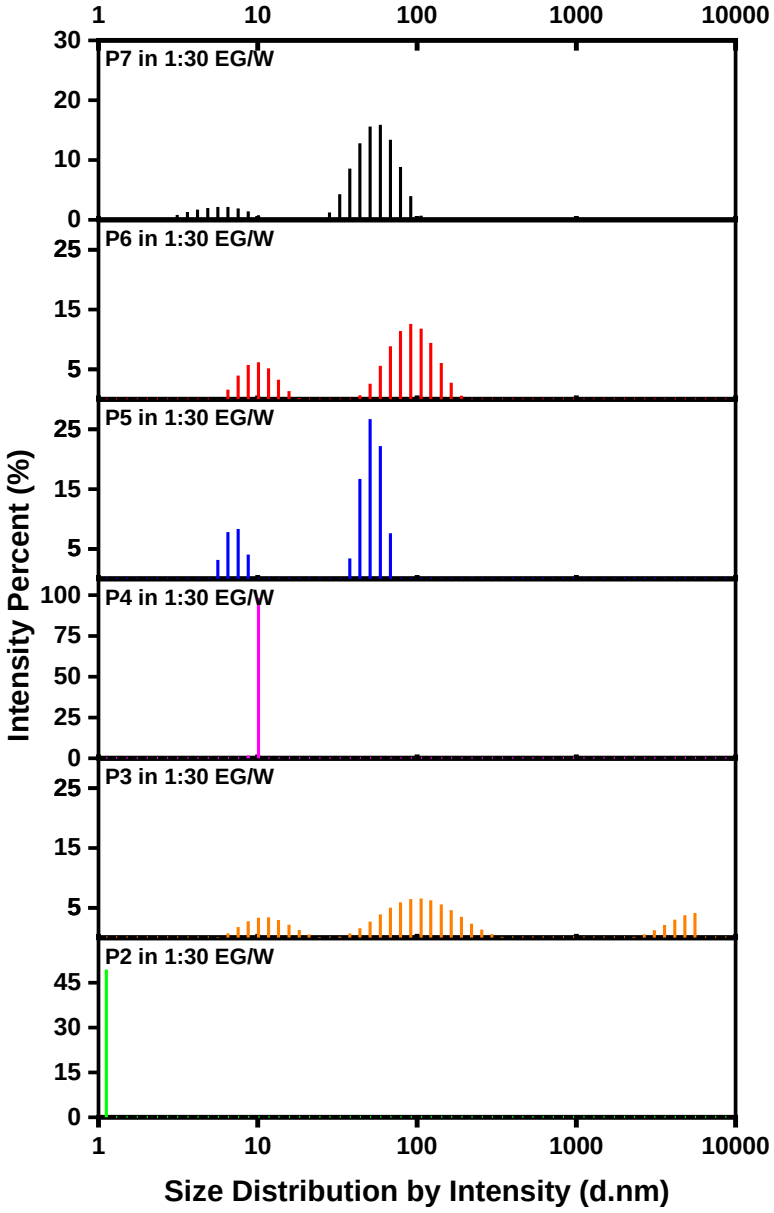

Figure 3.61. Dynamic Light Scattering Intensity-Size Spectrums of the Diethyl Ether Rinsed P2-P7 in 1:30 EG/W

In Figure 3.62. spectrums show intensity autocorrelation versus time graph of Diethyl Ether rinsed P2-P7 in 1:30 EG/W. All polymers exhibit multi modal type decay time distributions. Correlation Coefficients of the polymers are between 0.25-0.75a.u.

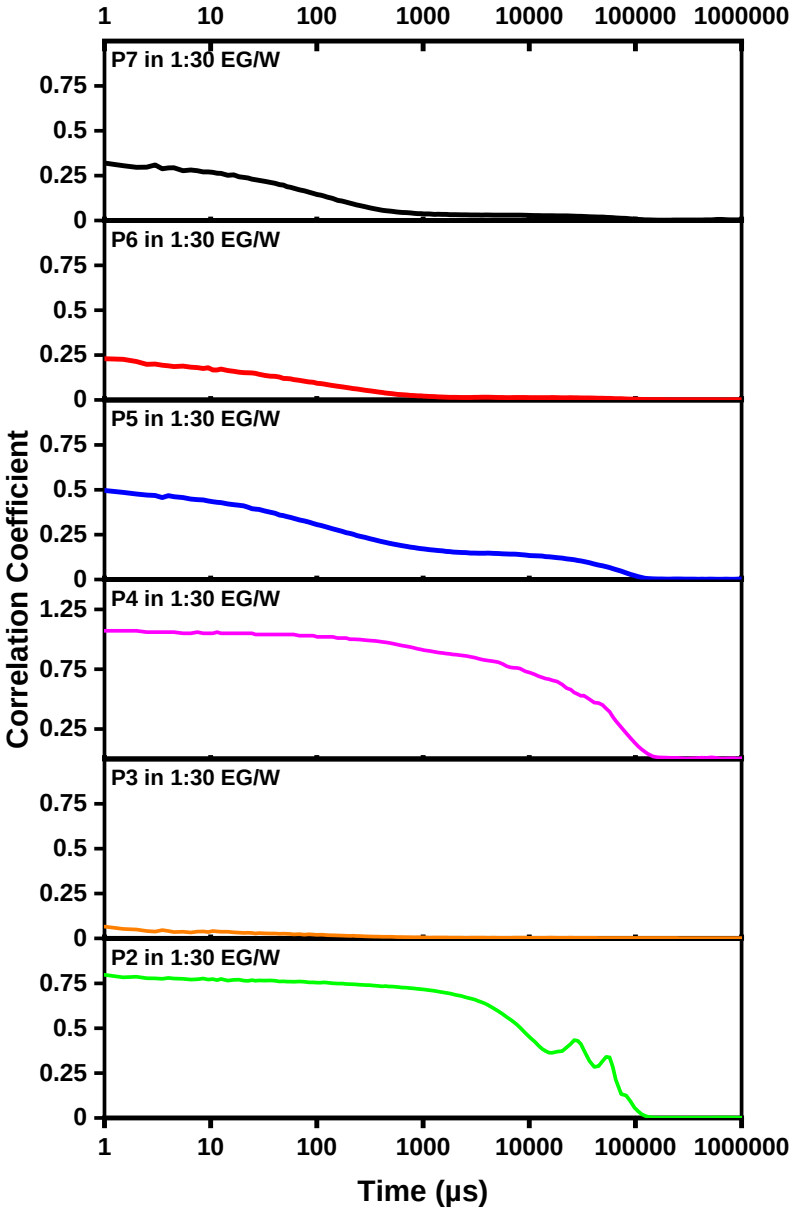

Figure 3.62. Dynamic Light Scattering Correlation/Time Spectrums of the Diethyl Ether Rinsed P2-P7 in 1:30 EG/W

In Figure 3.63. Intensity/Size spectrums show size distribution analysis of Diethyl Ether rinsed Sonicated P2-P7 in 1:10 EG/W. The results imply that P5, P6 and P7 polymers have distinct populations with double peaks. P2 and P4 polymers have narrow size distributions. P2 has small size polymer particles (Pdots) approximately 1-2nm.

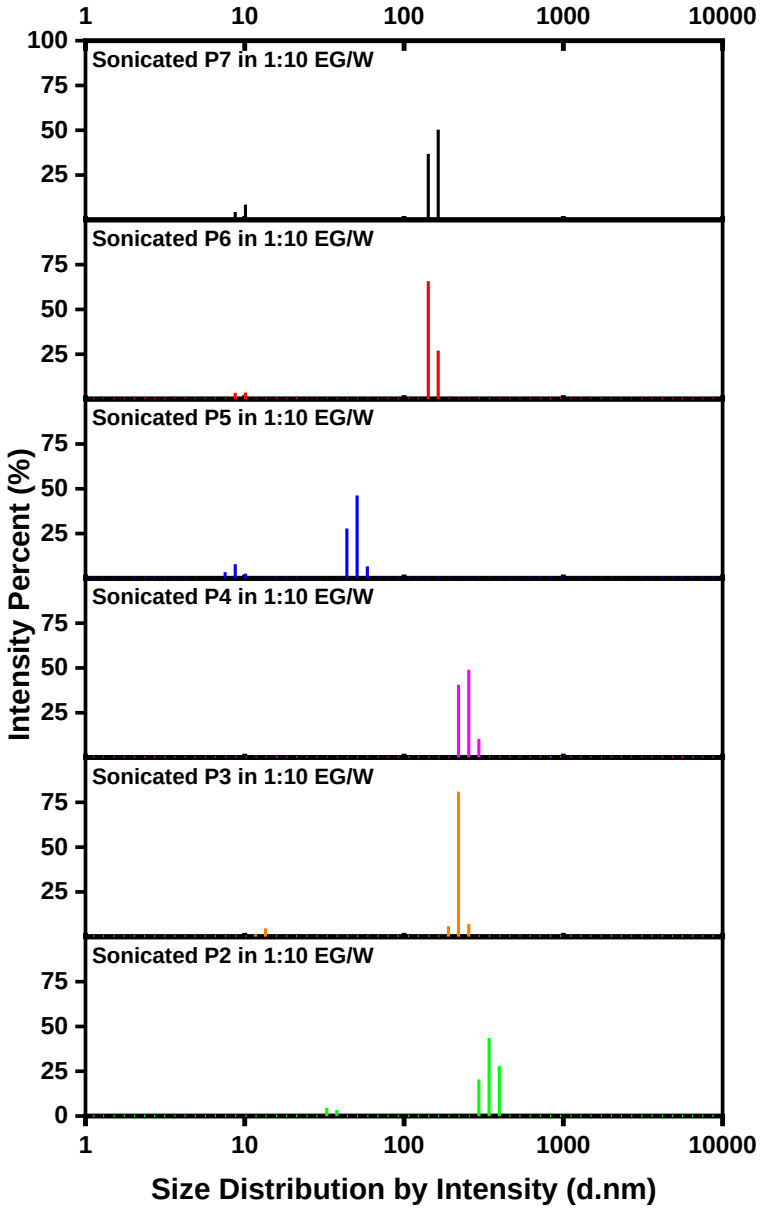

Figure 3.63. Dynamic Light Scattering Sonicated Intensity/Size spectrums of the Diethyl Ether Rinsed P2-P7 in 1:10 EG/W

In Figure 3.64 spectrums show intensity autocorrelation versus time graph of Diethyl Ether Rinsed Sonicated P2-P7 in 1:10 EG/W. All polymers exhibit similar modal type decay time distributions (approximately 1.000.000 μs). Correlation Coefficients of the polymers are between 1-2.5 a.u.

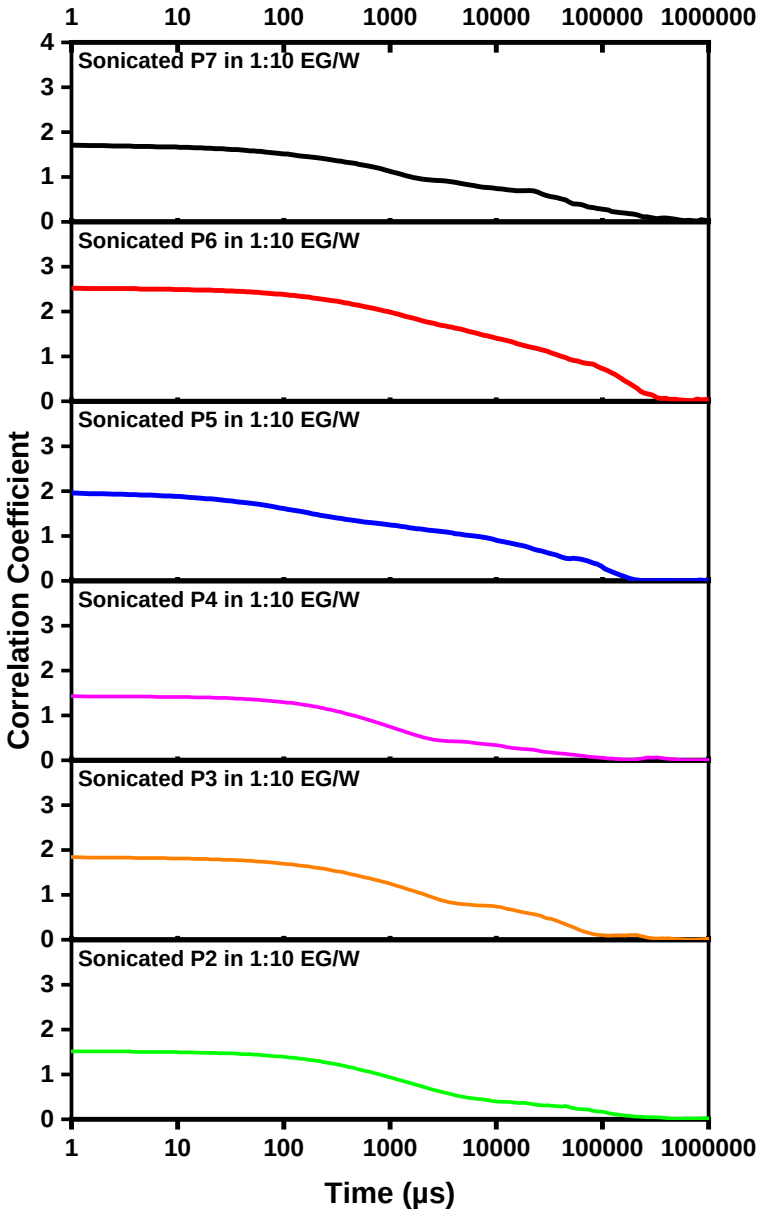

Figure 3.64. Dynamic Light Scattering Sonicated Intensity/Size spectrums of the Diethyl Ether Rinsed P2-P7 in 1:10 EG/W

In Figure 3.65. Intensity/Size spectrums show size distribution analysis of Diethyl Ether rinsed Sonicated P2-P7 in 1:30 EG/W. P5 and P6 polymers have larger size distributions. The results imply that P2, P4 and P7 polymers exhibit hydrodynamic radius around 100 nm. Only P3 polymer solution have smaller size distribution (approximately 20nm)

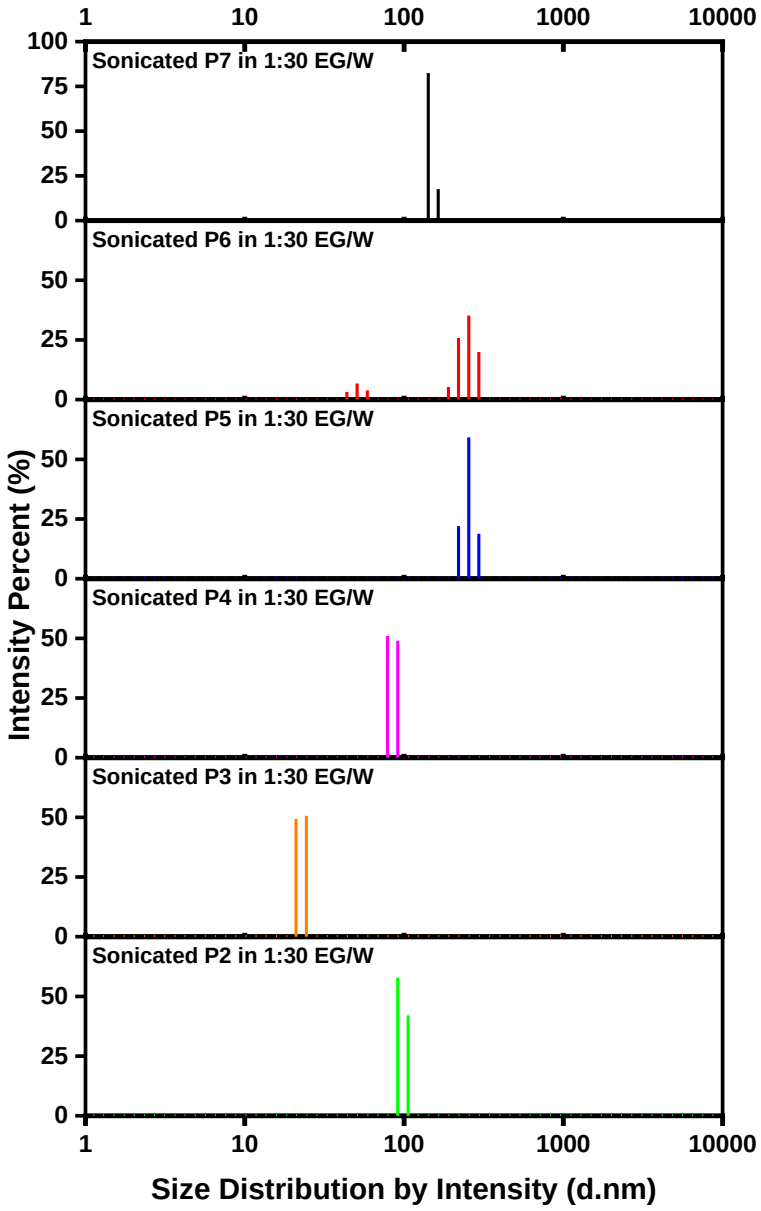

Figure 3.65. Dynamic Light Scattering Sonicated Intensity/Size spectrums of the Diethyl Ether Rinsed P2-P7 in 1:30 EG/W

In Figure 3.66 spectrums show intensity autocorrelation versus time graph of Diethyl Ether Rinsed Sonicated P2-P7 in 1:30 EG/W. All polymers exhibit similar modal type decay time distributions (approximately 100.000 µs). Correlation Coefficients of the polymers are between 1-6 a.u.

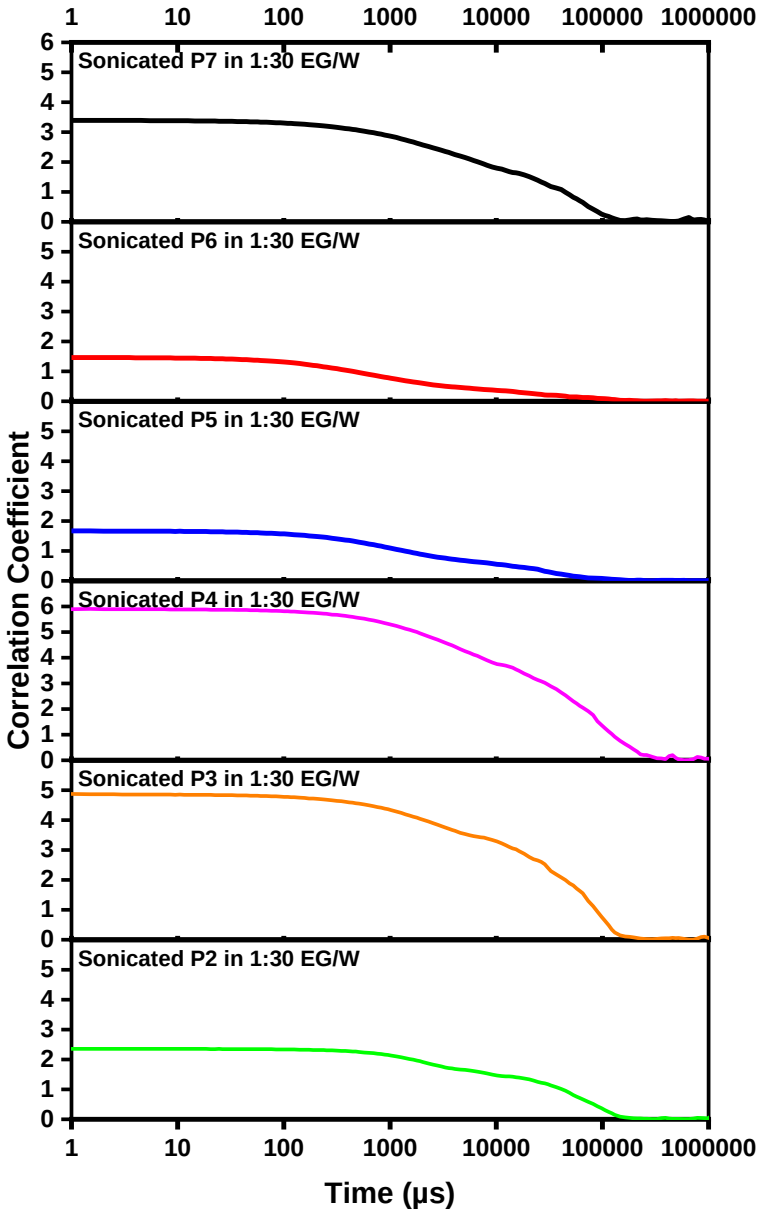

Figure 3.66. Dynamic Light Scattering Sonicated Intensity/Size spectrums of the Diethyl Ether Rinsed P2-P7 in 1:30 EG/W

Table 3.5. Peak intensity values of size measurements of P2-P7 polymers analyzed in EG, 1:10 EG/W, 1:30 EG/W and after sonication at 1:10 and 1:30 ratios.

Polymers in EG EG/W	Intensity (%)	Intensity (%) in 1:10	Intensity (%) in 1:30	Sonicated Intensity (%) in 1:10	Sonicated Intensity (%) in 1:30
P2	94nm.	14-58nm.	1nm	33-337nm.	92nm.
P3	106nm.	15-41nm	10-113nm.	11-220nm.	22nm.
P4	94nm.	21-220nm.	10nm.	245nm.	86nm.
P5	7-241nm.	2-50nm.	6-50nm.	8-50nm.	245nm.
P6	8-116nm.	18-63nm.	9-94nm.	9-142nm.	52-268nm.
P7	23-204nm.	41nm.	5-55nm.	10-156nm.	139nm.

3.2.6. Quantum Yield Analysis of the Polymers

Fluorophores are molecules that can absorb light energy, become excited, and then emit this energy by fluorescence. This property makes them frequently used in biological imaging, molecular labeling, and chemical analysis. (Lakowicz 2006)The performance of a fluorophore is usually measured by quantum yield, which is a ratio of how many of the absorbed photons are emitted as fluorescence photons.(Yu et al. 2017) The higher the quantum yield value, the greater the fluorescence efficiency of the fluorophore. (F. Liu et al. 2017; Anni 2023) Fluorescence quenching is the decrease in the light emitted by fluorophores due to environmental factors or interactions with other molecules. Quantum

yield analyses were conducted by dissolving the polymers in methanol (MeOH), which was used as the reference solvent. A polymer solution with an initial concentration of 0.5 mg/mL in MeOH was prepared, and 50 µL of this solution was subsequently diluted with 2 mL of MeOH for the measurements. The quantum yield was calculated by comparing the spectrum of the polymer solution to the blank spectrum of the solvent. The results revealed that hydrophobic polymers demonstrated significantly higher quantum yield values.

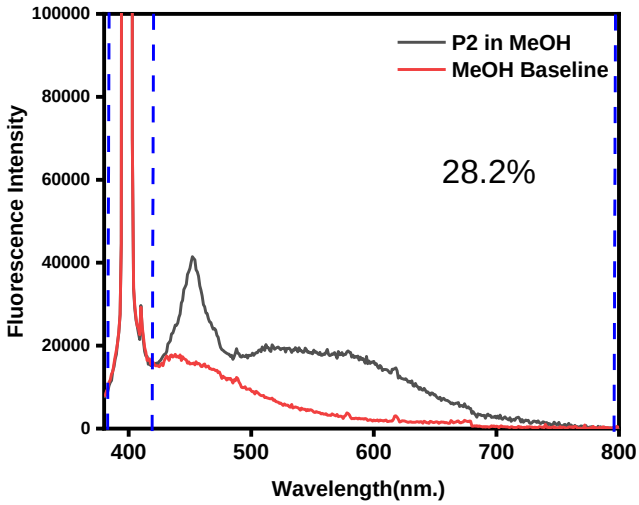

Figure 3.67. Quantum Yield Analysis of P2 Polymer with MeOH baseline.

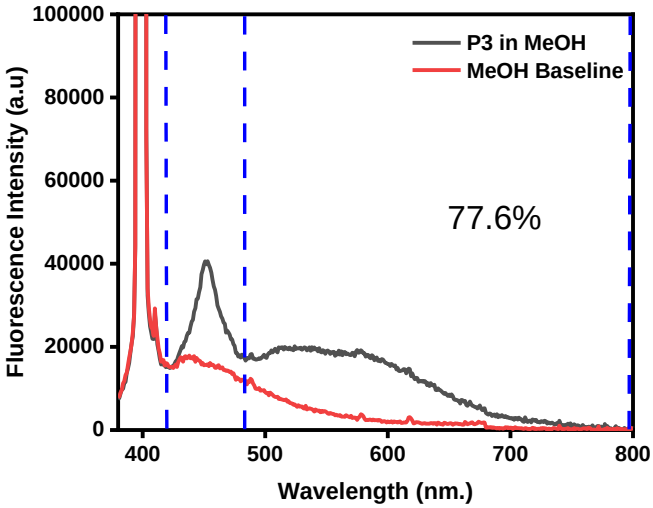

Figure 3.68. Quantum Yield Analysis of P3 Polymer with MeOH baseline.

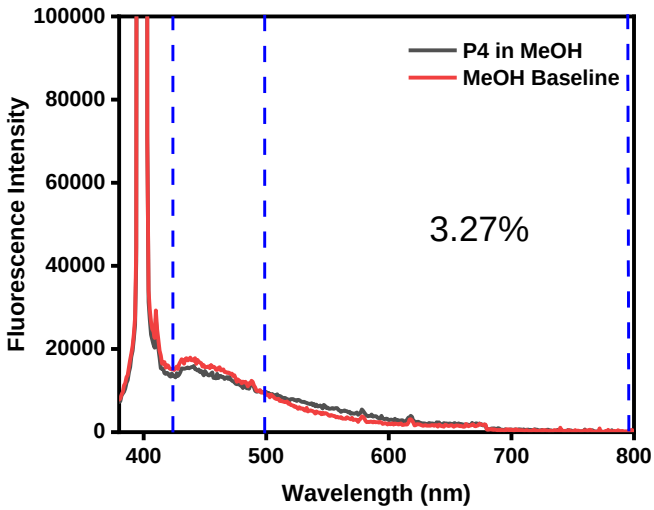

Figure 3.69. Quantum Yield Analysis of P4 Polymer with MeOH baseline.

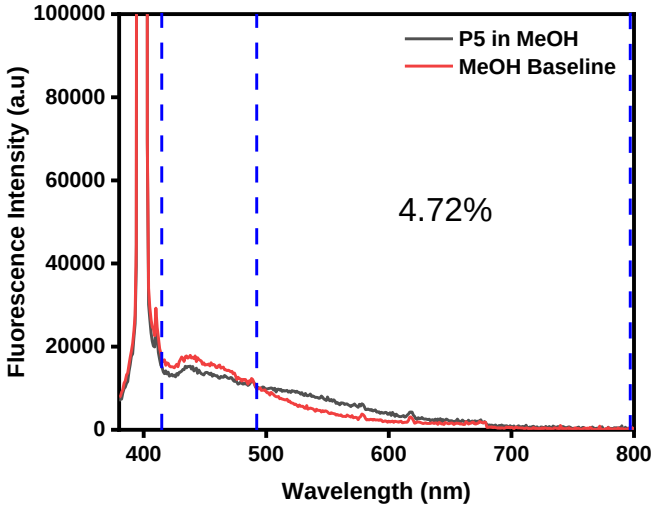

Figure 3.70. Quantum Yield Analysis of P5 Polymer with MeOH baseline.

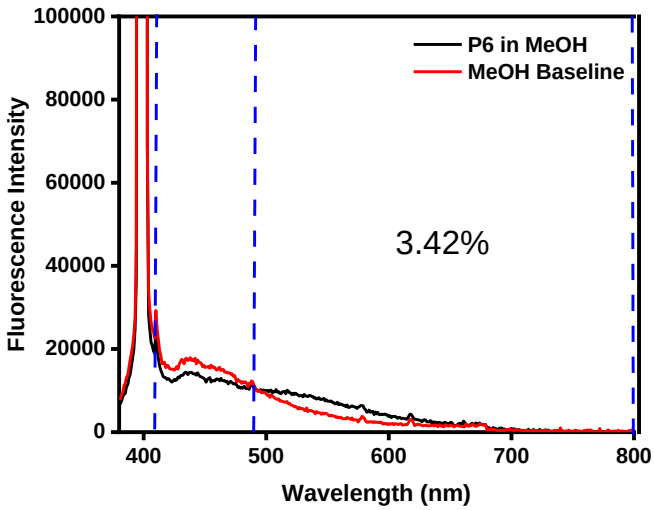

Figure 3.71. Quantum Yield Analysis of P6 Polymer with MeOH baseline.

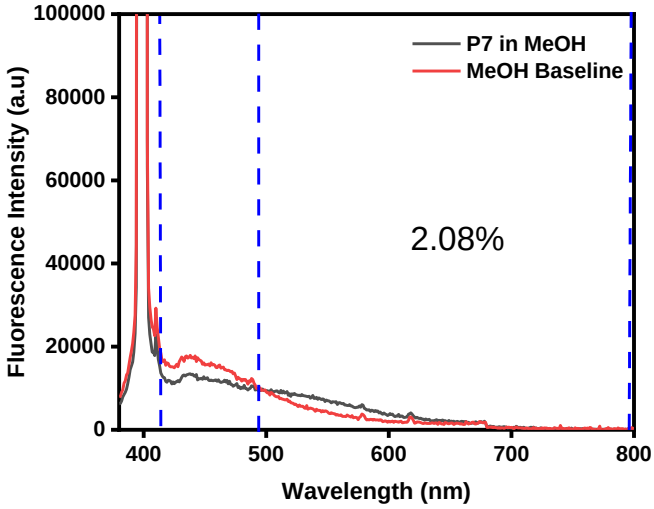

Figure 3.72. Quantum Yield Analysis of P7 Polymer with MeOH baseline.

Table 3.6. Quantum Yield Analysis of P2-P7 polymers

Polymer Name	Polymer Ratio M1:M2	QY of the Polymers
P2	10:1	%28,6
P3	5:1	%77,6
P4	1:1	%3,27
P5	1:5	%4,72
P6	1:10	%3,42
P7	Homopolymer	%2,08

3.2.7. Quantum Yield Analysis of PDots

Quantum yield analyses were performed by dissolving Pdots in EG and diluting them in water. The solvent system used for the preparation of Pdot consists of ethylene glycol (EG) and water (W) in a ratio of 1:30 (v/v). The same ratio of EG and Water was used as a reference. A polymer solution with an initial concentration of 0.5 mg/mL in EG was prepared, and 50 µL of this solution was subsequently diluted with 2 mL of Water for the measurements. Hydrophilic polymer solutions gave higher quantum yield results.

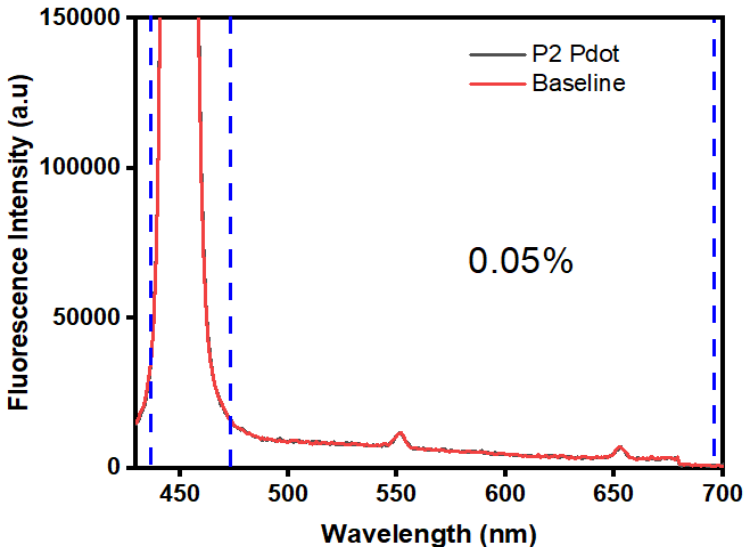

Figure 3.73. Quantum Yield Analysis of P2 Pdot Formation.

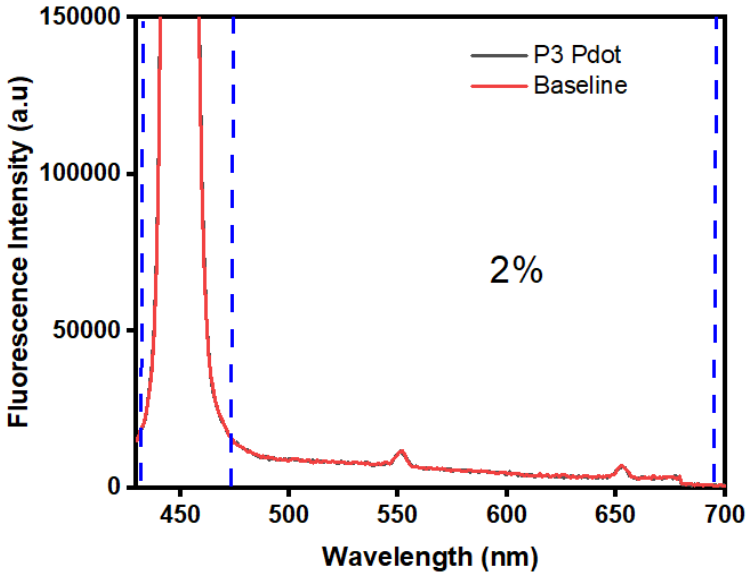

Figure 3.74. Quantum Yield Analysis of P3 Pdot Formation.

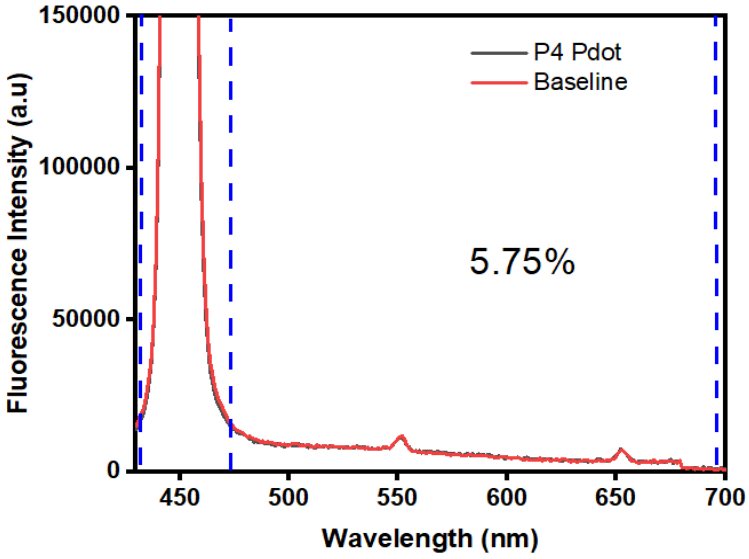

Figure 3.75. Quantum Yield Analysis of P4 Pdot Formation.

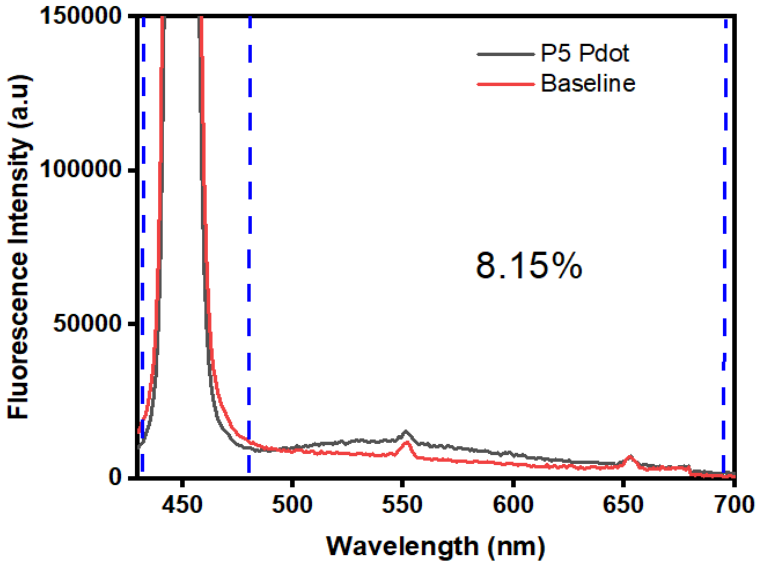

Figure 3.76. Quantum Yield Analysis of P5 Pdot Formation.

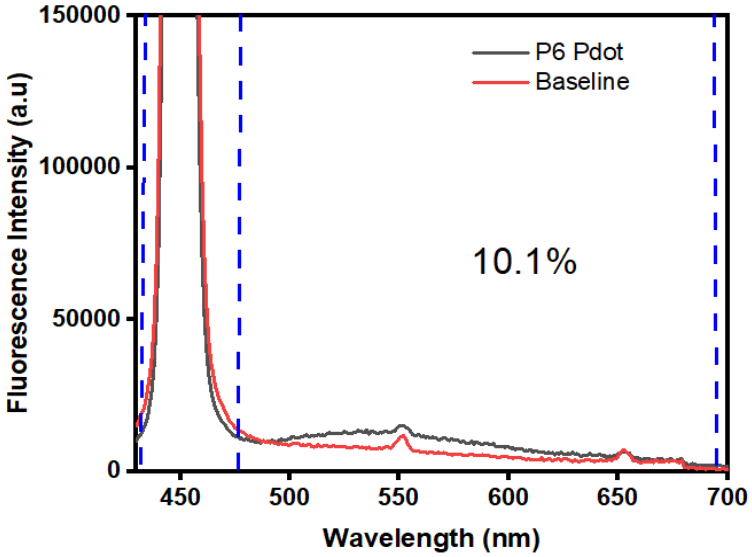

Figure 3.77. Quantum Yield Analysis of P6 Pdot Formation.

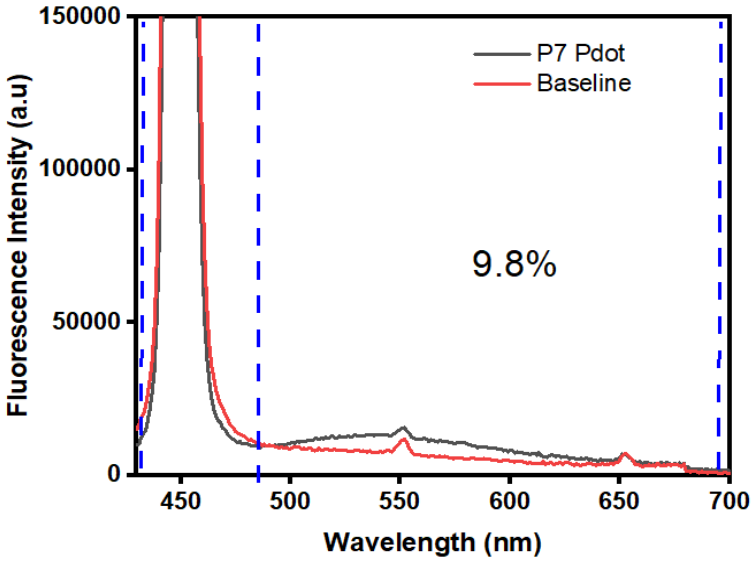

Figure 3.78. Quantum Yield Analysis of P7 Pdot Formation.

Table 3.7. Quantum Yield Analysis of P2-P7 Pdot Formation Polymers

Polymer Name	Polymer Ratio M1:M2	QY of the Polymers
P2	10:1	%0,05
P3	5:1	%2
P4	1:1	%5,75
P5	1:5	%8,5
P6	1:10	%10,1
P7	Homopolymer	%9,8

With the nanophase separation method, Pdots containing single-chain conjugated polyelectrolyte are formed by a rapid nanophase separation between water (a poor solvent) and ethylene glycol (a good solvent). (Özenler et al. 2019) Pdots obtained with this method were found to have high absorbance coefficient, high quantum yield, and photostability. It is observed that polymers containing mostly hydrophobic monomers in their structure have higher Quantum Yield results in MeOH solvent, while polymers containing mostly hydrophilic monomers in their structure have higher Quantum Yield results in Pdot structure.

3.2.8. Raman Analysis of the Polymers Particles

Raman Analysis was performed with approximately 10 mg of synthesized polymers. Due to the structure of the polymers, it was aimed to obtain information about the signals to be received from the Raman active regions and the intensities of these signals, as well as the 3D structure and structural conformation of the polymers. (Brambilla et al. 2014) (Lopez Navarrete and Zerbi 1991) From the P2 polymer to the P7 polymer, the intensity in all polymer peaks except the P7 polymer increases.

Raman spectra of conjugated thiophene polymers are characterized by prominent lines in the energy range of 1600−1400 cm^{-1}, especially of the C=C stretching modes.(Hernandez et al. 1994) For example, the strong signals at 1400 cm^{-1} are associated with the symmetric mode of planar and coplanar polythiophene chains.(Xu et al. 2024) When the conformation of the backbone is disrupted, frequency is expected to shift to higher wavenumbers; this situation shoulders and shifts to higher wavelengths from P1 to P7. The reason for the three peaks observed in the P7 polymer is also due to the non-planar conformational structure of the polymer.

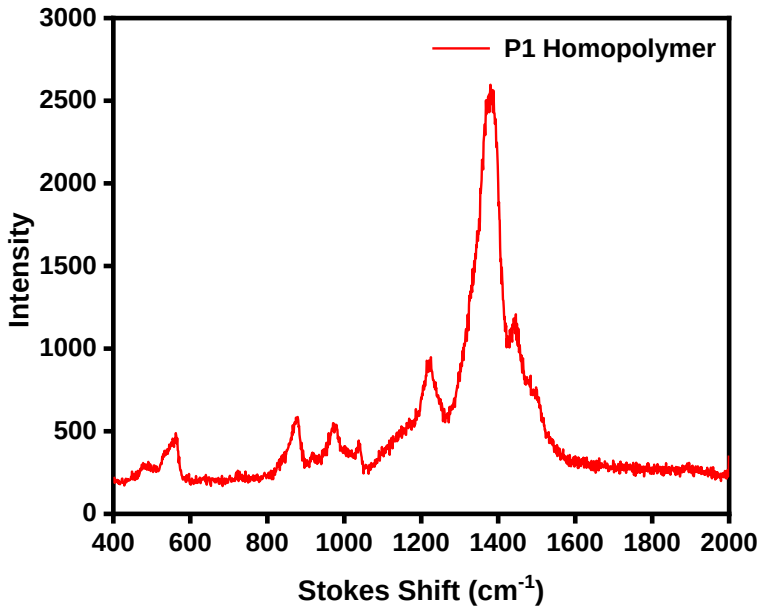

Figure 3.79. Solid Phase Raman Spectrum of the P1 (Homo M1) Polymer

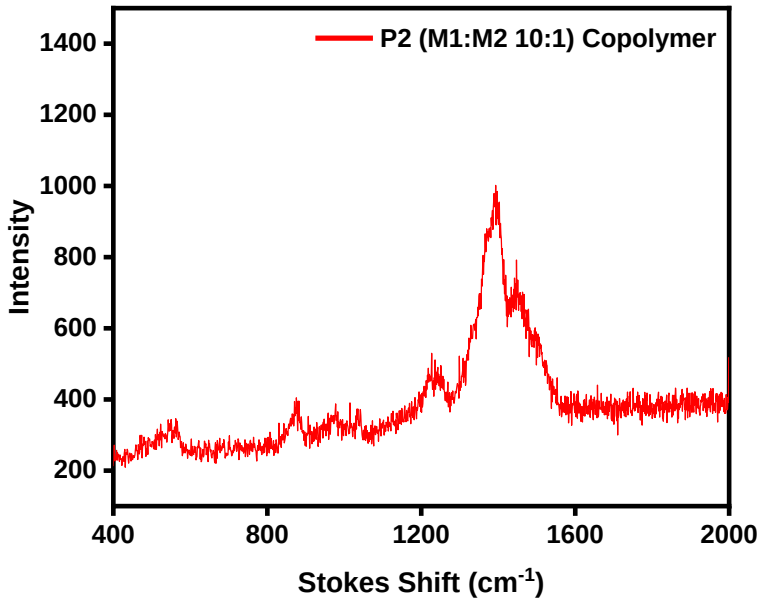

Figure 3.80. Solid Phase Raman Spectrum of the P2 (M1:M2 10:1) Polymer

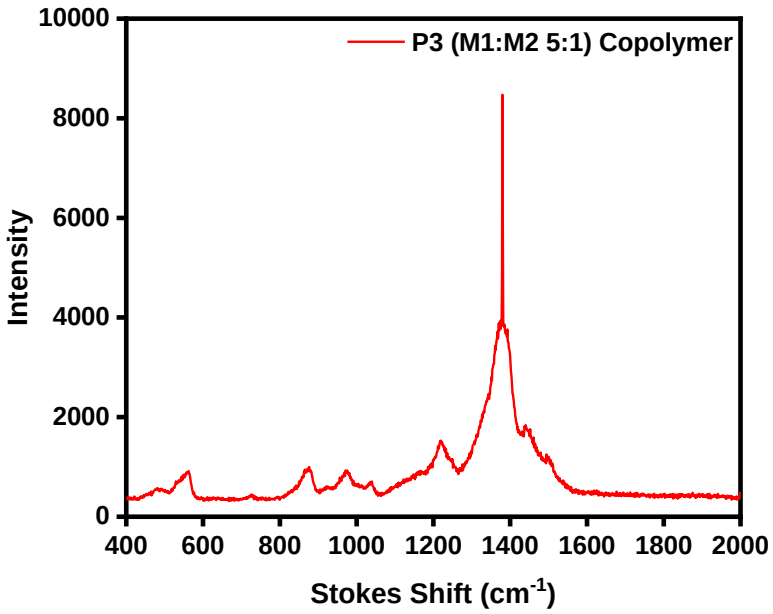

Figure 3.81. Solid Phase Raman Spectrum of the P3 (M1:M2 5:1) Polymer

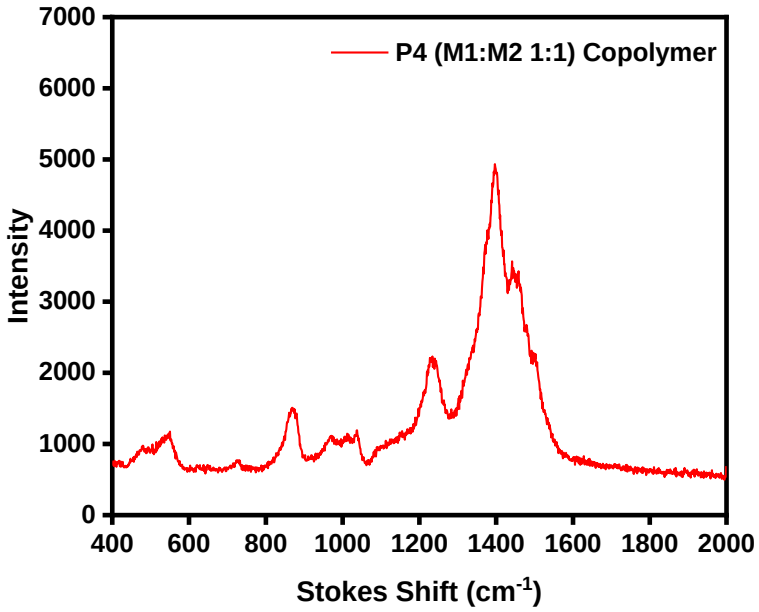

Figure 3.82. Solid Phase Raman Spectrum of the P4 (M1:M2 1:1) Polymer

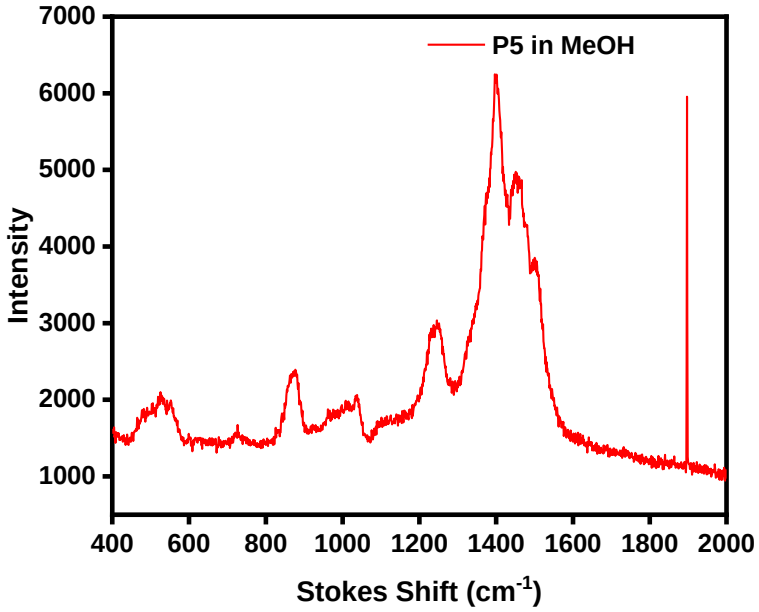

Figure 3.83. Solid Phase Raman Spectrum of the P5 (M1:M2 1:5) Polymer

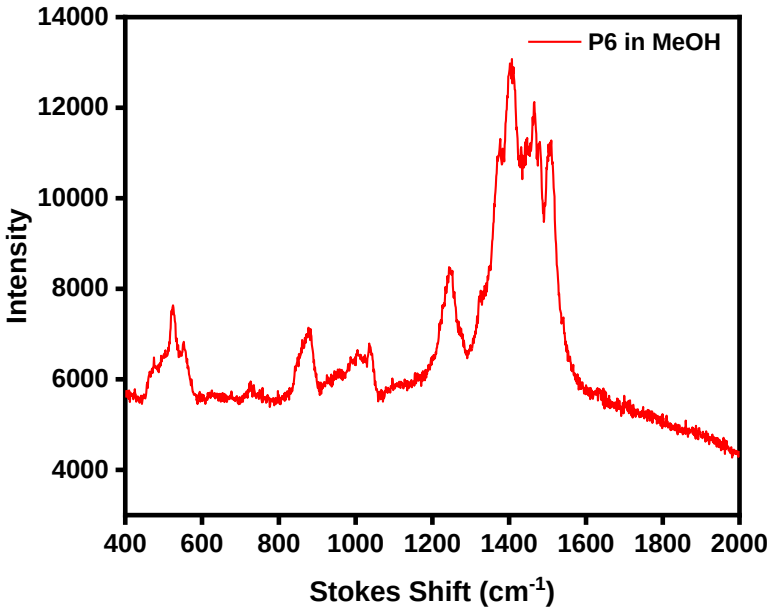

Figure 3.84. Solid Phase Raman Spectrum of the P6 (M1:M2 1:10) Polymer

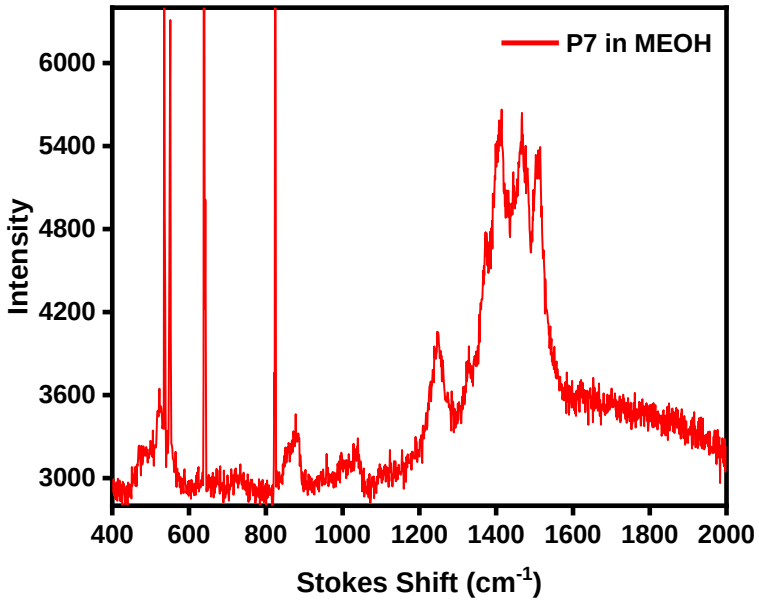

Figure 3.85. Solid Phase Raman Spectrum of the P7 (M2 Homo) Polymer

3.2.9.Raman Analysis of the Polymers on LAM

To observe the behaviors of polymers in different conformations in Raman analysis, polymers were dissolved with solvent and coated on glass slide after solid phase analyses. Solutions of all polymers were prepared in their own solvents at a concentration of 0.5 mg/ml. Polymer P1 was dissolved in chloroform, P2-P7 in methanol, and added dropwise onto the glass slide and dried in the oven. To coat layer by layer, a new layer was added after each layer dried in the oven set at 50 °C. Approximately 10 layers were formed for each polymer, dried, and Raman analysis was repeated. The figure shows the Raman Spectrum of the polymers taken after dissolving in their solvent and drying it on a slide. Compared to the Raman analysis taken in the dry phase, the intensities seen in the spectrum are much higher. It has been observed that taking Raman analysis by making film-shaped coatings is much more effective than taking analysis in the dry phase.

The signals in film coating Raman analyses of polymers have higher signal strengths than those in solid phase Raman analyses. The reason is the conformation of the polymers changing from P1 to P7. The 1500-1600cm^{-1} signals seen in the Raman spectrum from P1 to P7 are also due to the non-planar conformation of the polymer.

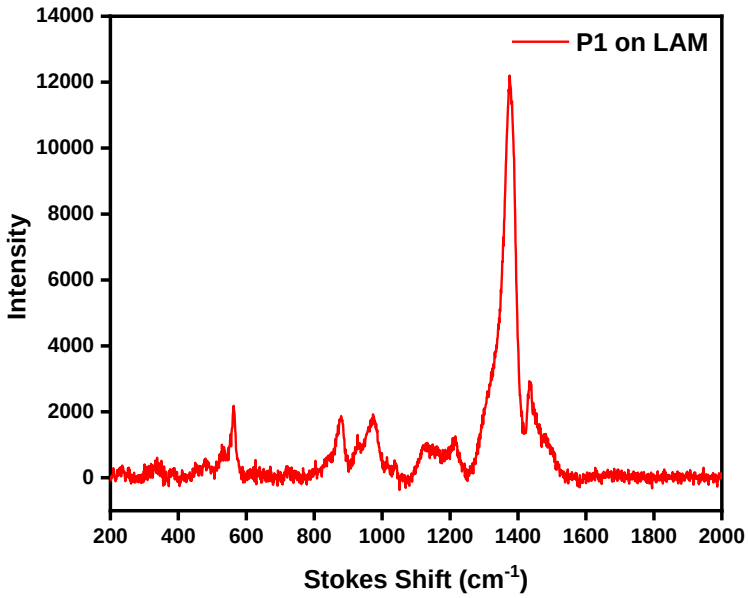

Figure 3.86. Film Coated Raman Spectrum of the P1 (Homo M1) Polymer

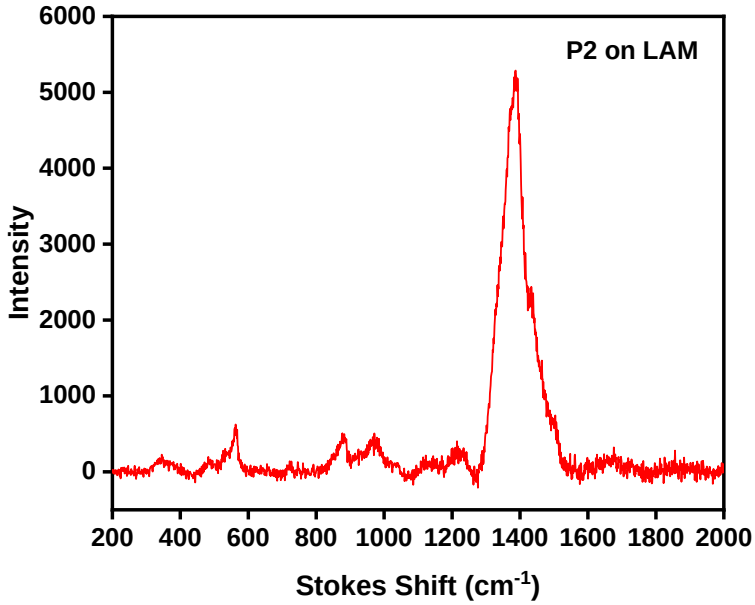

Figure 3.87. Film Coated Raman Spectrum of the P2 (M1:M2 10:1) Copolymer

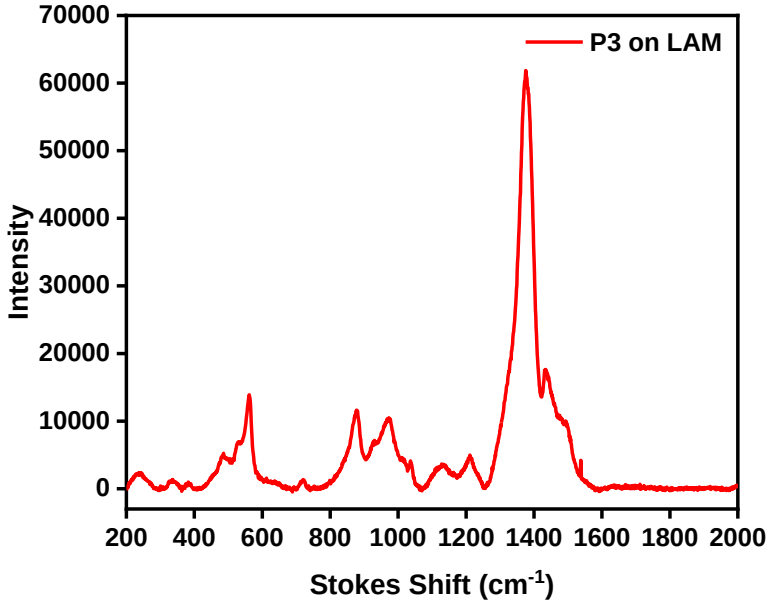

Figure 3.88. Film Coated Raman Spectrum of the P3 (M1:M2 5:1) Copolymer

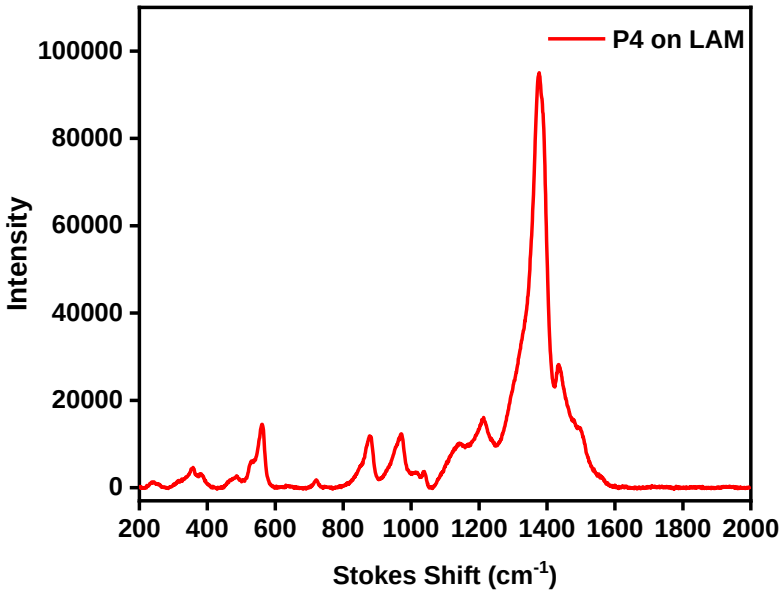

Figure 3.89. Film Coated Raman Spectrum of the P4 (M1:M2 1:1) Copolymer

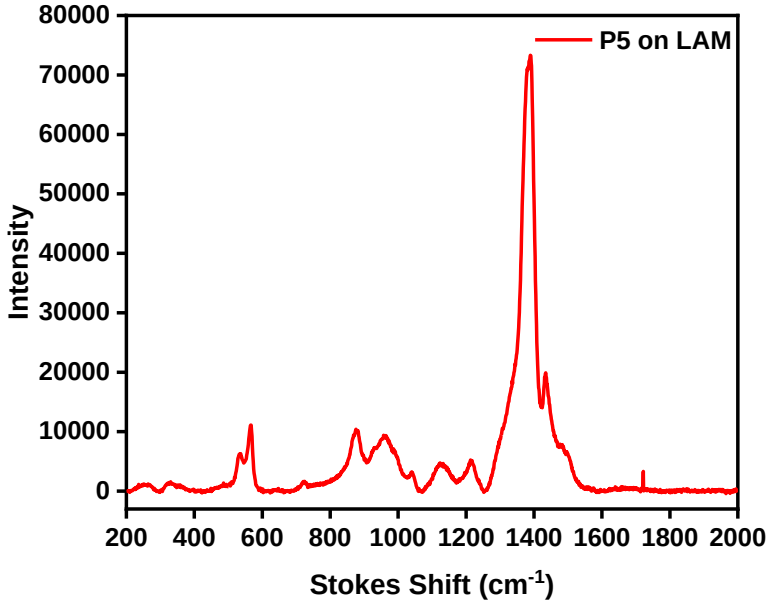

Figure 3.90. Film Coated Raman Spectrum of the P5 (M1:M2 1:5) Copolymer

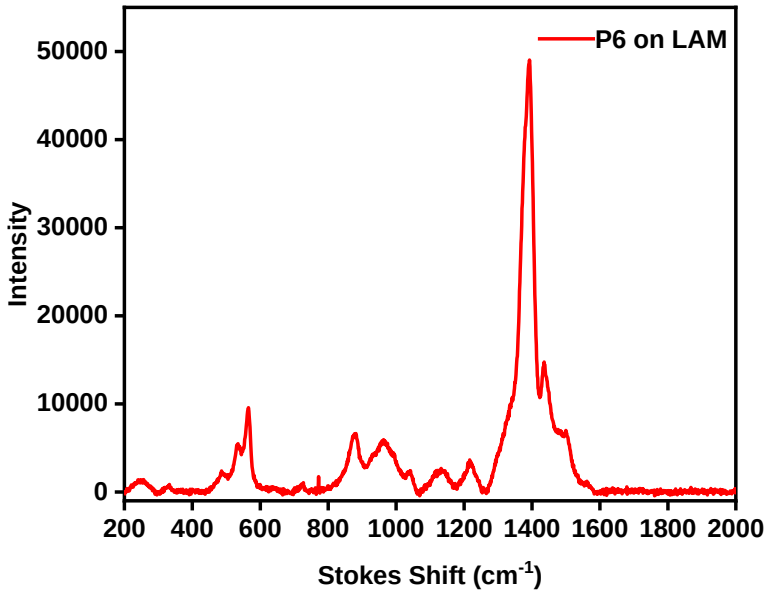

Figure 3.91. Film Coated Raman Spectrum of the P6 (M1:M2 1:10) Copolymer

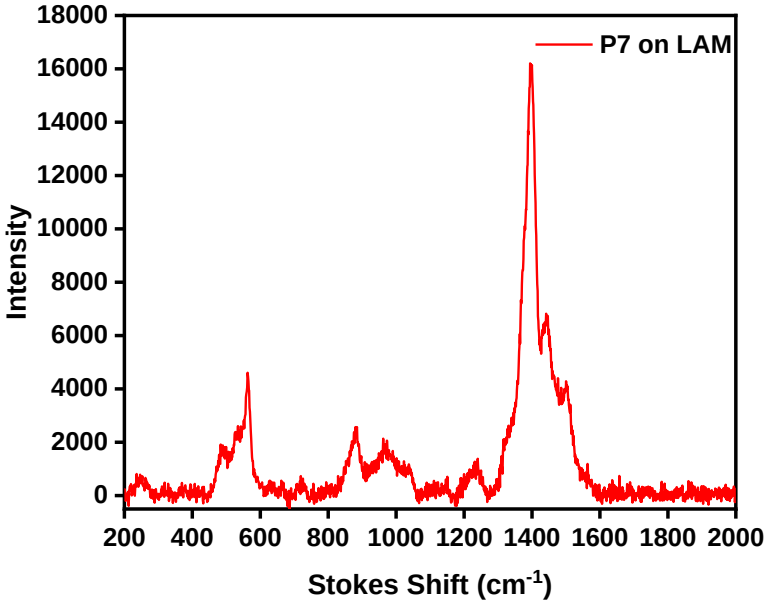

Figure 3.92. Film Coated Raman Spectrum of the P7 (Homo M2) Polymer

3.2.10. Zeta-Sizer Analysis of the Polymer

Zeta potential measurements are a technique used to evaluate the surface charge of a particle, colloid, or macromolecule and its electrostatic interactions with the surrounding liquid medium. The charges of polymers and the effect of copolymer reactions on the charge distribution are shown in graphs**.**

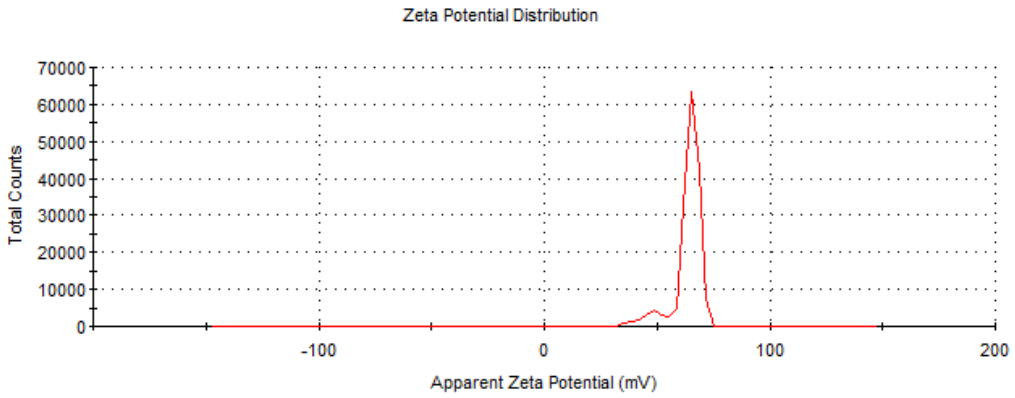

Figure 3.93. Zeta Potential Spectrum of P2 polymer

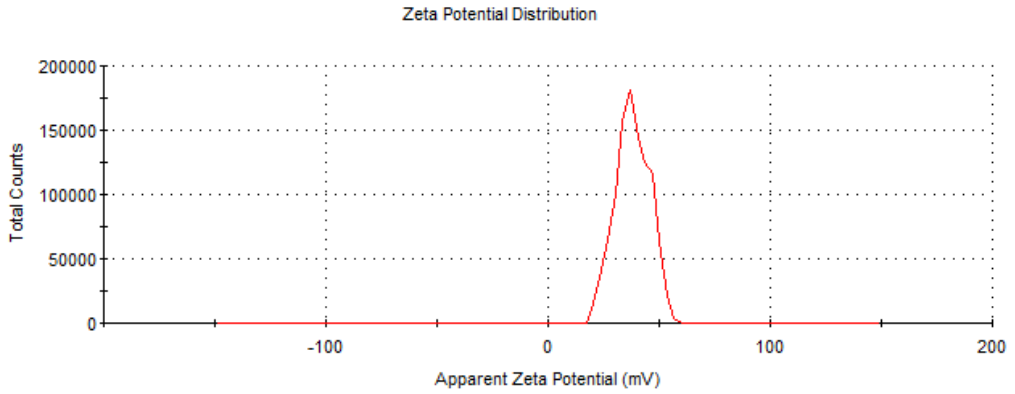

Figure 3.94. Zeta Potential Spectrum of P3 polymer

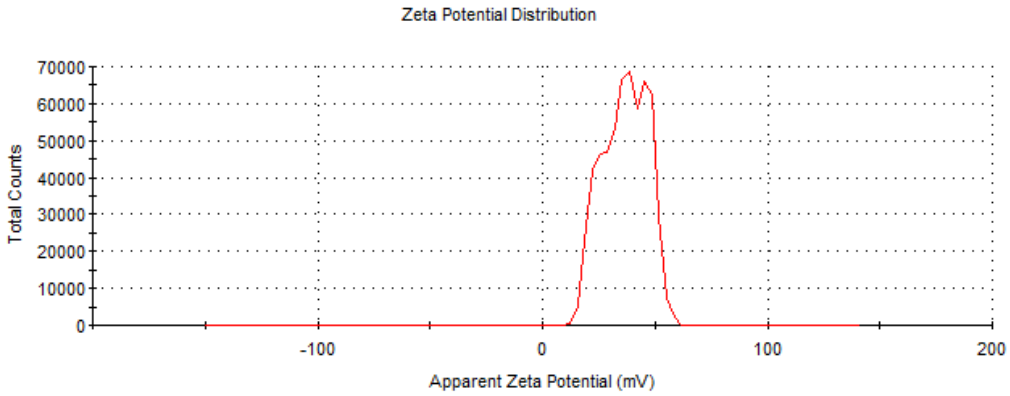

Figure 3.95. Zeta Potential Spectrum of P4 polymer

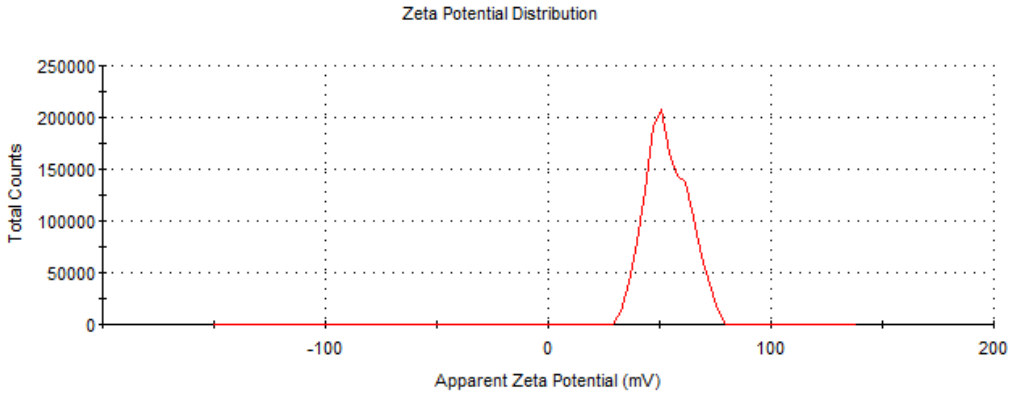

Figure 3.96. Zeta Potential Spectrum of P5 polymer

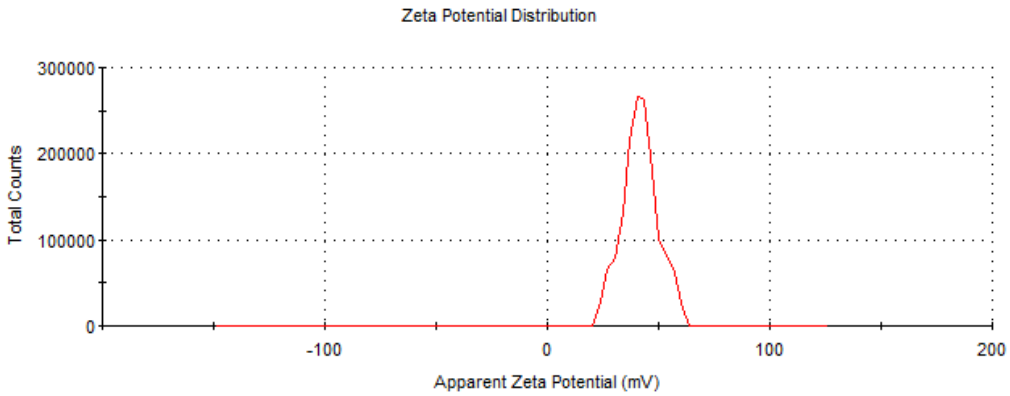

Figure 3.97. Zeta Potential Spectrum of P6 polymer

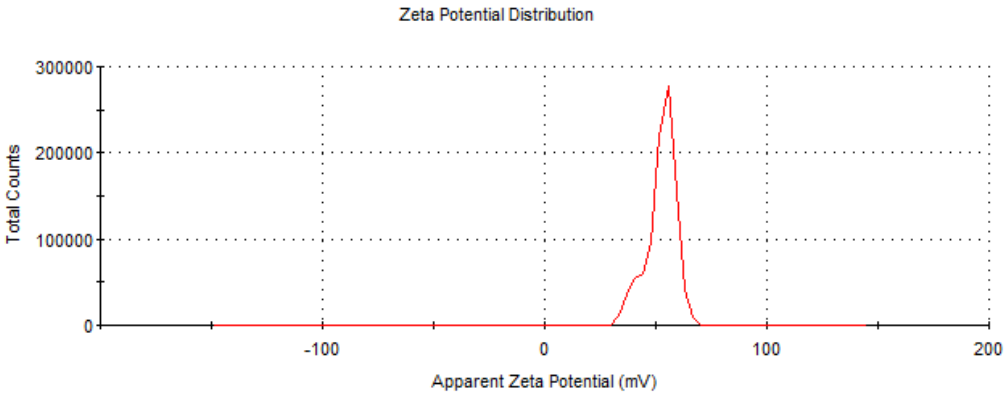

Figure 3.98. Zeta Potential Spectrum of P7 polymer

In the Zeta analyses, the increase in the cationic monomer ratio causes a positive increase in the surface charge of the copolymer. This is since the cationic monomers contain positively charged groups, making the net surface charge of the copolymer more positive. In the zeta potential analysis of the polymers, it was observed that the surface charge increased with the ratio of cationic monomer from polymer P2 to P7. Specifically, the measured surface charge of polymer P2 was determined to be 34.8 eV, whereas for polymer P7, it increased to 44 eV. This trend indicates a direct correlation between the cationic monomer content and the magnitude of the polymer's surface charge.

Table 3.8. Table Representation of Zeta Potentials of Polymers

Polymer Name	**Copolymer Ratio M1:M2**	**Charge of the Polyners**
P2	10:1	34,8 mV
P3	5:1	38 mV
P4	1:1	36.7 mV
P5	1:5	53.5 mV
P6	1:10	42mV
P7	Homopolymer	44 mV

CHAPTER 4

APPLICATIONS

4.1.Blood-Brain Barrier Bioimaging Applications

The blood-brain barrier (BBB) is a selective physiological barrier that surrounds the central nervous system (CNS) and maintains brain homeostasis. There are tight junctions between the endothelial cells of the brain capillaries, and this structure prevents the passage of harmful substances, toxins and pathogens into the brain tissue, while allowing the controlled transport of necessary nutrients and gases. While lipophilic and small molecules can easily pass through this barrier, hydrophilic and large molecules generally cannot. This selective permeability of the BBB makes it difficult for drugs to be effectively delivered to the brain in the treatment of neurological diseases, and therefore the development of new carrier systems and molecular structures is gaining importance.

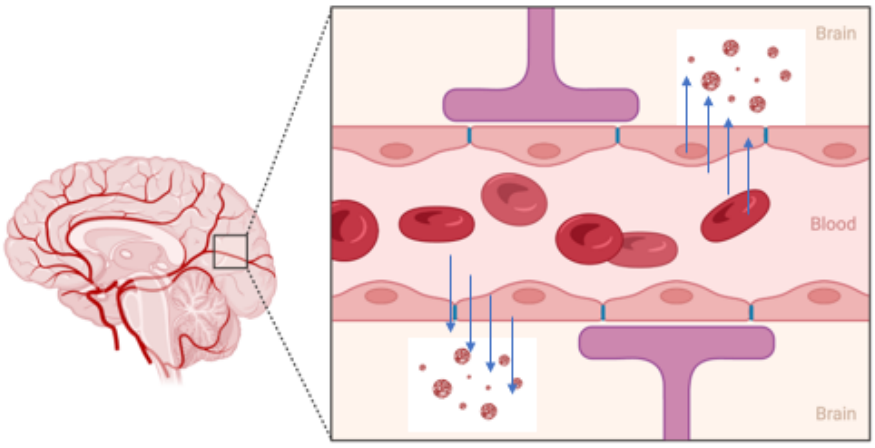

Figure 4.1. Illustration of Blood-Brain Barrier

Light microscope images of time-dependent profiles of 2D cultured cells are shared. When the 2D cultured cell lines reached 80-90% growth rate, they were lifted

from the surface with trypsin. After trypsin was inactivated in serum-based medium, centrifugation was applied to remove the trypsin medium and collect the cells.

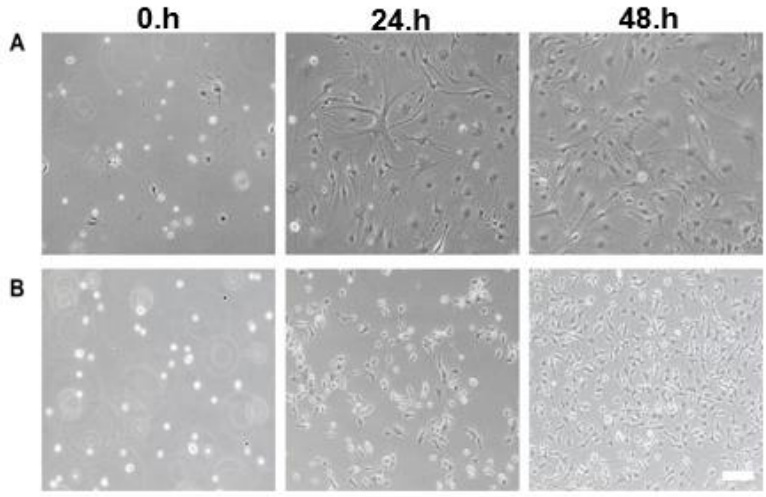

Figure 4.2. Light microscope images of 2D cultured cells A) bEnd.3 cells B) SH-SY5Y cells (Scale size: 100 µm)

Fluorescence microscopy images visualize the location, distribution, dynamics, and molecular interactions of cellular structures. Specific dyes or labels can determine the location of proteins, organelles, and other targets within the cell, while molecular movements, interactions, and environmental changes (pH, ion concentration) can be observed in living cells. Fluorescence intensity can also be used to measure the number of molecules. Abnormalities can also be detected, and 3D structures can be analyzed, allowing detailed studies of biological processes. Calcein Green is a fluorescent dye used to examine cell viability and membrane integrity. It emits bright green fluorescence in living cells because it is permeable to the cell but cannot accumulate in dead cells. The effects of P2, P4 and P6 on the viability of 2D SH-SY5Y cells at 24, 48 and 72 hours were examined. Fluorescent microscope images obtained with Calcein Green staining were shared.

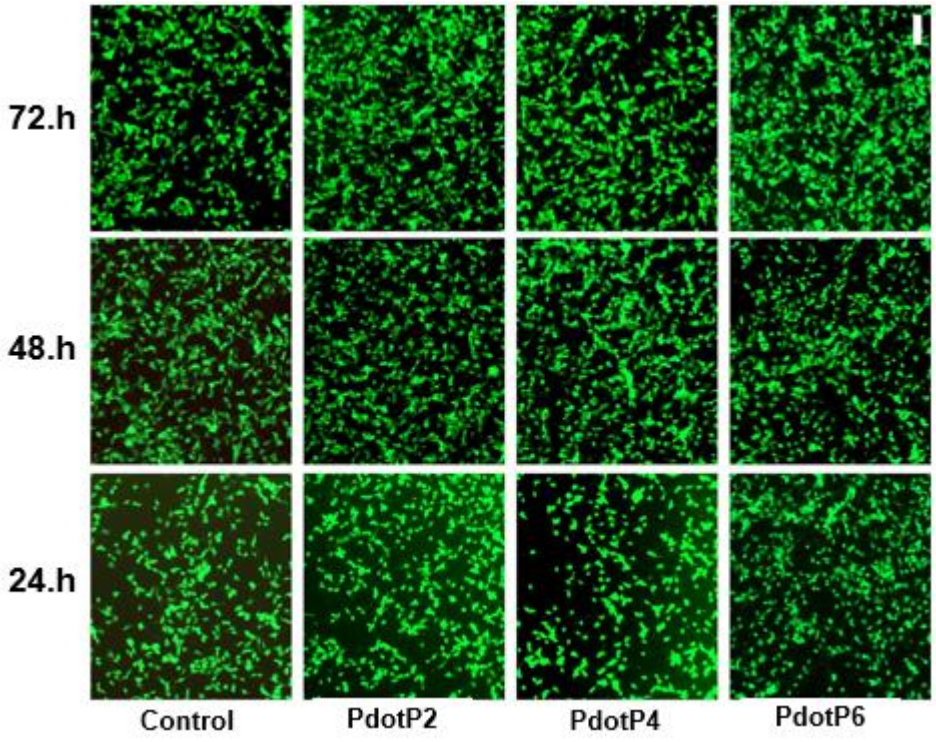

Figure 4.3. Effect of P2, P4 and P6 on the viability of 2D SH-SY5Y cells at 24, 48 and 72 h. Fluorescence microscope images obtained by Calcein Green staining (Scale size: 100 μm)

MTT analysis is a method used to measure cell viability and proliferation. Mitochondrial enzymes reduce the MTT salt to insoluble purple formazan crystals; this occurs only in metabolically active cells. The crystals are dissolved, their absorbance is measured, and cell viability is quantitatively assessed. As a result of the analysis of the viability of 2D SH-SY5Y cells, P2-P4 and P6 polymers by the MTT method, the viability results of three Pdot samples were observed to be at least 80 percent.

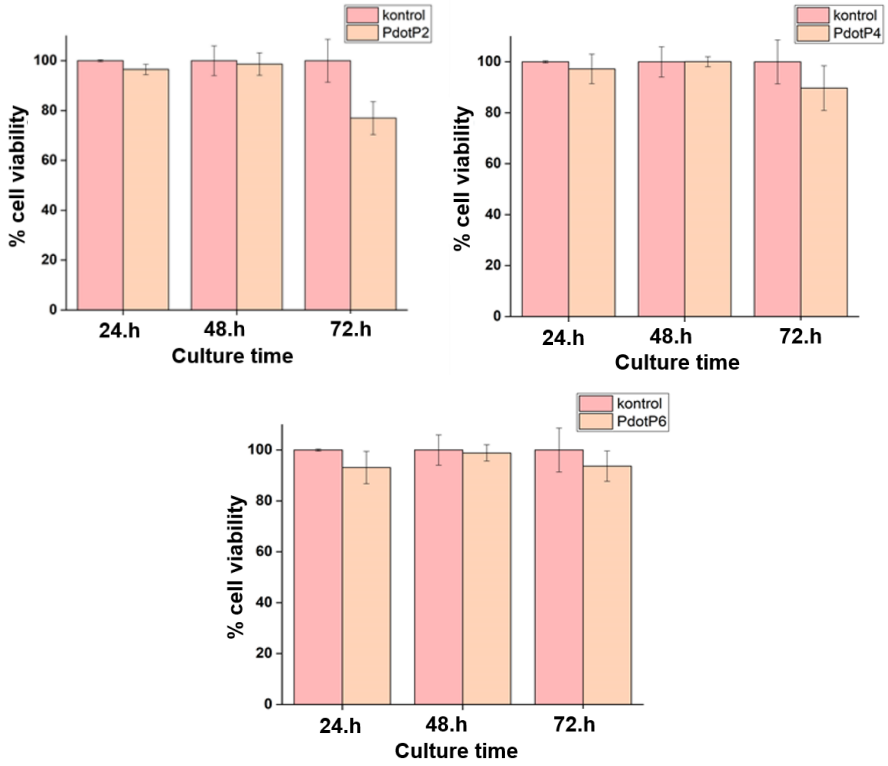

Figure 4.4. Effect of P2 (M1:M2 10:1), P4 (M1:M2 1:1) and P6 (M1:M2 1:10) on the viability of 2D SH-SY5Y cells at 24, 48 and 72 hours. Graphs of cell viability results obtained from MTT (methyltetrazolium) analysis**.**

Fluorescence microscopy images visualize the location, distribution, dynamics, and molecular interactions of cellular structures. Specific dyes or labels can determine the location of proteins, organelles, and other targets within the cell, while molecular motions, interactions, and environmental changes can be observed in living cells.

In the image, three different polymer dots (PdotP2, PdotP4 and PdotP6) were tested on cells. DAPI dye marked the cell nuclei in blue. Pdot (red) shows the distribution of polymer dots within the cell. CALCEIN (green) live cell dye confirms cell viability. In the combined image (DAPI + Pdot), both nuclei and distribution of polymer can be observed. It is observed that Pdots are taken up into the cells and do not affect cell viability.

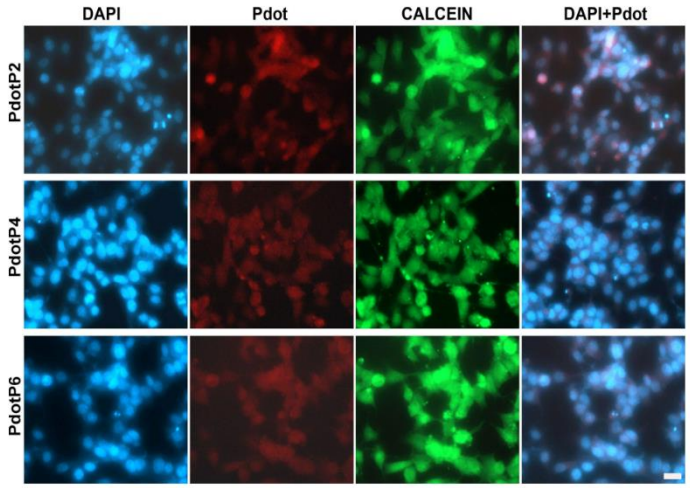

Figure 4.5. Fluorescence microscopy image of 2D SH-SY5Y cells treated with P2, P4 and P6 (blue: DAPI, red: Pdot, green: Calcein Green) (Scale size: 20 µm)

The effect of PdotP2, PdotP4 and PdotP6 polymers on the viability of 2D bEnd.3 cells were evaluated for 24, 48 and 72 hours. Green color represents live cells. In all groups, cells proliferated, and cell density increased over time. Cell density reached the highest level at 72 hours, indicating that Pdots had no negative effect on cell viability. PdotP2, PdotP4 and PdotP6 were not cytotoxic and did not affect cell growth.

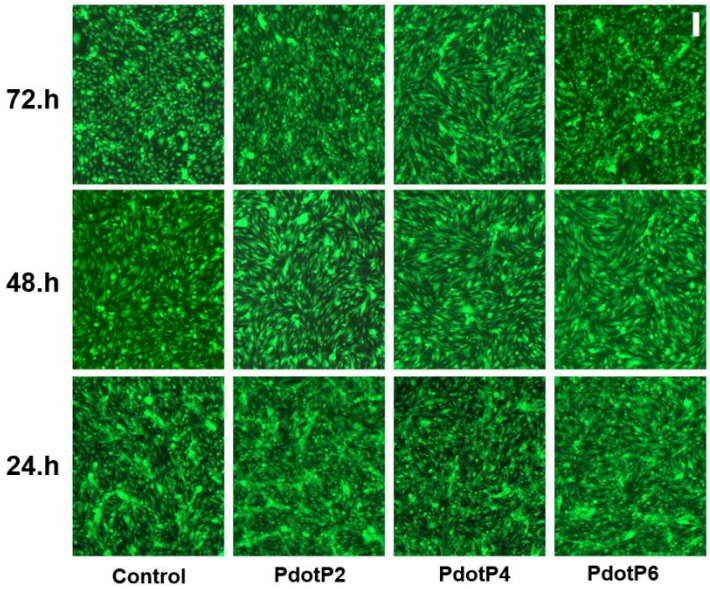

Figure 4.6. Effect of PdotP2, PdotP4 and PdotP6 on the viability of 2D bEnd.3 cells at 24, 48 and 72 hours. Fluorescence microscope images obtained because of Calcein Green staining (Scale size: 100 µm)

MTT analysis of the viability of 2D SH-SY5Y cells treated with P2, P4 and P6 polymers showed that all three Pdot samples-maintained cell viability at least 85%.

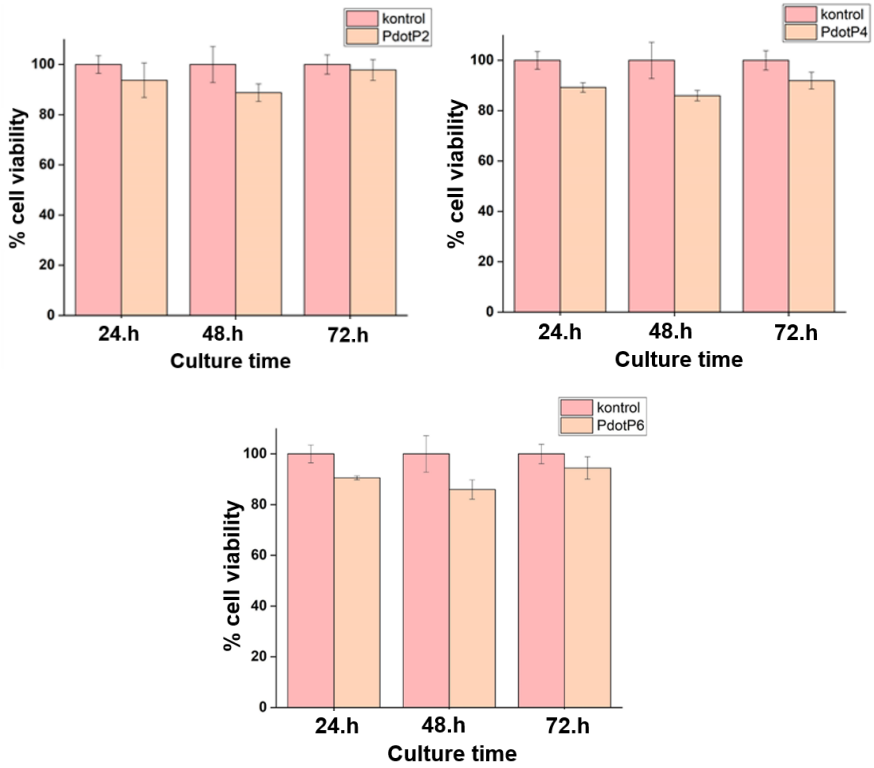

Figure 4.7. Effect of P2 (M1:M2 10:1), P4 (M1:M2 1:1) and P6 (M1:M2 1:10) on the viability of 2B bEnd.3 cells at 24, 48 and 72 hours. Graphs of cell viability results obtained from MTT analysis.

In PdotP2, PdotP4 and PdotP6 groups, the integrity of the nucleus was preserved, and no deterioration or irregularity was observed in the nucleus structure. The homogeneous distribution of the nuclei supports that the cells are healthy, and that cell death is minimal. The signals of the polymer dots do not overlap with the blue nuclei stained with DAPI, proving that the Pdots do not enter the nucleus and are localized in the cytoplasm. The CALCEIN signal is strong in all groups, indicating that most of the cells are alive. No significant negative effect of the polymers on cell viability was observed.

It was concluded that the PdotP2, PdotP4 and PdotP6 polymers were effectively taken into the cells, stayed away from the nucleus and did not negatively affect cell viability.

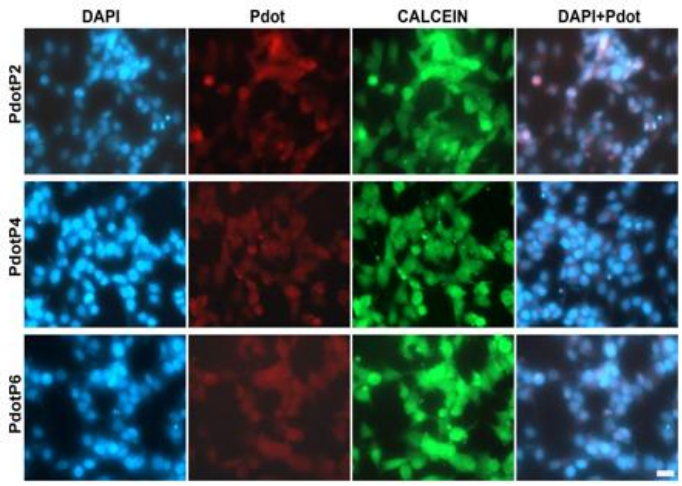

Figure 4.8. Fluorescence microscopy image of 2D bEnd.3 cells treated with P2, P4 and P6 (blue: DAPI, red: Pdot, green: Calcein Green) (Scale size: 20 µm)

After examining the effect of Pdots on cell viability and growth in the standard 2D cell culture model, the blood-brain barrier was established with SH-SY5Y and bEnd.3 cells using Transwells. To determine the effect of cell numbers on the blood-brain barrier, bEnd.3 cells propagated with the standard 2D culture method were seeded on the surface of Transwells (pore size 0.4 µm, PET membrane) placed in 24-microplates at cell numbers of 1×10^4 and 5×10^4. Culture was continued at 37ºC and 5% CO2 conditions until bEnd.3 cells formed a barrier on the filter, and monoculture was established.

After culture, the integrity of the brain endothelial layer was evaluated by measuring the trans-endothelial electrical resistance (TEER). After the bEnd.3 cells covered the entire filter surface and the maximum TEER value was obtained, SH-SY5Y cells were seeded in the wells as 1×10^5 cells, and co-culture was established. Cell culture medium and culture conditions do not differ for monoculture and coculture.

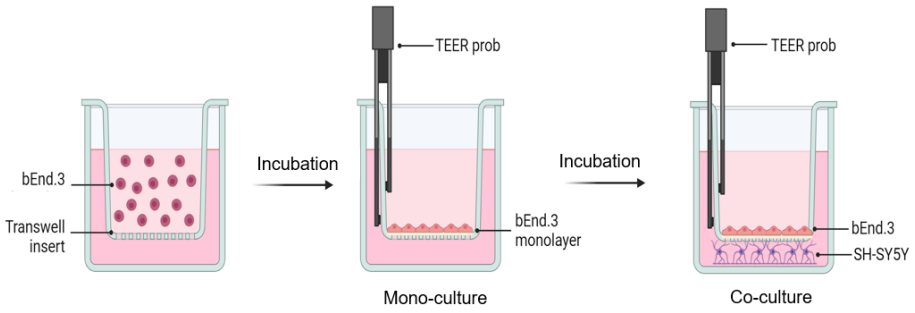

Figure 4.9. Establishment of the blood-brain barrier with bEnd.3 and SH-SY5Y cells using the Transwell system

TEER values for different cell numbers of bEnd.3 cells depending on the culture time are shown. During this process, a cell-free Transwell was used as a blank and analyzed under the same conditions as the experimental group. After recording the resistance values obtained during the measurement, the value was calculated using this TEER equation $TEER = (R_{total} - R_{blank}) \times A\ (ohmcm^2)$. Here R_{total} is the resistance between the cell layers on the permeable filters, Rblank is the resistance of the permeable filters without cells and A is the surface area of the filter.

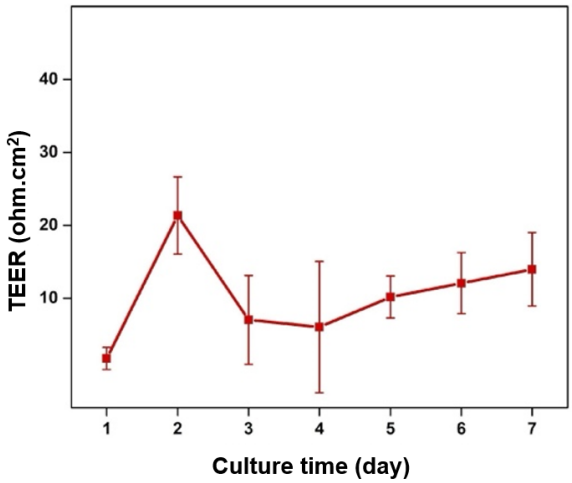

Figure 4.10. TEER values measured according to the culture time of bEnd.3 (1×10^4) cells on Transwell.

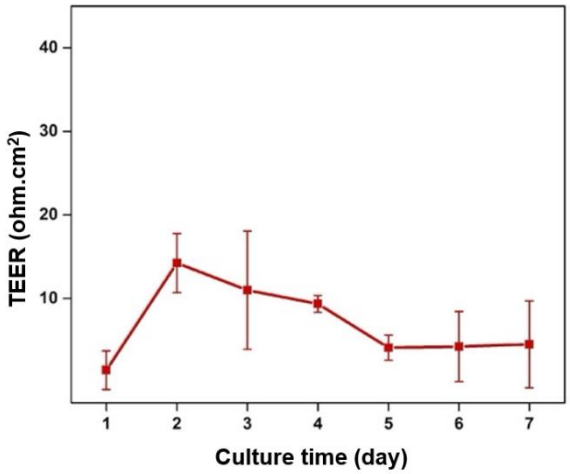

Figure 4.11. TEER values measured according to the culture time of bEnd.3 (5×10^4) cells on Transwell.

Papp changes over time and provides an understanding of how much resistance this barrier provides to the passage of molecules at different time intervals. The fact that the Papp value is high at the beginning of the experiment, then decreases after the first minutes and then stabilizes shows that the blood-brain barrier stabilizes in a short time. As the connections between cells increase at the end of the first hour, the passage of molecules becomes more difficult. It is seen that the Papp value is balanced, and permeability decreases during this period. After 24 hours, the low permeability of the endothelial tissue formed by bEnd.3 cells indicate the effectiveness of the blood-brain barrier created. As a result, the low permeability coefficient for a long time supports that the cells form a successful barrier structure.

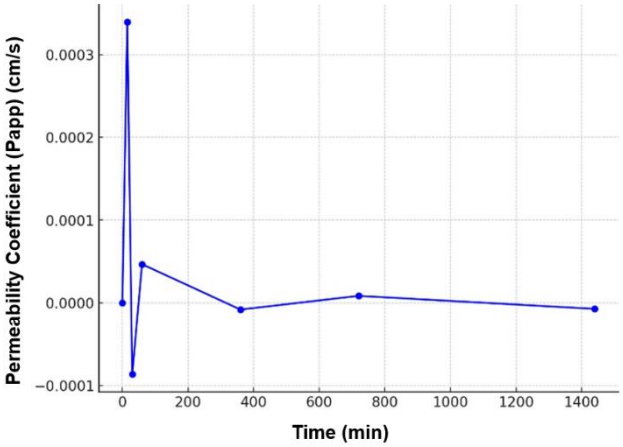

Figure 4.12. Graph showing the change of apparent permeability coefficient (Papp) over time.

After the bEnd.3 cells in the Transwell in the 24-microplate formed a barrier, they were first incubated with PdotP2. In addition to the barrier passage characteristics of the polymer, its effect on SH-SY5Y cells in the wells was also examined. It shows the fluorescence microscopy analyses of bEnd.3 and SH-SY5Y cells, respectively. At the end of 24, 48 and 72 hours, the cell cytoplasm was marked with Calcein Green, while the nucleus was marked with DAPI. In addition, after Pdot application, it was observed with a red fluorescence signal that PdotP2 was taken into the cells in both bEnd.3 and SH-SY5Y cells. Thus, it is shown that PdotP2 passed through the blood-brain barrier formed by bEnd.3 cells and reached SH-SY5Y cells in the wells. In addition, the visualization of the cells with Calcein Green at the end of 24, 48 and 72 hours and the high signal indicate that PdotP2 does not have a toxic effect on the cells.

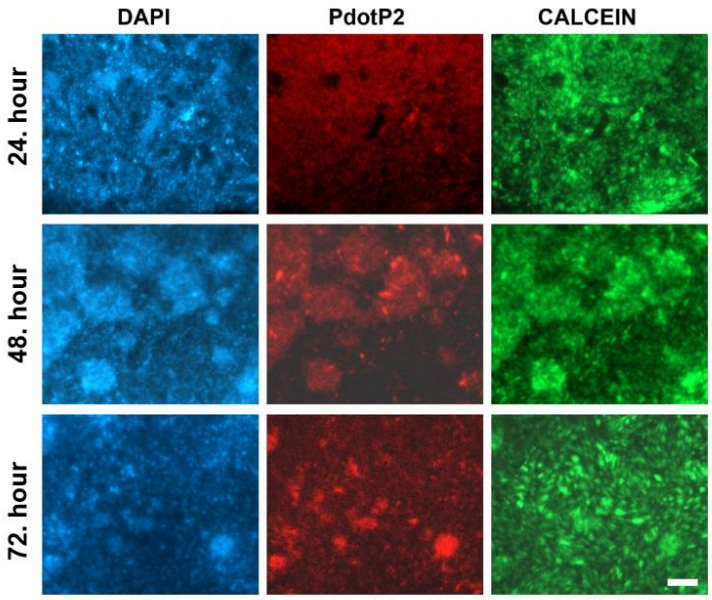

Figure 4.13. Fluorescence microscopy image of bEnd.3 cells on PdotP2-treated Transwell membrane (blue: DAPI, red: Pdot, green: Calcein Green) (Scale size: 200 μm).

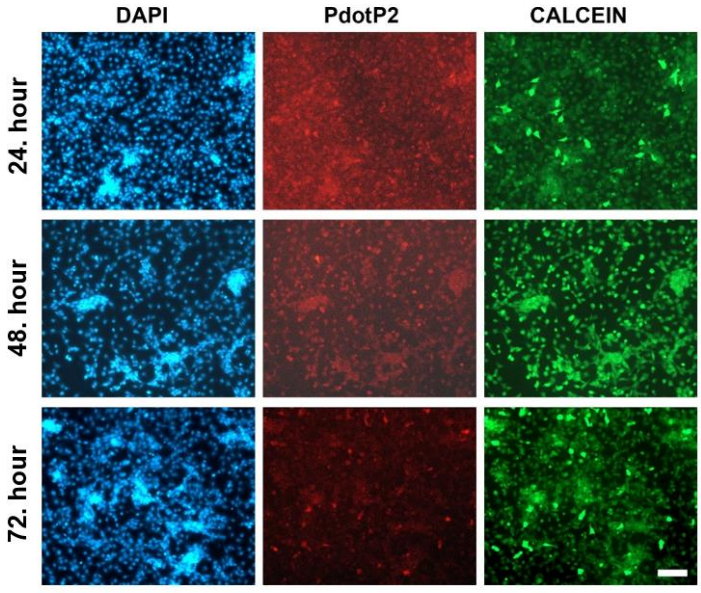

Figure 4.14. Fluorescence microscopy image of SH-SY5Y cells on PdotP2-treated Transwell membrane (blue: DAPI, red: Pdot, green: Calcein Green) (Scale size: 100 μm).

It shows the fluorescence microscopy analyses of bEnd.3 and SH-SY5Y cells after incubation with PdotP4, respectively. Similarly, at the end of 24, 48 and 72 hours, the cell cytoplasm was marked with Calcein Green, while the nucleus was marked with DAPI. The effect of PdotP4 applied after the formation of the blood-brain barrier on both bEnd.3 cells and its ability to pass through the barrier were interpreted. It was also observed in this experiment that PdotP4 passed through the barrier formed by bEnd.3 cells in the BBB model and reached the SH-SY5Y cells in the lower well, and these results show the capacity of PdotP4 to pass through the blood-brain barrier. In addition, the fact that the cells could still be visualized with Calcein Green dye at the end of the 24, 48 and 72 hour incubation process reveals that PdotP4 did not create any toxicity on the cells.

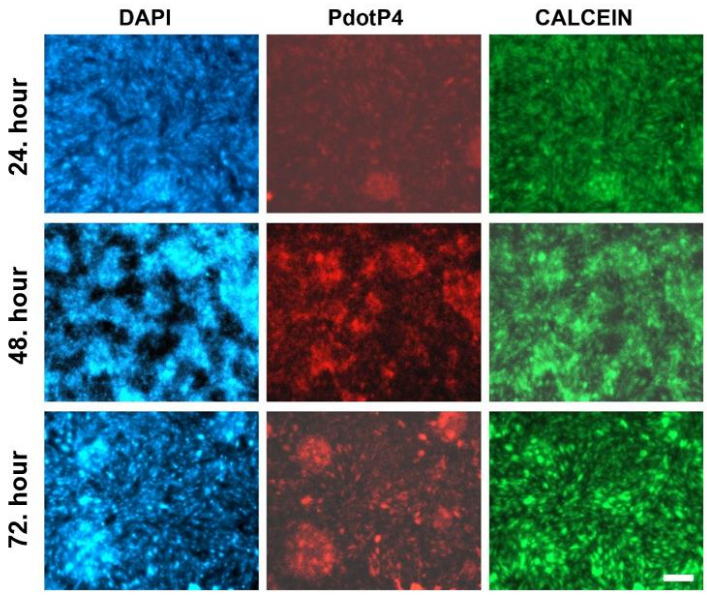

Figure 4.15. Fluorescence microscopy image of bEnd.3 cells on PdotP4-treated Transwell membrane (blue: DAPI, red: Pdot, green: Calcein Green) (Scale size: 200 μm).

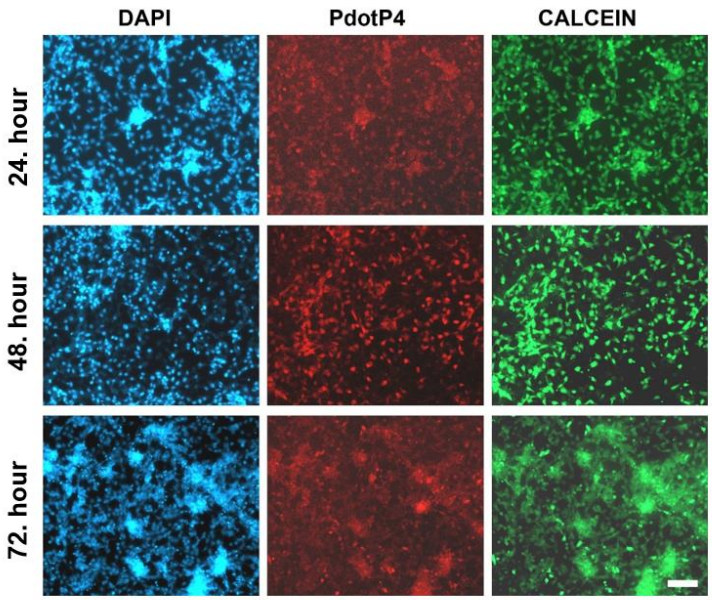

Figure 4.16. Fluorescence microscopy image of SH-SY5Y cells on PdotP4-treated Transwell membrane (blue: DAPI, red: Pdot, green: Calcein Green) (Scale size: 100 µm).

It shows PdotP6 analyses for bEnd.3 and SH-SY5Y, respectively. Similarly, at the end of 24, 48 and 72 hours, the cell cytoplasm was marked with Calcein Green, while the nucleus was marked with DAPI. As with other polymers, in this section, the effect of PdotP6 applied after the formation of the BBB on bEnd.3 cells and its barrier passage feature were interpreted with the help of a fluorescence microscope. The red fluorescence signal originating from PdotP6 indicates that this substance was taken into both bEnd.3 and SH-SY5Y cells. As with other Pdots, the red signal observed in SH-SY5Y cells is an indicator of PdotP6 passage through the barrier. At the same time, the green signal given by the cells with Calcein Green during the 24, 48 and 72 hour period indicates that the cells remained alive and metabolically active during this period. In this case, the fact that the cells were not damaged during the long culture period provides a positive indicator about the biocompatibility of Pdots (P2, P4 and P6). This finding also suggests that Pdots (P2, P4 and P6) do not damage brain cells after crossing the BBB and are potentially safe to use in neural systems.

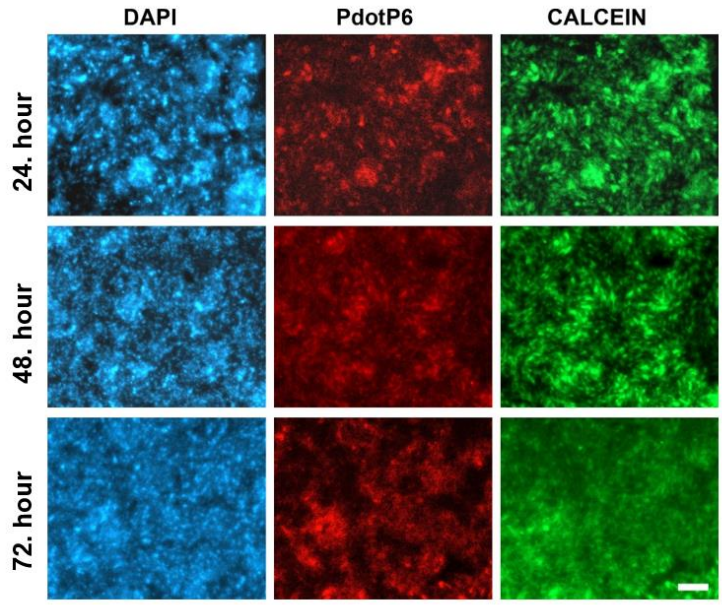

Figure 4.17. Fluorescence microscopy image of bEnd.3 cells on PdotP6-treated Transwell membrane (blue: DAPI, red: Pdot, green: Calcein Green) (Scale size: 200 μm).

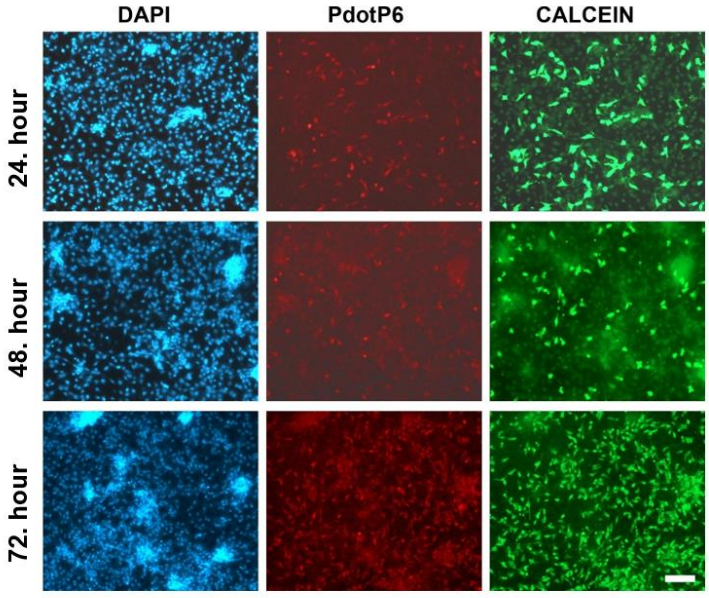

Figure 4.18. Fluorescence microscopy image of SH-SY5Y cells on PdotP4-treated Transwell membrane (blue: DAPI, red: Pdot, green: Calcein Green) (Scale size: 100 μm).

It shows the MTT results of bEnd.3 and SH-SY5Y cells treated with PdotP2 after BBB formation at the end of 24, 48 and 72 hours and the effect of PdotP2 on cell viability. The graph shows the MTT analysis performed at three different time points (% cell viability) at the end of 24 hours, 48 hours and 72 hours for two different cell types. Green columns represent the control group (cells without PdotP2), blue columns represent PdotP2-treated cells. After bEnd.3 cells on Transwell membrane were incubated with PdotP2, cell viability was recorded as 98% after 24 hours, 100% after 48 hours and 81% after 72 hours. Simultaneously, SH-SY5Y cells in the wells of 24-microplates treated with PdotP2, which passes through the blood brain barrier, had a cell viability of 98% after 24 hours and 100% at the end of 48th and 72nd hours.

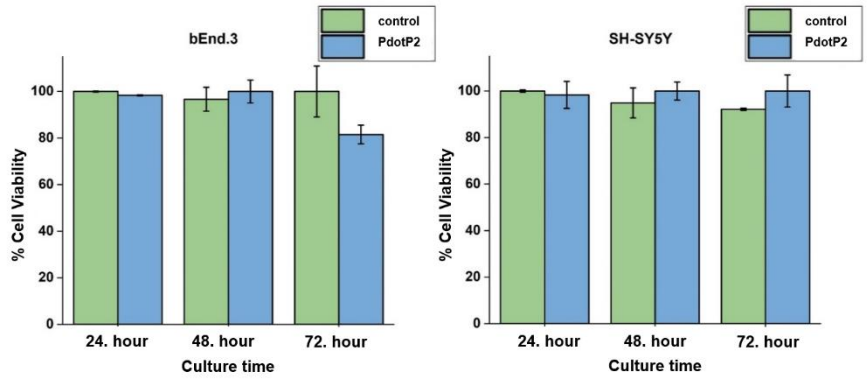

Figure 4.19. Effect of PdotP2 on the viability of bEnd.3 and SH-SY5Y cells at 24, 48 and 72 hours. Cell viability results obtained from MTT analysis.

It is investigating the effect of PdotP4 applied to bEnd.3 and SH-SY5Y cells on cell viability using the Blood-Brain Barrier model. After bEnd.3 cells were incubated with PdotP4 on Transwell membrane, cell viability was recorded as 93% after 24 hours and 100% at the end of 48th and 72nd hours. Simultaneously, SH-SY5Y cells treated with PdotP4 in 24-microplate wells and passing through the blood-brain barrier had cell viability of 98% after 24 hours and 100% at the end of 48th and 72nd hours.

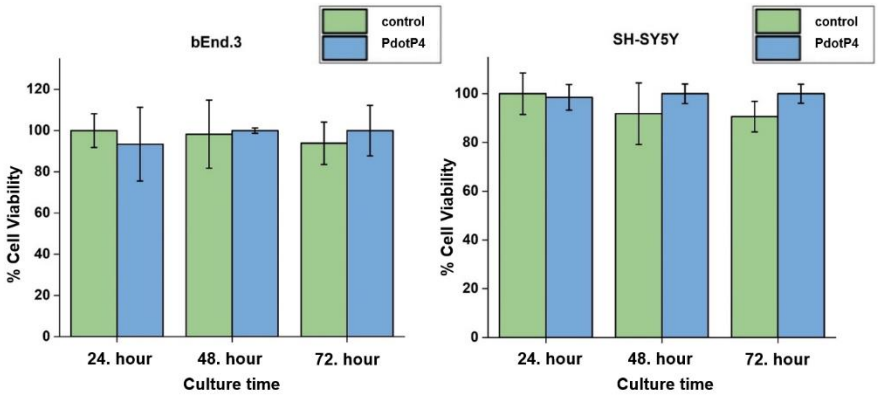

Figure 4.20. Effect of PdotP4 on the viability of bEnd.3 and SH-SY5Y cells at 24, 48 and 72 hours. Cell viability results obtained from MTT analysis.

The results of MTT analysis of bEnd.3 and SH-SY5Y cells treated with PdotP6 after the formation of the blood-brain barrier and the effect of PdotP6 on cell viability are shown. After incubation of bEnd.3 cells on transwell membrane with PdotP6, cell viability was recorded as 81% after 24 hours, 98% after 48 hours and 100% after 72 hours. Simultaneously, cell viability of SH-SY5Y cells treated with PdotP6 in 24-microplate wells and passing through the blood-brain barrier was observed as 92% after 24 hours, 80% after 48 hours and 92% after 72 hours.

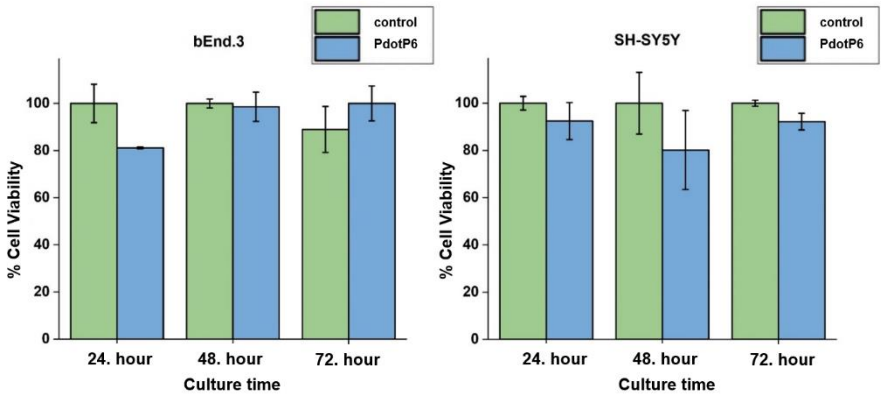

Figure 4.21. Effect of PdotP6 on the viability of bEnd.3 and SH-SY5Y cells at 24, 48 and 72 hours. Cell viability results obtained from MTT analysis.

After observing the passage of Pdots through the BBB barrier with a fluorescence microscope, quantitative permeability analyses were also performed. bEnd.3 cells, which

were propagated by the standard 2D culture method to form the blood-brain barrier, were seeded in a volume of 1×104 cells, 100 µl, for each Transwell (pore size 0.4 µm, PET membrane) placed in 24-microplates. They were cultured at 37ºC and 5% CO2 conditions. The culture was continued until the maximum TEER value was obtained on the 2nd day, and then permeability analyses were started. The previously prepared Krebs Ringer uptake buffer and Pdot (P2, P4 and P6) solutions were prepared separately and added to the upper part of the Transwells. An uptake buffer was also added to the lower wells.

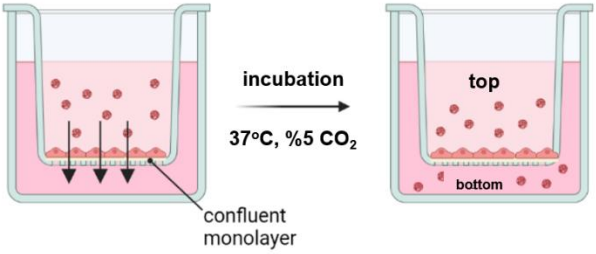

Figure 4.22. Schematic of permeability study in the blood brain barrier model.

To investigate the ability of PdotP2 to pass through the blood-brain barrier, samples were collected from the upper part of the Transwell and the lower well at 0, 12, 24, 48 and 72 hours, and absorbance measurements were made at 550 nm, and then PdotP2 passage was evaluated by comparing them to each other. While the absorbance ratio was 0.87 at 0 hour, the ratio increased to 0.96-0.98 between 12 and 24 hours, indicating that PdotP2 penetrated the barrier over time. The closer this ratio is to 1, the more transfer there is to the lower compartment. As of the 48th hour, the ratio appears to stabilize at a level close to 1, indicating that PdotP2 movement has reached equilibrium and is almost equal in both compartments. At the 72nd hour, the ratio exceeds 1, at which point the lower compartment probably has a slightly higher amount of PdotP2 due to diffusion dynamics or cellular uptake.

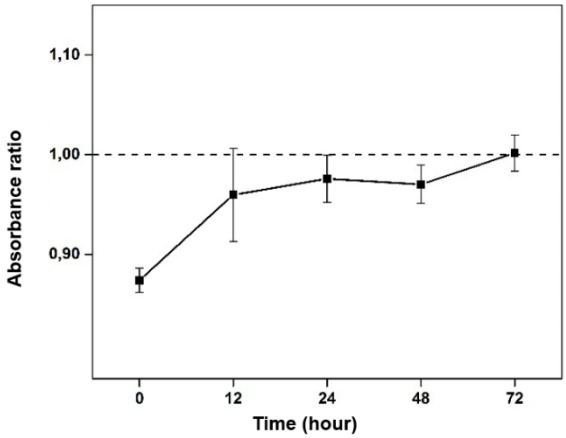

Figure 4.23. Permeability rate of PdotP2 in the blood-brain barrier model at 0, 12, 24, 48 and 72 hours.

Similarly, the behavior of PdotP4 passing through the blood-brain barrier has been examined and shared. While the absorbance ratio increases towards the 12th hour and approaches 1.0, it is observed that the absorbance ratio reaches its highest point at 48 hours, so there is more PdotP4 in the lower compartment than in the upper compartment during this period. The decrease in the ratio after 48 hours suggests that permeability may have reached equilibrium, or the blood-brain barrier model may have reached maximum permeability.

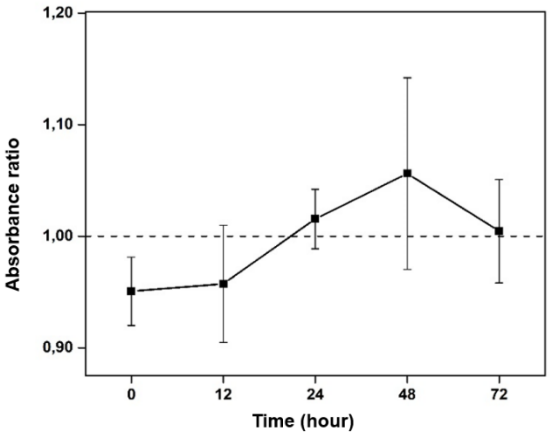

Figure 4.24. Permeability rate of PdotP4 in the blood-brain barrier model at 0, 12, 24, 48 and 72 hours.

The absorbance ratio in PdotP6 reached and even exceeded 1.0 in a shorter time compared to PdotP2 and PdotP4. This shows that PdotP6 began to pass through the blood-brain barrier in about 12 hours and was found in higher amounts in the lower compartment. The ratio began to fall below 1.0 within 48 hours and stabilized at a level close to 1.0 within 72 hours, indicating that equilibrium was reached.

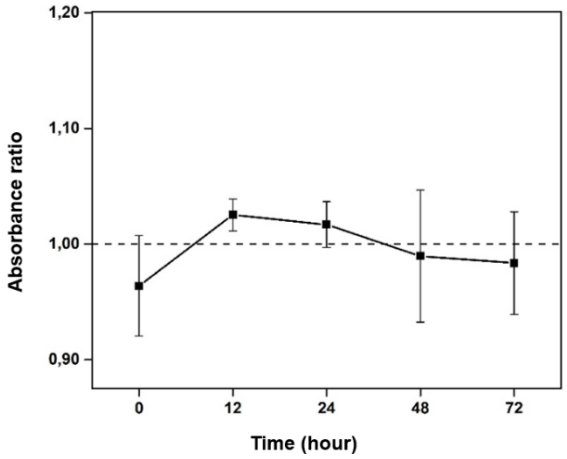

Figure 4.25. Permeability rate of PdotP6 in the blood-brain barrier model at 0, 12, 24, 48 and 72 hours.

When the synthesized Pdots are compared in terms of permeability; it is observed that P2 does not fully reach the peak point, which indicates that it has a lower tendency to penetrate the blood-brain barrier compared to P4. P4 shows the highest permeability among the three Pdots, reaching a maximum especially at the 48th hour, indicating that it is the most effective in passing the blood-brain barrier. This result suggests that P4 may have properties that allow higher transport across the barrier, which may be advantageous for applications requiring medium to high permeability. P6 has the lowest permeability, which may be useful for applications requiring limited or minimum transport across the barrier.

4.2. Oral Candidiasis Sensor Applications

Point-of-care (POC) sensors for oral candidiasis provide rapid and non-invasive diagnosis. Electrochemical or optical biosensors are typically used to detect Candida biomarkers in saliva or oral swabs. These sensors are useful for early diagnosis, treatment monitoring, and clinical management, especially in immunocompromised patients.

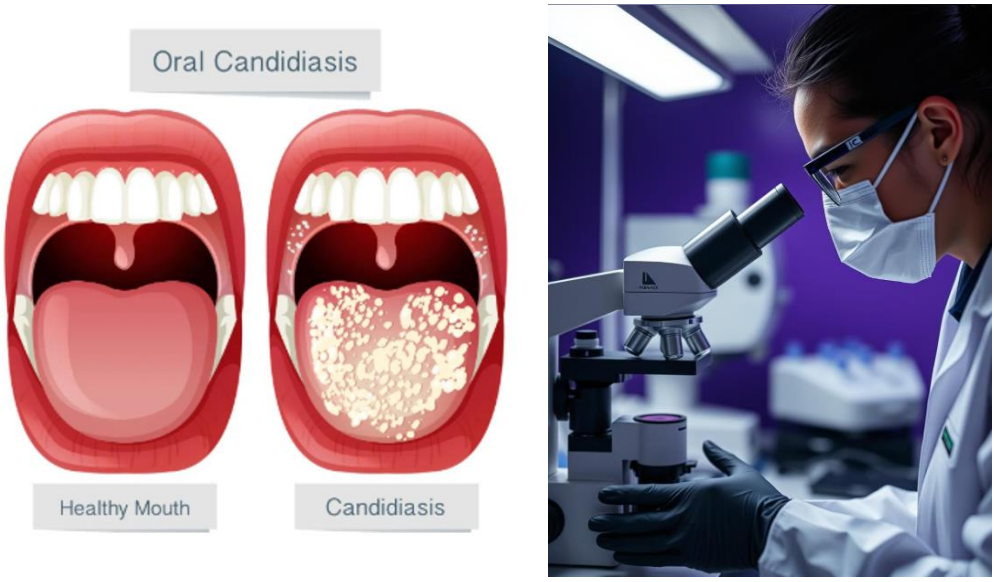

Figure 4.26. Illustration of Oral Candidiasis

Candida species, which cause oral candidiasis, are single-celled fungi, usually in the form of yeast. The chemical structure of their cell walls consists primarily of β-glucan, mannan, chitin, and proteins. The cell membrane is rich in sterols such as phospholipids and ergosterol. This structure allows the fungus to resist environmental stresses and is the target of antifungal treatments. Mannan and glucans in the cell wall play a significant role in interaction with the immune system.

Since the OH ends on the surface structure of Candida bacteria exhibit anionic charged properties, Phytic acid was preferred as the OH source and the reaction between the cationic polymer and Candida bacteria was simulated in this way.

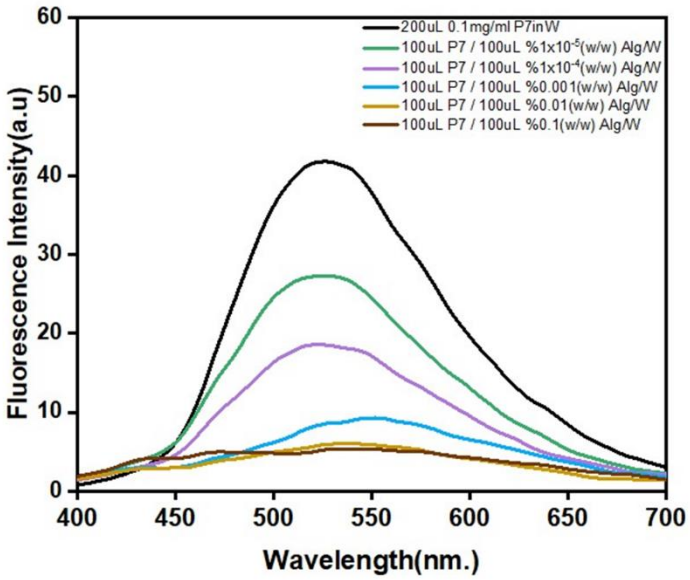

Figure 4.27. Fluorescence Intensity of Phytic Acid at different concentrations

In this study, where the BIOMACROS team volunteered, image processing and Absorbance-Fluorescence analyses of the samples were performed. After waking up in the morning, the subjects were allowed to only brush their teeth and drink water until they came to the laboratory. They were asked to swish the liquid in the test kits in their mouths for 10 seconds and put it in a test tube.

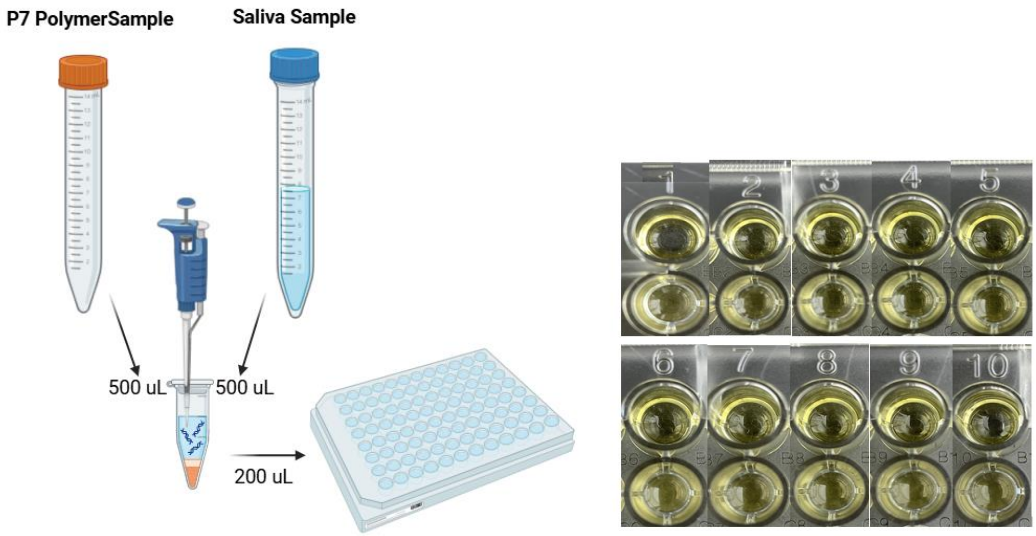

Figure 4.28. Sample Preparation Illustration of Oral Candidiasis Test Kit

Subject samples and polymer reference solution were observed under UV lamp. The emittance differences between the samples show how much candida bacteria the subjects' mouths have by providing FL turn off feature.

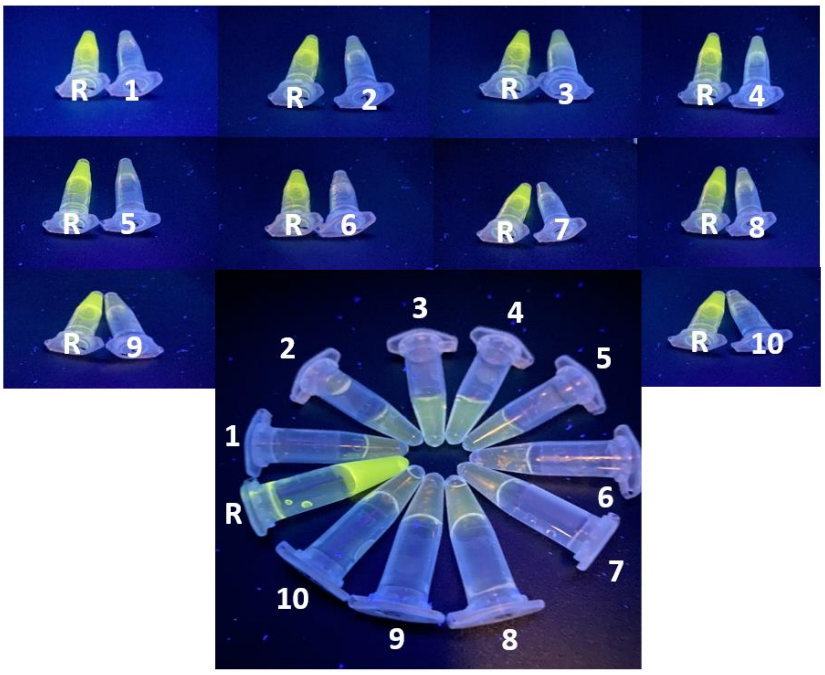

Figure 4.29. Fluorescence intensity observations of subjects with test kits.

After the observational color analysis was completed, it was photographed to verify this analysis with color codes. The photographed samples were analyzed with RGB color picker, and the codes were shared in a table.

Table 4.1. RGB color codes Blank + Saliva + Mannan M. samples

SAMPLE NAME:	RED/GREEN/BLUE (1)	RED/GREEN/BLUE (2)	RED/GREEN/BLUE (3)
Reference Polymer	192, 233, 85	179, 226, 82	192, 239, 102
Subject 1	129, 158, 200	136, 154, 207	129, 159, 197
Subject 2	105, 141, 168	112, 140, 185	98, 130, 173
Subject 3	120, 161, 148	123, 161, 175	120, 155, 149
Subject 4	133, 176, 174	129, 173, 171	130, 168, 174

Subject 5	118, 145, 167	114, 143, 179	109, 143, 172
Subject 6	141, 149, 205	106, 127, 183	92, 113, 161
Subject 7	126, 160, 184	131, 151, 203	89, 121, 171
Subject 8	159, 192, 192	154, 173, 183	133, 159, 168
Subject 9	119, 141, 165	121, 147, 165	185, 193, 201
Subject 10	149, 171, 194	136, 161, 158	144, 171, 167

The RGB color codes of the photographed reference and samples were accepted as RGB regions in the 3D plane and a distribution graph was created. The samples taken from the subjects and the locations of the reference polymer solution were examined. It examined whether there was a relationship between the RGB distributions of the samples and the amount of Candida bacteria.

The examinations showed that the distance to the reference polymer RGB code could be directly proportional to the amount of Candidiasis bacteria. Subjects 1, 2 and 5 have the farthest RGB values from the reference point and the lowest FL intensity values. On the other hand, subjects 3 and 4 have the closest positions to the reference RGB point in this plane and the highest FL intensity was observed in these two subjects.

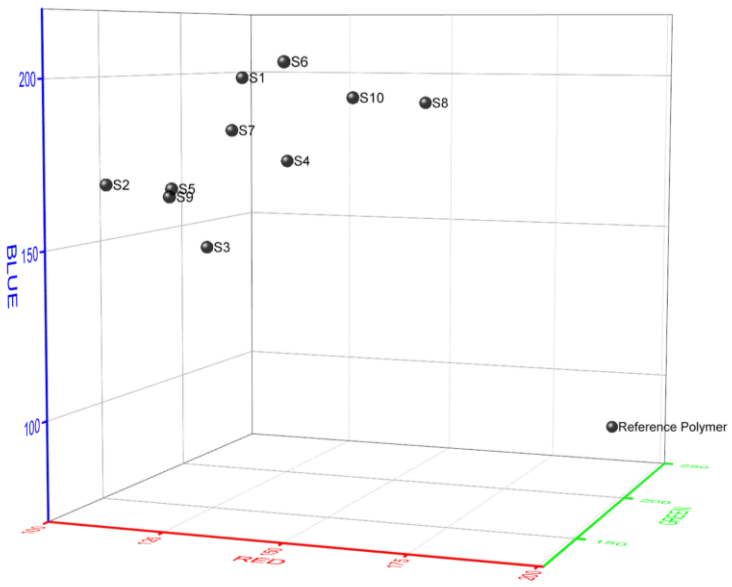

Figure 4.30. Display of the distribution graph of RGB color codes of photographed references and samples on a 3D plane.

The absorbance and fluorescence measurements of the polymer solution were made and recorded as a reference for each sample.

After taking the blank measurement with the polymer solution (100uL), the saliva samples were added to the polymer solutions (50uL) in order and absorbance and fluorescence measurements were taken again: For the evaluation of this result as positive or negative, the positive sample taken from the Candida albicans culture medium was added in the next step and the correlation was established with the magnitude of the difference.

Finally, a solution that will reduce the FL density, which we call Mannan Mimics (50uL), was added to the polymer + saliva sample. In this experiment, the effects of the saliva sample taken from the subjects on the FL density were examined.

Subject 1 is female, 24 years old. She is a smoker. She gave a sample in the morning without having breakfast and just brushing her teeth. In the measurement taken from the polymer solution, the absorbance density without sample was 0.21 a.u, while an increase in absorbance was observed up to 0.25 a.u with the additions made. However, the FL density was measured as 44 a.u, and with the addition of saliva sample it decreased to 17 a.u, and then to 13 a.u with the addition of 50 uL of Mannan mimic solution. In this case, the difference between the red curve and the green curve being less than 5 a.u raises the suspicion of candida colonization (oral candidiasis) in subject 1.

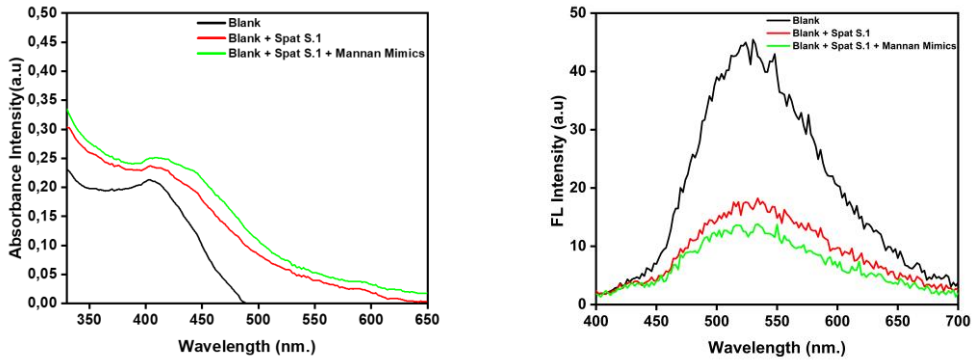

Figure 4.31. Absorbance and Fluorescence spectrums of the Sample 1, Black color refers Blank, Red color refers Blank + Saliva sample, Green color refers Blank + Saliva sample + Mannan Mimics

Subject 2 is female, 24 years old. She is a smoker. She gave a sample in the morning without having breakfast and just brushing her teeth. In the measurement taken from the polymer solution, the absorbance density without sample (blank) was 0.26 a.u, but no change in absorbance was observed with the additions. However, the FL density was measured as 42 a.u. With the addition of the FL saliva sample, it first decreased to 17 a.u and then to 13 a.u after the addition of Mannan mimic solution (50uL). In this case, it was understood that the difference between the red curve and the green curve was less than 5 a.u, which also raises the suspicion of candida colonization in sample 2.

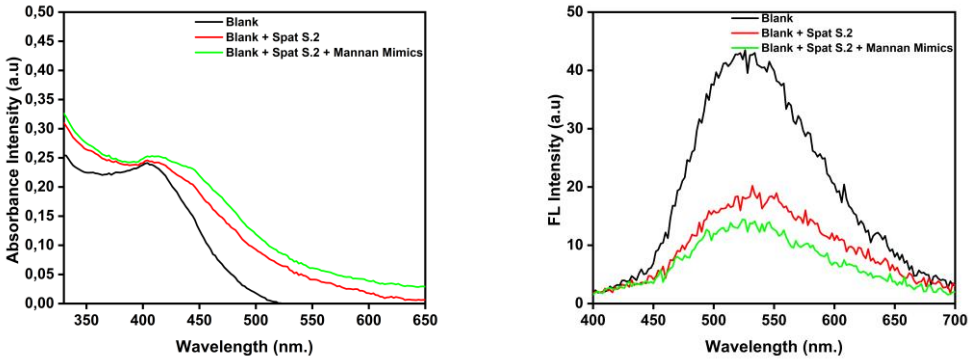

Figure 4.32. Absorbance and Fluorescence spectrums of the Sample 2, Black color refers Blank, Red color refers Blank + Saliva sample, Green color refers Blank + Saliva sample + Mannan Mimics

Subject 3 is a female, 24 years old. She does not smoke. She gave a sample without having breakfast and only brushing her teeth. The maximum FL value decreased from approximately 44a.u to 31a.u. It was observed that she had a higher FL value compared to the other subjects. It can be said that the reason for this is that the amount of oral candidiasis is less than the other samples.

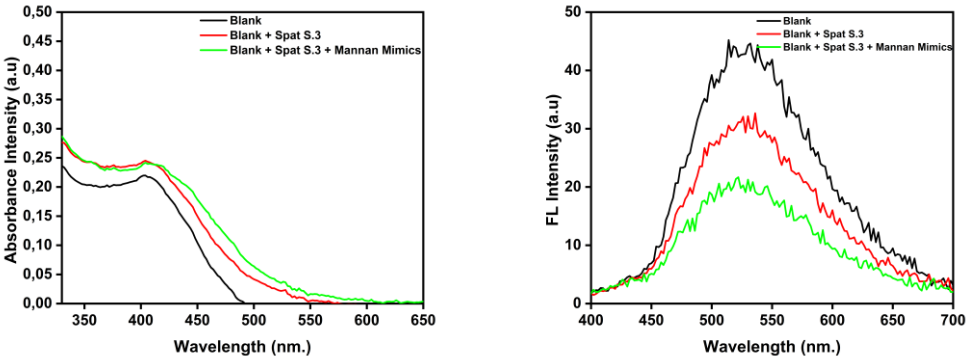

Figure 4.33. Absorbance and Fluorescence spectrums of the Sample 3, Black color refers Blank, Red color refers Blank + Saliva sample, Green color refers Blank + Saliva sample + Mannan Mimics

Subject 4 is a 27-year-old female nonsmoker. She provided a sample after brushing her teeth but without breakfast. Her maximum FL decreased from approximately 44 a.u to. 31 a.u. She was noted to exhibit a higher FL value compared to the other subjects. This is attributable to the lower presence of oral candidiasis in her sample compared to the others.

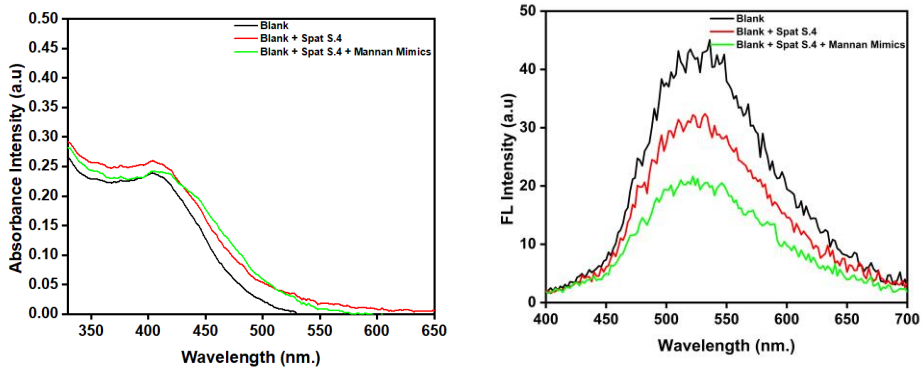

Figure 4.34. Absorbance and Fluorescence spectrums of the Sample 4, Black color refers Blank, Red color refers Blank + Saliva sample, Green color refers Blank + Saliva sample + Mannan Mimics

Subject 5 is a 29-year-old female and a smoker. She provided a sample in the morning after brushing her teeth but without having breakfast. Examination of the FL values reveals a high concentration of Candida bacteria in the sample. The maximum FL

value decreased from 45 a.u. to 18 a.u. following the sample addition. This FL decrease proves this.

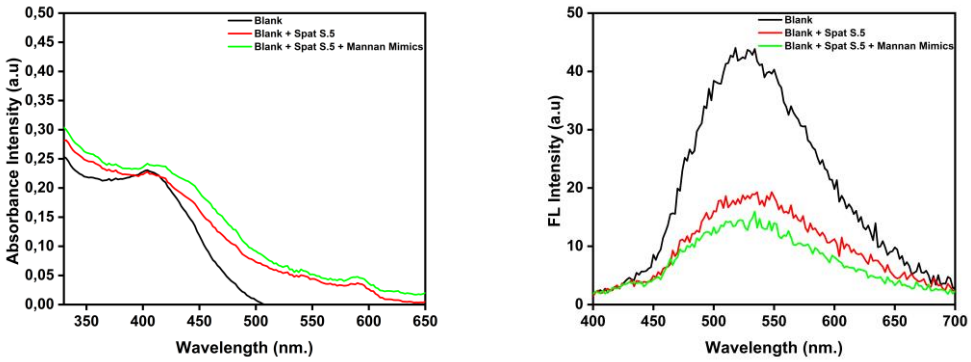

Figure 4.35. Absorbance and Fluorescence spectrums of the Sample 5, Black color refers Blank, Red color refers Blank + Saliva sample, Green color refers Blank + Saliva sample + Mannan Mimics

Subject 6 is a 27-year-old female who does not smoke. She provided a sample after brushing her teeth but prior to consuming breakfast. In contrast to other subjects, the absorbance analyzes revealed significantly higher intensities. The maximum FL value decreased from approximately 45 a.u. to 25 a.u., and the FL intensity was determined to be within average ranges.

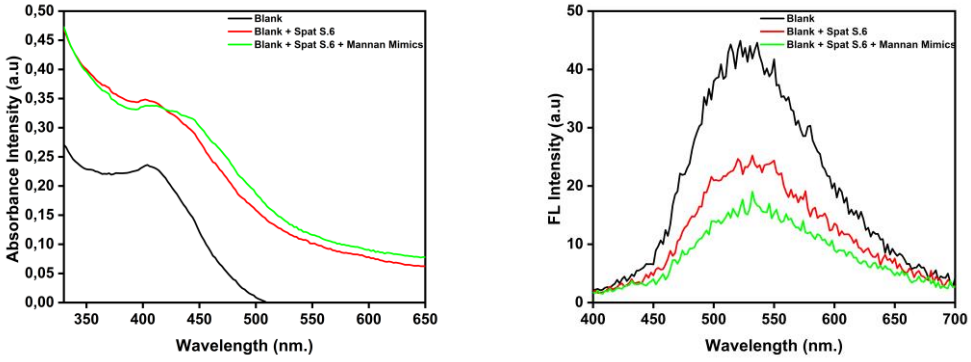

Figure 4.36. Absorbance and Fluorescence spectrums of the Sample 6, Black color refers Blank, Red color refers Blank + Saliva sample, Green color refers Blank + Saliva sample + Mannan Mimics

Subject 7 is a 24-year-old female smoker. She provided a sample after brushing her teeth but without breakfast. Her maximum FL decreased from approximately 44 a.u to. 22 a.u. It can be said that the reason for this is the high amount of oral candidiasis.

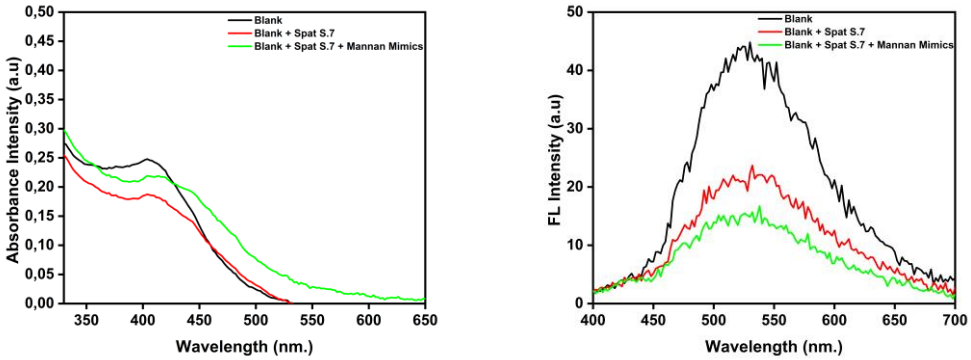

Figure 4.37. Absorbance and Fluorescence spectrums of the Sample 7, Black color refers Blank, Red color refers Blank + Saliva sample, Green color refers Blank + Saliva sample + Mannan Mimics

Subject 8 is a 30-year-old male non-smoker (for several years). He provided a sample after brushing his teeth but without breakfast. The maximum FL value decreased from approximately 45 a.u. to 28 a.u., and the FL intensity was determined to be within average ranges.

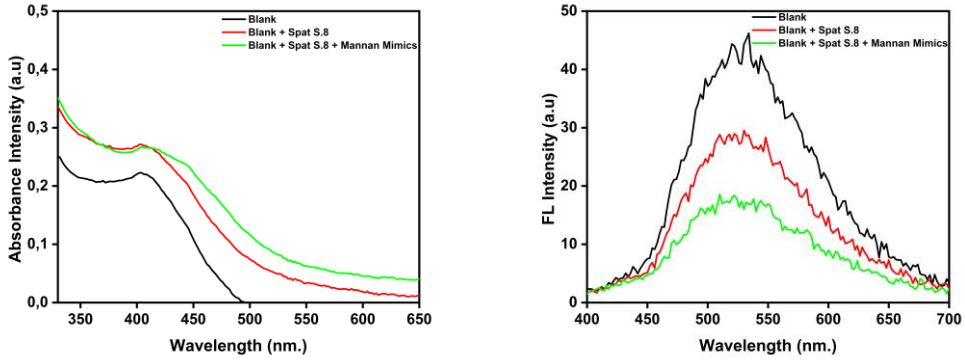

Figure 4.38. Absorbance and Fluorescence spectrums of the Sample 8, Black color refers Blank, Red color refers Blank + Saliva sample, Green color refers Blank + Saliva sample + Mannan Mimics

Subject 9 is a 27-year-old male non-smoker. He provided a sample after brushing his teeth but without breakfast. The maximum FL value decreased from approximately 45 a.u. to 25 a.u., and the FL intensity was determined to be within average ranges.

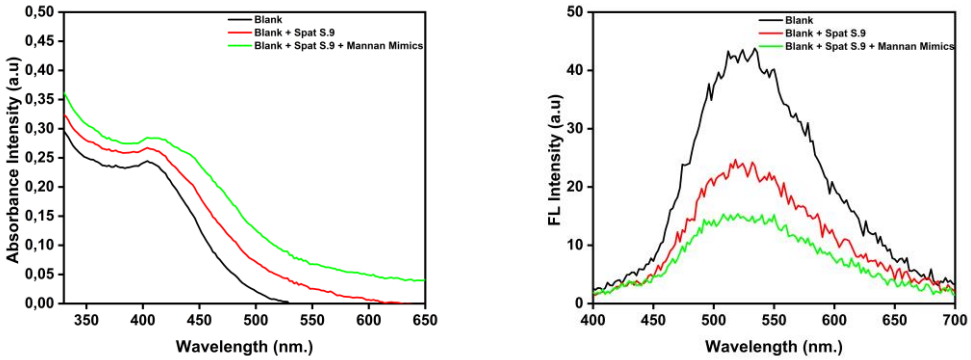

Figure 4.39. Absorbance and Fluorescence spectrums of the Sample 9, Black color refers Blank, Red color refers Blank + Saliva sample, Green color refers Blank + Saliva sample + Mannan Mimics

Subject 10 is a 24-year-old female and a smoker. She provided a sample in the morning after brushing her teeth but without having breakfast. Examination of the FL values reveals a high concentration of Candida bacteria in the sample. The maximum FL value decreased from 45 a.u. to 24 a.u. following the sample addition. This FL decrease proves this. The FL intensity was determined to be within the average ranges.

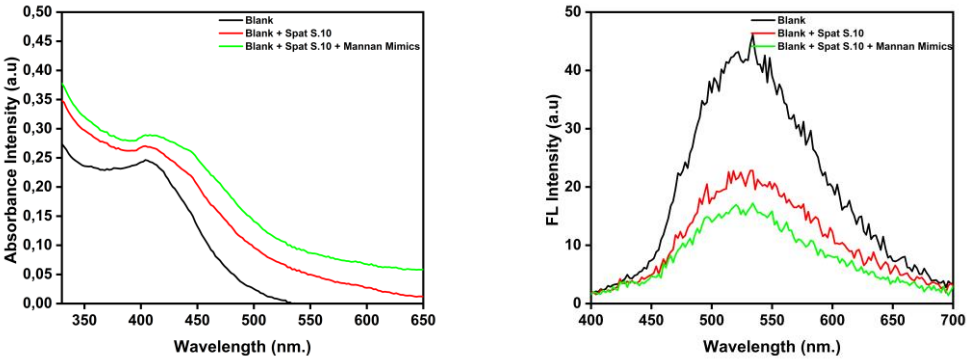

Figure 4.40. Absorbance and Fluorescence spectrums of the Sample 10, Black color refers Blank, Red color refers Blank + Saliva sample, Green color refers Blank + Saliva sample + Mannan Mimics

In the bar graph, the changes in the FL values of the samples taken from the subjects are shared. Blue columns show the polymer blank measurement values, orange columns show the Blank + Saliva FL values, and gray columns show the FL values after mannan mimics were added to the medium. The maximum values in each graph were taken as reference when creating this graph. In this graph, the FL intensity behaviors of Blank, Blank + Saliva and Blank + Saliva + Mannan M. samples of all subjects are shown in order.

In two samples (2 and 5), FL intensity below 20 a.u was observed with saliva addition. In other samples, FL intensity above 20 a.u was observed with saliva addition.

It was understood that the samples where the difference between the positive control (gray bar) and the orange bar (saliva sample) is equal to or less than 5 a.u carry the risk of Candida colonization. Conversely, in cases where the difference is equal to or greater than 10 a.u, it can be evaluated that there is no risk of Candida colonization.

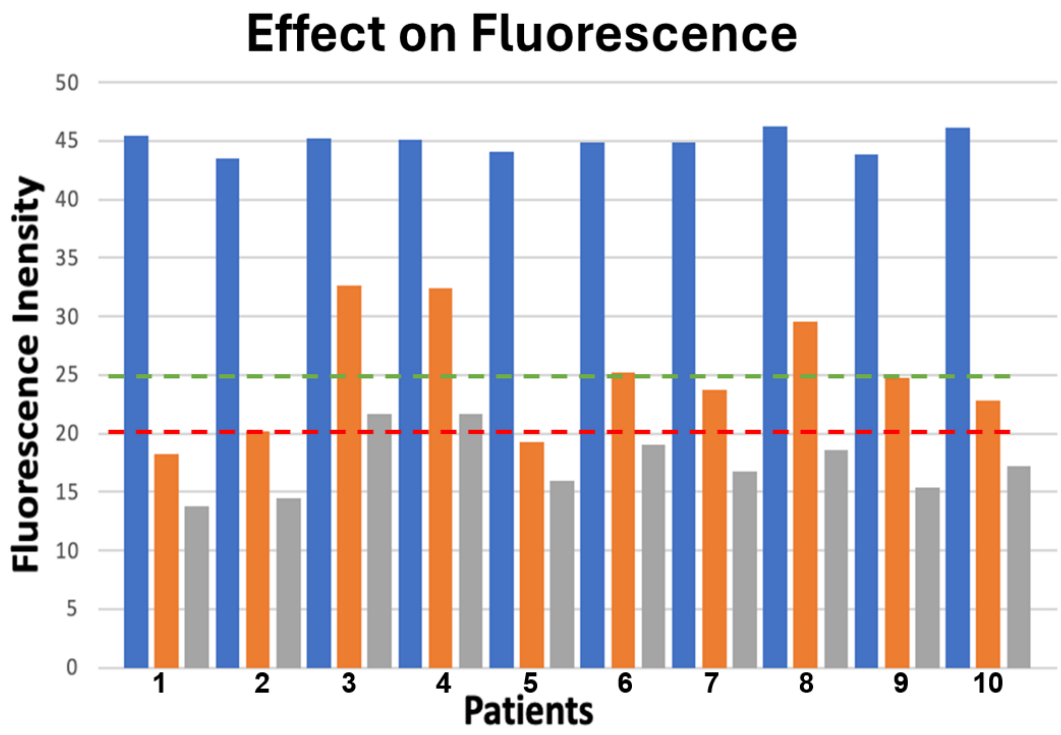

Figure 4.41. Bar graph Fluorescence intensity observations of subjects with test kits

Point-of-care (POC) tests provide a fast, practical, and effective solution for detecting oral candidiasis, delivering results within minutes to enable rapid diagnosis and treatment. Their ability to be used directly at the patient's location eliminates the need for laboratory facilities, saving both time and resources. With simple and non-invasive procedures, these tests enhance patient comfort while offering ease of use for healthcare providers. Early diagnosis and treatment are particularly critical for immunocompromised individuals, as they help prevent complications. Furthermore, the portable design of POC tests makes them suitable for use in low-resource settings and allows for treatment monitoring, improving overall disease management. In our research, we focused on developing a POC test by leveraging the fluorescence properties of cationic polythiophenes as sensors. Studies have demonstrated the potential of these test kits for effectively detecting oral candidiasis.

CHAPTER 5

CONCLUSION

In this thesis, the synthesis and characterization of cationic and non-ionic monomers and their precursors were performed and confirmed using NMR, Mass Spectroscopy, Absorbance Spectroscopy, and Fluorescence Spectroscopy. Homopolymers and copolymers, synthesized via the oxidative polymerization method using different ratios of M1 and M2 monomers, were characterized through NMR, Mass Spectroscopy, Raman Spectroscopy, Dynamic Light Scattering, Zeta Potential Charge Analysis, and Quantum Yield Analysis.

Research has focused on investigating strategies to enhance the permeability of nanomaterials across the blood-brain barrier for biomedical applications, utilizing nanophase separation to optimize Pdot structures. Additionally, studies were conducted on their ability to pass through the Blood-Brain Barrier in Pdot form (5-30 nm). P4 polymer has better performance compared to other polymers.

The studies on Candida detection focused on the use of cationic polymers as optical probes for identifying Candida species, particularly in oral environments. These materials demonstrated enhanced fluorescence and high specificity for binding to Candida cells by optimizing their structural and optical properties. Various spectroscopic techniques were employed to assess their interactions with Candida, highlighting the sensitivity and selectivity of the cationic polymers. These findings suggest that cationic polymers could serve as effective noninvasive diagnostic tools for the early detection of Oral Candida, offering a promising approach for improved clinical management.

This thesis primarily focuses on the characterization of cationic, non-ionic polymers and polymer dots (Pdots) to enhance their optical and structural properties using spectroscopic and scattering techniques, with applications in detecting Oral Candidiasis and crossing the Blood-Brain Barrier (BBB).

REFERENCES

Al-Azzawi, Ahmed G. S., Shujahadeen B. Aziz, Elham M. A. Dannoun, Ahmed Iraqi, Muaffaq M. Nofal, Ary R. Murad, and Ahang M. Hussein. 2022. "A Mini Review on the Development of Conjugated Polymers: Steps towards the Commercialization of Organic Solar Cells." *Polymers* 15 (1): 164. https://doi.org/10.3390/polym15010164.

Anni, Marco. 2023. "Investigation of the Origin of High Photoluminescence Quantum Yield in Thienyl-S,S-Dioxide AIEgens Oligomers by Temperature Dependent Optical Spectroscopy." *Molecules* 28 (13): 5161. https://doi.org/10.3390/molecules28135161.

Arslan-Yildiz, Ahu, Rami El Assal, Pu Chen, Sinan Guven, Fatih Inci, and Utkan Demirci. 2016. "Towards Artificial Tissue Models: Past, Present, and Future of 3D Bioprinting." *Biofabrication* 8 (1): 014103. https://doi.org/10.1088/1758-5090/8/1/014103.

Bautista, Michael V., Anthony J. Varni, Josué Ayuso-Carrillo, Matthew C. Carson, and Kevin J. T. Noonan. 2021. "Pairing Suzuki–Miyaura Cross-Coupling and Catalyst Transfer Polymerization." *Polymer Chemistry* 12 (10): 1404–14. https://doi.org/10.1039/D0PY01507E.

Braeken, Yasmine, Srujan Cheruku, Anitha Ethirajan, and Wouter Maes. 2017. "Conjugated Polymer Nanoparticles for Bioimaging." *Materials* 10 (12): 1420. https://doi.org/10.3390/ma10121420.

Brambilla, Luigi, Matteo Tommasini, Ioan Botiz, Khosrow Rahimi, John O. Agumba, Natalie Stingelin, and Giuseppe Zerbi. 2014. "Regio-Regular Oligo and Poly(3-Hexyl Thiophene): Precise Structural Markers from the Vibrational Spectra of Oligomer Single Crystals." *Macromolecules* 47 (19): 6730–39. https://doi.org/10.1021/ma501614c.

Coropceanu, Veaceslav, Jérôme Cornil, Demetrio A. da Silva Filho, Yoann Olivier, Robert Silbey, and Jean-Luc Brédas. 2007. "Charge Transport in Organic Semiconductors." *Chemical Reviews* 107 (4): 926–52. https://doi.org/10.1021/cr050140x.

Englert, Christoph, Anne-Kristin Trützschler, Martin Raasch, Tanja Bus, Philipp Borchers, Alexander S. Mosig, Anja Traeger, and Ulrich S. Schubert. 2016. "Crossing the Blood-Brain Barrier: Glutathione-Conjugated Poly(Ethylene Imine) for Gene Delivery." *Journal of Controlled Release* 241 (November):1–14. https://doi.org/10.1016/j.jconrel.2016.08.039.

Feng, Liheng, Chunlei Zhu, Huanxiang Yuan, Libing Liu, Fengting Lv, and Shu Wang. 2013. "Conjugated Polymer Nanoparticles: Preparation, Properties, Functionalization and Biological Applications." *Chemical Society Reviews* 42 (16): 6620. https://doi.org/10.1039/c3cs60036j.

Hebert, David D., Michael A. Naley, Carter C. Cunningham, David J. Sharp, Emma E. Murphy, Venus Stanton, and Jennifer A. Irvin. 2021. "Enabling Conducting Polymer Applications: Methods for Achieving High Molecular Weight in Chemical Oxidative Polymerization in Alkyl- and Ether-Substituted Thiophenes." *Materials* 14 (20): 6146. https://doi.org/10.3390/ma14206146.

Hernandez, V., F. J. Ramirez, T. F. Otero, and J. T. Lopez Navarrete. 1994. "An Interpretation of the Vibrational Spectra of Insulating and Electrically Conducting Poly(3-Methylthiophene) Aided by a Theoretical Dynamical Model." *The Journal of Chemical Physics* 100 (1): 114–29. https://doi.org/10.1063/1.466982.

Heydari Gharahcheshmeh, Meysam, and Karen K. Gleason. 2022. "Recent Progress in Conjugated Conducting and Semiconducting Polymers for Energy Devices." *Energies* 15 (10): 3661. https://doi.org/10.3390/en15103661.

Higgins, Stuart G., Alessandra Lo Fiego, Ijeoma Patrick, Adam Creamer, and Molly M. Stevens. 2020. "Organic Bioelectronics: Using Highly Conjugated Polymers to Interface with Biomolecules, Cells, and Tissues in the Human Body." *Advanced Materials Technologies* 5 (11). https://doi.org/10.1002/admt.202000384.

Inal, Sahika, Jonathan Rivnay, Andreea-Otilia Suiu, George G. Malliaras, and Iain McCulloch. 2018. "Conjugated Polymers in Bioelectronics." *Accounts of Chemical Research* 51 (6): 1368–76. https://doi.org/10.1021/acs.accounts.7b00624.

İncel, Anıl, Osman Akın, Ali Çağır, Ümit Hakan Yıldız, and Mustafa M. Demir. 2017. "Smart Phone Assisted Detection and Quantification of Cyanide in Drinking Water by Paper Based Sensing Platform." *Sensors and Actuators B: Chemical* 252 (November):886–93. https://doi.org/10.1016/j.snb.2017.05.185.

Karabacak, Soner, Başak Çoban, Ahu Arslan Yıldız, and Ümit Hakan Yıldız. 2024. "Near-Infrared Emissive Super Penetrating Conjugated Polymer Dots for Intratumoral Imaging in 3D Tumor Spheroid Models." *Advanced Science*, July. https://doi.org/10.1002/advs.202403398.

Knop, Katrin, Richard Hoogenboom, Dagmar Fischer, and Ulrich S. Schubert. 2010. "Poly(Ethylene Glycol) in Drug Delivery: Pros and Cons as Well as Potential Alternatives." *Angewandte Chemie International Edition* 49 (36): 6288–6308. https://doi.org/10.1002/anie.200902672.

Köksal, Büşra, Rümeysa Bilginer Kartal, Ufuk Saim Günay, Hakan Durmaz, Ahu Arslan Yildiz, and Ümit Hakan Yildiz. 2024. "Fabrication of Gelatin-Polyester Based Biocomposite Scaffold via One-Step Functionalization of Melt Electrowritten Polymer Blends in Aqueous Phase." *International Journal of Biological Macromolecules* 265 (April):130938. https://doi.org/10.1016/j.ijbiomac.2024.130938.

Lakowicz, Joseph R., ed. 2006. *Principles of Fluorescence Spectroscopy*. Boston, MA: Springer US. https://doi.org/10.1007/978-0-387-46312-4.

Lee, Moo Yeol, Hae Rang Lee, Cheol Hee Park, Seul Gi Han, and Joon Hak Oh. 2018. "Organic Transistor-Based Chemical Sensors for Wearable Bioelectronics." *Accounts of Chemical Research* 51 (11): 2829–38. https://doi.org/10.1021/acs.accounts.8b00465.

Lee, Pei-Wei, Marissa Totten, Liben Chen, Fan-En Chen, Alexander Y. Trick, Kushagra Shah, Hoan Thanh Ngo, et al. 2022. "A Portable Droplet Magnetofluidic Device for Point-of-Care Detection of Multidrug-Resistant Candida Auris." *Frontiers in Bioengineering and Biotechnology* 10 (March). https://doi.org/10.3389/fbioe.2022.826694.

Li, Shanghao, Zhili Peng, Julia Dallman, James Baker, Abdelhameed M. Othman, Patrica L. Blackwelder, and Roger M. Leblanc. 2016. “Crossing the Blood–Brain–Barrier with Transferrin Conjugated Carbon Dots: A Zebrafish Model Study.” *Colloids and Surfaces B: Biointerfaces* 145 (September):251–56. https://doi.org/10.1016/j.colsurfb.2016.05.007.

Lim, Shi Ying, Wei Shen, and Zhiqiang Gao. 2015. “Carbon Quantum Dots and Their Applications.” *Chemical Society Reviews* 44 (1): 362–81. https://doi.org/10.1039/C4CS00269E.

Liu, Feng, Yaohong Zhang, Chao Ding, Syuusuke Kobayashi, Takuya Izuishi, Naoki Nakazawa, Taro Toyoda, et al. 2017. “Highly Luminescent Phase-Stable $CsPbI_3$ Perovskite Quantum Dots Achieving Near 100% Absolute Photoluminescence Quantum Yield.” *ACS Nano* 11 (10): 10373–83. https://doi.org/10.1021/acsnano.7b05442.

Liu, Yang, Junjun Liu, Jiayi Zhang, Xiucun Li, Fangsiyu Lin, Nan Zhou, Bai Yang, and Laijin Lu. 2018. “Noninvasive Brain Tumor Imaging Using Red Emissive Carbonized Polymer Dots across the Blood–Brain Barrier.” *ACS Omega* 3 (7): 7888–96. https://doi.org/10.1021/acsomega.8b01169.

Lopez Navarrete, J. T., and G. Zerbi. 1991. “Lattice Dynamics and Vibrational Spectra of Polythiophene. I. Oligomers and Polymer.” *The Journal of Chemical Physics* 94 (2): 957–64. https://doi.org/10.1063/1.459986.

Lu, Huizhi, Xunlai Li, and Qingquan Lei. 2021. “Conjugated Conductive Polymer Materials and Its Applications: A Mini-Review.” *Frontiers in Chemistry* 9 (September). https://doi.org/10.3389/fchem.2021.732132.

Özenler, Sezer, Muge Yucel, Özge Tüncel, Hakan Kaya, Serdar Özçelik, and Umit Hakan Yildiz. 2019a. “Single Chain Cationic Polymer Dot as a Fluorescent Probe for Cell Imaging and Selective Determination of Hepatocellular Carcinoma Cells.” *Analytical Chemistry* 91 (16): 10357–60. https://doi.org/10.1021/acs.analchem.9b02300.

Pankow, Robert M., and Barry C. Thompson. 2020. “The Development of Conjugated Polymers as the Cornerstone of Organic Electronics.” *Polymer* 207 (October):122874. https://doi.org/10.1016/j.polymer.2020.122874.

Perepichka, I. F., D. F. Perepichka, H. Meng, and F. Wudl. 2005. “Light-Emitting Polythiophenes.” *Advanced Materials* 17 (19): 2281–2305. https://doi.org/10.1002/adma.200500461.

Pitsalidis, Charalampos, Anna-Maria Pappa, Alexander J. Boys, Ying Fu, Chrysanthi-Maria Moysidou, Douglas van Niekerk, Janire Saez, Achilleas Savva, Donata Iandolo, and Róisín M. Owens. 2022. “Organic Bioelectronics for *In Vitro* Systems.” *Chemical Reviews* 122 (4): 4700–4790. https://doi.org/10.1021/acs.chemrev.1c00539.

Safavieh, Mohammadali, Chad Coarsey, Nwadiuto Esiobu, Adnan Memic, Jatin Mahesh Vyas, Hadi Shafiee, and Waseem Asghar. 2017. “Advances in *Candida* Detection Platforms for Clinical and Point-of-Care Applications.” *Critical Reviews in Biotechnology* 37 (4): 441–58. https://doi.org/10.3109/07388551.2016.1167667.

Sayar, Melike, Erman Karakuş, Tuğrul Güner, Busra Yildiz, Umit Hakan Yildiz, and Mustafa Emrullahoğlu. 2018. “A BODIPY-Based Fluorescent Probe to Visually Detect Phosgene: Toward the Development of a Handheld Phosgene Detector.” *Chemistry – A European Journal* 24 (13): 3136–40. https://doi.org/10.1002/chem.201705613.

Sim, Tao Ming, Dinesh Tarini, S. Thameem Dheen, Boon Huat Bay, and Dinesh Kumar Srinivasan. 2020. “Nanoparticle-Based Technology Approaches to the Management of Neurological Disorders.” *International Journal of Molecular Sciences* 21 (17): 6070. https://doi.org/10.3390/ijms21176070.

Sirringhaus, Henning. 2014. “25th Anniversary Article: Organic Field-Effect Transistors: The Path Beyond Amorphous Silicon.” *Advanced Materials* 26 (9): 1319–35. https://doi.org/10.1002/adma.201304346.

Syedmoradi, Leila, Maryam Daneshpour, Mehrdad Alvandipour, Frank A. Gomez, Hassan Hajghassem, and Kobra Omidfar. 2017. “Point of Care Testing: The Impact

of Nanotechnology.” *Biosensors and Bioelectronics* 87 (January):373–87. https://doi.org/10.1016/j.bios.2016.08.084.

Tokel, Onur, Umit Hakan Yildiz, Fatih Inci, Naside Gozde Durmus, Okan Oner Ekiz, Burak Turker, Can Cetin, et al. 2015. “Portable Microfluidic Integrated Plasmonic Platform for Pathogen Detection.” *Scientific Reports* 5 (1): 9152. https://doi.org/10.1038/srep09152.

Torres, B. B. M., and D. T. Balogh. 2012. “Regioregular Improvement on the Oxidative Polymerization of Poly-3-octylthiophenes by Slow Addition of Oxidant at Low Temperature.” *Journal of Applied Polymer Science* 124 (4): 3222–28. https://doi.org/10.1002/app.35441.

Tu, Meng-Che, Hari Krishna Svm, Alahakoon Thilini, Lim Tse Loong Wallace, Shabbir Moochhala, Umit Hakan Yildiz, Al. Palaniappan, and Bo Liedberg. 2017. “Tuning Pendant Groups of Polythiophene on Carbon Nanotubes for Vapour Classification.” *Sensors and Actuators B: Chemical* 247 (August):916–22. https://doi.org/10.1016/j.snb.2017.03.095.

Xu, Man, Chuanxin Wei, Yunlong Zhang, Jiefeng Chen, Hao Li, Jingrui Zhang, Lili Sun, et al. 2024. “Coplanar Conformational Structure of Π-Conjugated Polymers for Optoelectronic Applications.” *Advanced Materials* 36 (1). https://doi.org/10.1002/adma.202301671.

Yadav, Pravesh Kumar, Sunil Kumar, and Pralay Maiti. 2022. “Conjugated Polymers for Solar Cell Applications.” In *Conjugated Polymers for Next-Generation Applications*, 367–401. Elsevier. https://doi.org/10.1016/B978-0-12-824094-6.00004-2.

Yildiz, Umit Hakan, Palaniappan Alagappan, and Bo Liedberg. 2013a. “Naked Eye Detection of Lung Cancer Associated MiRNA by Paper Based Biosensing Platform.” *Analytical Chemistry* 85 (2): 820–24. https://doi.org/10.1021/ac3034008.

Yildiz, Umit Hakan, Elif Sahin, Idris M. Akhmedov, Cihangir Tanyeli, and Levent Toppare. 2006. “A New Soluble Conducting Polymer and Its Electrochromic

Devices." *Journal of Polymer Science Part A: Polymer Chemistry* 44 (7): 2215–25. https://doi.org/10.1002/pola.21337.

Yu, Jiangbo, Yu Rong, Chun-Ting Kuo, Xing-Hua Zhou, and Daniel T. Chiu. 2017. "Recent Advances in the Development of Highly Luminescent Semiconducting Polymer Dots and Nanoparticles for Biological Imaging and Medicine." *Analytical Chemistry* 89 (1): 42–56. https://doi.org/10.1021/acs.analchem.6b04672.

Yuan, Ye, Weiying Hou, Weiping Qin, and Changfeng Wu. 2021. "Recent Advances in Semiconducting Polymer Dots as Optical Probes for Biosensing." *Biomaterials Science* 9 (2): 328–46. https://doi.org/10.1039/D0BM01038C.

Yucel, Muge, Altug Koc, Ayfer Ulgenalp, Gun Deniz Akkoc, Metin Ceyhan, and Umit Hakan Yildiz. 2021. "PCR-Free Methodology for Detection of Single-Nucleotide Polymorphism with a Cationic Polythiophene Reporter." *ACS Sensors* 6 (3): 950–57. https://doi.org/10.1021/acssensors.0c02130.

Yucel, Muge, Rabia Onbas, Ahu Arslan Yildiz, and Umit Hakan Yildiz. 2024. "The Soft Nanodots as Fluorescent Probes for Cell Imaging: Analysis of Cell and Spheroid Penetration Behavior of Single Chain Polymer Dots." *Macromolecular Bioscience* 24 (4). https://doi.org/10.1002/mabi.202300402.

Zaumseil, Jana, and Henning Sirringhaus. 2007. "Electron and Ambipolar Transport in Organic Field-Effect Transistors." *Chemical Reviews* 107 (4): 1296–1323. https://doi.org/10.1021/cr0501543.

Zhang, Ze, Chenhao Yu, Yuyang Wu, Zhe Wang, Haotian Xu, Yining Yan, Zhixin Zhan, and Shengyan Yin. 2024. "Semiconducting Polymer Dots for Multifunctional Integrated Nanomedicine Carriers." *Materials Today Bio* 26 (June):101028. https://doi.org/10.1016/j.mtbio.2024.101028.